8-1999

Evaluation of Raman Spectroscopy and Ruby Piezospectroscopy as Tools for Investigating the Corrosion of Metallic Alloys

Daniel P. Renusch
Western Michigan University

EVALUATION OF RAMAN SPECTROSCOPY AND RUBY PIEZOSPECTROSCOPY AS TOOLS FOR INVESTIGATING THE CORROSION OF METALLIC ALLOYS

by

Daniel P. Renusch

A Dissertation
Submitted to the
Faculty of The Graduate College
in partial fulfillment of the
requirements for the
Degree of Doctor of Philosophy
Department of Physics

Western Michigan University
Kalamazoo, Michigan
August 1999

EVALUATION OF RAMAN SPECTROSCOPY AND RUBY PIEZOSPECTROSCOPY AS TOOLS FOR INVESTIGATING THE CORROSION OF METALLIC ALLOYS

Daniel P. Renusch, Ph.D.

Western Michigan University, 1999

Stainless steel system components that operate in high temperature oxidizing environments obtain protection from corrosion by means of thermally grown chromia and alumina scales. Ongoing investigations of protective scales utilize a battery of experimental and theoretical techniques. A technique which has received little attention is Raman scattering. The reason for its limited use has been long data acquisition times required to obtain suitable spectra from thin surface oxides. Because advances in detection systems, namely the multichannel CCD (charge coupled devices), have recently provided dramatic improvement in the sensitivity of Raman scattering experiments, we decided to reevaluate the technique as a probe of oxide scale evolution.

During the Raman investigation it was observed that many of the scales that formed on aluminum containing alloys fluoresced when irradiated with the laser. The origin of some of the fluorescence was found to be due to the presence of ruby (α-Al_2O_3:Cr) in the scale. Because ruby fluorescence has a rich history in high pressure diamond anvil cell research, it seemed likely to provide scale stress information (i.e. ruby piezospectroscopy). Thus, our research objectives were adjusted to include the evaluation of ruby piezospectroscopy as a tool for the investigation of scale stress.

The multichannel CCD was found to provide short data acquisition times (500 sec.). Both the Raman and fluorescence techniques were found to be convenient

because they require little sample preparation and are non-destructive. A Raman "fingerprint" technique was found to be useful for identifying and tracking scale oxide phase behavior, during transient oxidation, steady-state oxidation, and breakaway corrosion. Raman spectroscopy and ruby piezospectroscopy have been used to provide insight into the reactive element effect. By using micro-fluorescence we have also provided insight into the thermal-mechanical behavior of scales near sample edges and of scales with convoluted (or wrinkled) interface morphologies.

INFORMATION TO USERS

This manuscript has been reproduced from the microfilm master. UMI films the text directly from the original or copy submitted. Thus, some thesis and dissertation copies are in typewriter face, while others may be from any type of computer printer.

The quality of this reproduction is dependent upon the quality of the copy submitted. Broken or indistinct print, colored or poor quality illustrations and photographs, print bleedthrough, substandard margins, and improper alignment can adversely affect reproduction.

In the unlikely event that the author did not send UMI a complete manuscript and there are missing pages, these will be noted. Also, if unauthorized copyright material had to be removed, a note will indicate the deletion.

Oversize materials (e.g., maps, drawings, charts) are reproduced by sectioning the original, beginning at the upper left-hand corner and continuing from left to right in equal sections with small overlaps. Each original is also photographed in one exposure and is included in reduced form at the back of the book.

Photographs included in the original manuscript have been reproduced xerographically in this copy. Higher quality 6" x 9" black and white photographic prints are available for any photographs or illustrations appearing in this copy for an additional charge. Contact UMI directly to order.

UMI®

Bell & Howell Information and Learning
300 North Zeeb Road, Ann Arbor, MI 48106-1346 USA
800-521-0600

ACKNOWLEDGMENTS

I wish to express my sincere gratitude to Dr. Marcos Grimsditch for suggesting the research problems reported in this thesis and his untiring support and guidance throughout their investigation. It is with great pleasure that I thank Dr. B.W. Veal for his inspiring discussions and enjoyable collaborations. I also wish to record my thanks to my corrosion co-investigators, I am both fortunate and grateful to be a member of the team. With gratitude I thank Professor Lisa Paulius of Western Michigan University for her help and guidance. With great pleasure, thanks to Dr. P. Y. Hou and Dr. R. M. Cannon of the Lawrence Berkeley Laboratory for their collaborations on the work present in Chapters IV and V. Special thanks to Dr. J. K. Wright and R. L. Williamson of the Idaho National Engineering and Environmental Laboratory for the finite element calculation presented in Chapter V. I wish to express my sincere gratitude to the U. S. Department of Energy, Basic Energy Sciences under contract W-31-109-ENG-38, for their financial support.

Daniel P. Renusch

TABLE OF CONTENTS

Table of Contents-Continucd

CHAPTERS

Table of Contents-Continued

LIST OF TABLES

LIST OF FIGURES

List of Figures-Continued

CHAPTER I

INTRODUCTION

General Aspects of Corrosion

The disastrous effects of corrosion are evident in our day to day lives. It attacks many of the personal possessions that we hold close to our hearts, such as our cars and our homes. Many people have had to live with auto-body rust prior to the vehicle being paid off. Homeowners have had to replace or repair hot water heaters and furnaces because of corrosion-related failures. The impact that corrosion has on the United States economy has been estimated to be between $30 billion and $300 billion per year [1,2]. Much of the impact is felt by industry in terms of: plant downtime, loss of product, loss of efficiency and contamination [1]. Corrosion-related failures have also caused damage to the environment. According to the United States Environmental Protection Agency (EPA), gasoline and petroleum leaking from underground storage tanks is the primary cause of ground water contamination [3,4]. As of 1998, EPA regulations require corrosion protection for all underground storage tanks.

For the purpose of this thesis we will use the usual definition of corrosion: "the destructive result of chemical reactions between a metal or metallic alloy and its environment" [5]. The corrosion of ceramics, polymers, and semiconductors are beyond the scope of this work. There are a broad range of environments that cause metallic corrosion, and there are a vast number of techniques for prevention. The most common forms of corrosion involve a liquid electrolyte, usually water. However with the advance of industry and technology, new, very harsh, corrosive environments are

attacking modern engineering alloys. An example is the environment found inside gas turbine engines.

The internal combustion engine was the first power source for the aircraft industry. It was used by the Wright Brother in 1909, for the first powered flight and is still used today. In 1937 the first successful gas turbine engine was constructed by Whittle [6]. Earlier attempts to produce gas turbines were unsuccessful because the materials available at the time did not have the capability of withstanding the high stress and temperatures that an efficient gas turbine engine depends upon. Due largely to alloy development, the first turbine aircraft engines were in service by the early 1950's [6].

The largest mechanical stress that modern turbine engines are subjected to is due to the high rotational speeds that some of the components experience (1000 to 30000 rpm's) [7]. The material also has to withstand these large mechanical stresses at elevated temperatures, as high as 1370°C [8]. At these elevated temperatures corrosion poses a serious problem. The high rotational speeds and strict engineering tolerances often make corrosion related failures catastrophic and consequently unacceptable. Therefore, corroded internal turbine engine components have to be replaced prior to failure, which in turn causes costly engine overhauls.

Our high-tech society has produced a large number of harsh environments that cause corrosion, the study of which has been a never-ending exercise. To name a few: furnaces, rocket engines, power plants, and petrochemical plants. As our technology grows we can expect that the number of man-made corrosive environments will increase, and the development of new corrosion-resistant materials will be necessary.

In this chapter we will address some of the complex issues of high temperature corrosion and corrosion protection. We will briefly describe some of the common techniques used for characterizing high temperature corrosion products. Lastly, we

will state our motivation for evaluating Raman spectroscopy and ruby piezospectroscopy as tools for the study of high temperature corrosion.

Corrosion and Corrosion Protection at High Temperatures

Most metals will spontaneously corrode in air. In spite of air being mostly nitrogen, the dominant chemical reaction is oxidation, which can be written as:

$$aM + 1/2\ bO_2 \rightarrow M_aO_b \qquad 1.1$$

This reaction may appear simple, but it does depend on a number of factors and in turn the reaction mechanisms can be complex [9]. At modestly elevated temperatures (e.g. ~300°C) the oxidation reaction can quickly (1 hr) produce visible corrosion products on elemental metals and some stainless steels. At high temperatures (e.g. T > 1000°C) oxidation can create significant amounts of corrosion products.

If the products of Eq. 1.1 are non-volatile, they have a tendency to adhere to the surface of the metal, and produce a thin surface film called a scale. The scale acts as a protective barrier between the metal and the surrounding air (or oxygen). When a compact scale covers the surface of a metal or alloy the reaction may proceed only through solid-state diffusion of reactants through the film [9]. Some desirable properties of a protective scale are therefore; slow growth, strong adhesion, and stability.

Although a thermally grown scale may seem to be a reasonably simple remedy to corrosion, its nature can be very complex. Scales are polycrystalline, can be composed of several different chemical and crystalline phases, are subject to thermally generated stresses, and can have complicated morphologies. This complexity makes the prediction of a scale's usefulness as a protective film near impossible. As a result,

most corrosion-resistant alloys have been developed by trial and error, which has led to a vast bank of empirical data on which current attempts at alloy improvement are usually based.

The high temperature corrosion of an alloy is recognized to occur in three stages: transient oxidation; steady-state oxidation; and spallation (or breakaway corrosion) [10]. The scale that initially forms on an alloy is usually dominated by oxide phases that have a temporary existence, which are referred to as transient oxide phases. During this early stage, all of the different metals in an alloy can produce oxides that contribute to the formation of the scale. For example, a typical stainless steel contains Fe, Ni, and Cr. All of the oxides of these elements, FeO, Fe_3O_4, Fe_2O_3, NiO and Cr_2O_3 can, in principle, contribute to the composition of the immature scale. The energetically most stable oxide will eventually dominate the scale composition to produce a steady-state (or mature) scale. In the above example Cr_2O_3 is the most stable oxide. During the steady-state stage most of the new scale growth is composed of the most stable phase. Ultimately the protective scale fails by either (a) the scale debonding from the substrate, (b) the alloy becoming depleted of the steady-state scale forming element, or (c) chemical attack from atmospheric or metallurgical impurities (e.g. S, Na).

The failure mode pertinent to this thesis is spallation. Spallation is when a scale cracks and debonds from the substrate. Spallation is often accompanied by visibly observable flakes of oxide that have physically separated from the alloy. When an alloy loses its scale, the associated loss of protection can cause very rapid corrosion. The principal cause of spallation is believed to be scale stress.

Spallation is often observed when an alloy is cooled from its corrosion temperature. The explanation proposed for this behavior is that the thermal expansion difference between the oxide scale and metallic alloy generates a stress. Apriori there

are a large number of other possible contributions to residual-stress accumulation and relaxation, such as growth stresses, creep, scale phase composition, scale and alloy phase transformations, debonding, cracking, etc. A full treatment of this phenomenon is therefore extremely complex, especially when it is difficult to make initial assumptions regarding which effects are likely to contribute most strongly in a given instance.

Commercially available alloys often contain, in small quantities (e.g. <1%), what are commonly referred to as reactive elements (e.g. Zr, Y, and Hf) that improve corrosion resistance. Surprisingly, even though the inclusion of these reactive elements is done routinely, the mechanism by which the reactive elements improve corrosion resistance is still not known. However, numerous theories ranging from an improvement of scale adhesion to stress reduction mechanisms have been proposed to explain the reactive element effect.

Some Common Characterization Techniques

This thesis is an evaluation of inelastic light scattering techniques as tools for investigating the corrosion of metallic alloys. Here, for the sake of comparison, a short survey of some common characterization techniques is discussed. We also would like to use the survey to help further illustrate the complex issues that are associated with scales.

Thermogravimetry

As a metal or alloy oxidizes the accumulated scale causes a net weight gain of the sample. This can be measured by incorporating a micro-balance in the furnace where the corrosion is occurring [11]. Thermogravimetry is used to determine the scale growth rate, and can be used to study the reaction kinetics. Isothermal scale growth

rates are frequently parabolic with time, but depending on the growth kinetics they can also demonstrate linear or logarithmic behavior [11]. Weight gain data can be difficult to interpret quantitatively because changes in oxide phases and/or scale morphology can affect the growth kinetics. Also, if a volatile oxide forms or spallation occurs, the data may exhibit a weight loss [11].

This technique has been used to study the reactive element effect [12]. Some reactive element free alloys are prone to rampant spallation, and exhibit a substantial weight loss. When these alloys are doped with small amounts of a reactive element they no longer exhibit a weight loss. The observed spalled flakes from reactive element free alloys in conjunction with thermogravimetry results led to a definition of the reactive element effect: e.g. the reactive element improves scale adhesion [13].

X-Ray Diffraction

X-ray diffraction (XRD) is a common technique for the characterization of crystalline solids. Incident x-rays are reflected by crystallographic planes. The reflections constructively interfere to produce a characteristic pattern that is related to the interatomic spacing (d-spacing) of the crystallographic planes in the material [14]. By rotating the crystal, each of the d-spacings for all of the crystallographic orientations can be determined. Because scales are polycrystalline, with randomly oriented grains, all of the crystallographic orientations are simultaneously represented in a XRD spectrum (i.e. powder diffraction). Powder diffraction spectra can be acquired, from a scale, in a $\theta-2\theta$ geometry. The Bragg reflections from the scale can be compared to those from standard bulk oxides, to produce a qualitative assessment of the scale composition. A quantitative result can be obtained by analyzing the scale diffraction spectra with Rietveld refinement techniques.

A less common use of XRD is the measurement of scale strains. The expansion or contraction of a scale will produce a change in the d-spacing of the constituent oxides. Which can be determined by a shift in the 2θ angle of each Bragg reflection (Bragg's Law $n\lambda=2d\sin\theta$). Data using this technique will be presented in Chapter V.

One of the problems of thin film characterization is that scattering volumes are small, thus reducing the signal strength of the scattered radiation. For XRD measurements, the scale's thinness can be partially compensated by using samples with large surface areas. A second problem with XRD from films is that Bragg reflections from the underlying substrate are also present in the film spectrum. This can complicate the data analysis.

Scanning Electron Microscopy and Energy Dispersive X-Rays

Details of a scale's morphology can be obtained by using the high spatial resolution (10x to 300000x [15]) of scanning electron microscopy (SEM). The technique scans a focused electron beam across the surface of a scale (sample in vacuum). The incident electrons interact with the sample to produce three types of scattered radiation that are used for imaging; secondary electrons, back scattered electrons, and X-rays.[15] The secondary electrons and the back scattered electrons are produced by inelastic scattering from the atomic electrons, and elastic scattering from the atomic nuclei respectively. For the inelastic case, the scanning electrons transfer energy to an atomic electron. If a sufficient amount of energy is transferred, the atomic electron can be emitted from the sample, where it is detected and used for imaging. The back scattered electrons scatter from the atomic nuclei without a loss of kinetic energy. The elements with higher atomic numbers are stronger elastic scatterers. Thus the sample can be mapped as a function of atomic number. The third source of radiation

used in SEM imaging is X-rays. The technique is referred to as energy dispersive x-ray analysis (EDX). A core electron in the sample can become excited by an incident electron. When returning to its ground state the excited atom emits an x-ray with an energy specific to each element. The x-rays can be analyzed by an energy dispersive x-ray detector and used to identify the elements that produced them. EDX can be used for both imaging and the determination of elemental concentrations.

A wide range of valuable morphological information can be obtained from SEM/EDX measurements. By using secondary and back-scattered electrons a scale's grain structure and its grain boundaries can be mapped. The EDX can be used to determine the elemental concentration of an individual grain and in turn the oxide phase can be inferred. The secondary and back-scattered electrons can also detect pores, micro-cracks, and voids that may be present in the scale.

The scale morphology and grain structure can affect the diffusion rates of the cations and oxygen ions through the scale, in turn affecting the scale growth rates and growth kinetics. This can be of particular importance when the scale contains pores, micro-cracks, and voids, all of which can cause accelerated solid state diffusion.

Similarly to the XRD technique, analysis of EDX data requires considerable care because the scanning electrons can traverse the scale and interact with the substrate. This makes it difficult to separate the elemental concentrations of the scale from that of the underlying alloy.

Transmission Electron Microscopy

Transmission electron microscopy (TEM) utilizes a focused electron beam that is incident on a thin sample. The signal in TEM is from both undeflected and diffracted electrons that traverse the sample [16]. It is a very versatile technique that possesses a very high spatial resolution (50x to 10^6x [17]). The high resolution allows observation

of individual scale grains. The grain's oxide phase can be identified from its electron diffraction pattern and its morphological relation to the scale can be imaged by a variety of imaging modes. Although electron diffraction is conceptually similar to XRD discussed above, the quantitative analysis of the electron diffraction patterns is considerably more difficult. In contrast to EDX, where a grain's oxide phase is inferred from the elemental content, TEM's electron diffraction can identify a grain's chemical and crystallographic phase as well as the grain's crystallographic orientation [18] . TEM can also be used to investigate scale, pores, micro-cracks, and voids.

A significant drawback of TEM is the labor intensive sample preparation [19]. In order for electrons to be used in transmission, the sample has to be thinned to less than ~200nm [17]. The thinning process can take as long as a week and involves mechanical polishing, electro-polishing and ion milling. The time consumed and labor involved in sample preparation greatly reduces the number of samples investigated. Additional concerns with TEM sample preparation are that the thinning process can damage or contaminate the scale, and may drastically change the stress state of the as grown scale.

Raman Spectroscopy and Ruby Piezospectroscopy

Raman scattering has received little attention in the field of corrosion [12,20-37]. The reason for its limited use has been the long data acquisition times required to obtain suitable spectra from thin surface oxides. Because advances in detection systems, viz. multichannel CCD (charge coupled devices), have recently provided dramatic improvement in the sensitivity of Raman scattering experiments, we decided to reevaluate the technique as a tool for corrosion research.

The Raman effect is the inelastic scattering of light from atomic vibrations (i.e. phonons). Raman spectroscopy measures how atoms vibrate about their equilibrium

positions. The atomic vibrations are affected by chemical composition, crystalline phase, compound stoichiometry, and applied stress. Therefore Raman scattering has the potential of providing valuable information about scales. Early studies using Raman were successful in identifying some of the oxide phases in thick mature scales. We sought to determine if the new CCD detection systems could make Raman useful for the study of the thin scales that form during transient phase oxidation. Raman spectroscopy is also attractive because sample preparation is usually trivial, the technique is non-destructive and is applicable to micro-structural investigations.

The initial purpose of this research was to evaluate the use of Raman spectroscopy as a tool for the investigation of the oxidation of steels, in particular steels used in high temperature environments where oxidation is often the principal source of failure. However, during the Raman investigation it was observed that many of the scales that formed on aluminum containing alloys fluoresced when irradiated with a laser. The origin of some of the fluorescence was found to be due to the presence of ruby in the scale. Because ruby piezospectroscopy has a rich history in high pressure diamond anvil cell (DAC) research, it seemed likely to provide scale stress information. Thus, our research objectives were adjusted to include the evaluation of ruby piezospectroscopy as a tool for the investigation of scale stress.

This thesis contains a discussion of the mechanisms that give rise to the Raman effect, ruby fluorescence and ruby piezospectroscopy. It describes the equipment used to measure Raman, and fluorescence spectra. It presents the results that were obtained during the evaluation of both Raman spectroscopy and ruby piezospectroscopy. The thesis concludes with a summary of the advantages, drawbacks and potential applications of Raman spectroscopy and ruby fluorescence for the investigation of scale growth and failure.

CHAPTER II

BASICS CONCEPTS

When monochromatic light, of frequency ω_o, illuminates a solid material most of the light is either transmitted or reflected, however a small amount is scattered in all directions. Light scattering can be divided into two classes, elastic (or Rayleigh scattering) and inelastic. For the elastic case, the frequency (ω_s) of the scattered radiation has the same frequency as the incident light ($\omega_s = \omega_o$). For the inelastic case, the frequency of the scattered radiation is shifted from the frequency of the incident light ($\omega_s = \omega_o \pm \omega_i$). The Stokes and anti-Stokes processes are given by $\omega_s = \omega_o - \omega_i$ and $\omega_s = \omega_o + \omega_i$ respectively. For the propose of this thesis we are interested in how light is inelastically scattered by optical phonons. The measurement of this type of scattering is achieved by Raman spectroscopy. The optical phonons correspond to vibrations where the ions within each primitive cell are executing what is essentially a molecular vibration [38]. Hence, when we acquire Raman spectra from oxide scales, we are probing the molecular vibrations associated with the scale's chemical composition. Light is also inelastically scattered by acoustic phonons, and magnons. However, the measurement of this type of scattering typically requires Brillouin spectroscopy, and will not be covered here.

The phenomenon which we refer to as fluorescence, but is also referred to in text books as luminescence and photoluminescence, is due to electronic transitions in a material. The frequency (ω_e) emitted by a fluorescing material is a measure of the

energy ($\hbar\omega_e$) of the electronic transition that produced it. Even though $\omega_o \neq \omega_e$, fluorescence is not commonly referred to as inelastic light scattering because fluorescence requires an intermediate step of absorption. Fluorescence is also different than Raman scattering because it does not have Stokes and anti-Stokes components.

In this chapter we provide a classical description of the first order Raman scattering. We discuss the electronic transitions that give rise to ruby fluorescence. We also provide a description of ruby piezospectroscopy.

Raman Scattering in Crystals

Macroscopically, Raman scattering can be viewed as inelastic scattering by modulations in a material's electric susceptibility. This can be described by using classical electromagnetic theory [39, 40]. An incident electric field ($\mathbf{E}(\mathbf{k}_L,\omega_L)$) from a monochromatic light source induces a dipole moment per unit volume (i.e. polarization $\mathbf{P}$) in a solid, according to:

$$\mathbf{P} = \chi\, \mathbf{E}(\mathbf{k}_L,\omega_L) = \chi\, \mathbf{E}_o \sin(\mathbf{k}_L \bullet \mathbf{r} + \omega_L t) \qquad 2.1$$

where the electric field is described as a plane wave of frequency ω_L and wavevector $\mathbf{k}_L$. χ is the electric susceptibility tensor of the solid.

The induced dipoles which are much smaller than the emitted wavelength will radiate with intensity dI into a solid angle $d\Omega$ [41]:

$$\frac{dI}{d\Omega} = \left\langle \frac{d^2\mathbf{P}}{dt^2} \right\rangle^2 \frac{1}{4\pi c^3} \sin^2(\theta) \qquad 2.2$$

Where < > is the time average and θ is the angle between the dipole axis and the observation direction.

In solids the electric susceptibility χ is not a constant value since certain lattice vibrations (e.g. phonons) cause χ to vary. In the harmonic crystal approximation the jth lattice vibration (i.e. jth branch in the phonon dispersion relation) can be written in terms of the normal mode coordinate:

$$Q_j = Q_{jo} \sin (\mathbf{q}_j \bullet \mathbf{r} + \omega_j t) \qquad 2.3$$

Where the phonon frequency is ω_j and the phonon wavevector is $\mathbf{q}_j$.

For small amplitude vibrations χ is linear function of Q_j and can be expanded as a Taylor series.

$$\chi = \chi_o + \left(\frac{d\chi}{dQ_j} \right)_o Q_j + \ldots \qquad 2.4$$

Here χ_o is the susceptibility when the atoms in the lattice are in their equilibrium positions and $d\chi/dQ_j$ is the rate of change of the susceptibility with respect to the lattice vibration Q_j. Combining 2.1, 2.3, and 2.4 we obtain

$$\mathbf{P} = \chi_o \mathbf{E}_o \sin (\mathbf{k}_L \bullet \mathbf{r} + \omega_L t) +$$

$$(d\chi/dQj)_o \mathbf{E}_o Q_{jo} \sin (\mathbf{k}_L \bullet \mathbf{r} + \omega_L t) \sin (\mathbf{q}_j \bullet \mathbf{r} + \omega_j t) + \ldots \qquad 2.5$$

This expression can be rewritten by making use of a trigonometric identity.

$$\mathbf{P} = \chi o\, Eo \sin(\mathbf{k}_L \bullet \mathbf{r} + \omega_L t) +$$

$$1/2\, (d\chi/dQj)_o\, \mathbf{E}_o\, Q_{jo} [\cos\{(\mathbf{k}_L + \mathbf{q}_j)\bullet\mathbf{r} + (\omega_L + \omega_j)t\}$$

$$+\cos\{(\mathbf{k}_L - \mathbf{q}_j)\bullet\mathbf{r} + (\omega_L - \omega_j)t\}] \qquad 2.6$$

According to the classical theory the first term corresponds to the transmitted beam with frequency ω_L. The second term gives rise to Raman scattering of wavevector $\mathbf{k}_s$ and frequency ω_s, where:

$$\mathbf{k}_s = \mathbf{k}_L \pm \mathbf{q}_j \qquad 2.7$$

$$\omega_s = \omega_L \pm \omega_j$$

The first equation in 2.7 represents the conservation of wavevector and the second equation reflects the conservation energy, in the scattering process. The signs - and + correspond to Stokes and anti-Stokes scattering respectively. The quantity $(d\chi/dQ_j)_o$ is known as the Raman tensor. It is a second rank tensor whose form depends on the symmetry of the normal mode Q_j involved in the scattering process. If all the components of the jth Raman tensor are zero then the jth normal mode does not produce Raman scattering.

The energy of a phonon (~100 meV) is always small compared to the energy of the incident light (2.5 eV). Eq. 2.7 therefore implies $|\hbar\omega_s| \approx |\hbar\omega_L|$. The corresponding maximum wavevector which can be probed is $|\mathbf{k}_s \pm \mathbf{k}_L| \approx 2k_L$ which is $\sim 10^5$ cm^{-1} for visible light. Because this is small compared to the Brillouin zone dimension $|q| = 2\pi/a$ $\sim 10^8$ cm^{-1}, Raman probes the phonons very near the center of the Brillouin zone [42].

The main shortcoming of the classical treatment of Raman scattering is that it gives the wrong intensity ratio for the anti-Stokes to Stokes radiation. The correct ratio can be determined by quantum mechanical arguments [43]. Stokes scattering occurs when phonons in their ground state are excited into the first excited state (i.e. phonon creation). During this process a photon of energy $\hbar(\omega_L - \omega_j)$ is emitted. Anti-Stokes is the "reverse" process, a phonon in its first excited state relaxes into its ground state (i.e. phonon annihilation). A full quantum mechanical treatment shows that the intensity of the anti-Stokes scattering is proportional to the occupation number n_j of the excited state, which is known from Bose-Einstein statistics to be:

$$n_j = \frac{1}{\exp(\frac{\hbar\omega_j}{k_b T}) - 1} \qquad 2.8$$

The intensity of the Stokes scattering is proportional to n_j+1, so the correct ratio for the intensity of anti-Stokes to Stokes radiation is:

$$\frac{\text{anti - Stokes}}{\text{Stokes}} = \exp(\frac{-\hbar\omega_j}{k_b T}) \qquad 2.9$$

Consequently, the Stokes scattering is more intense than the anti-Stokes scattering.

In order to bring out the physical significance of wavevector conservation (Eq. 2.7) we will reexamine it using arguments based on conditions for constructive interference [42]. The normal mode coordinate (Q_j) can be viewed as a wavelike disturbance in a continuous medium. If the disturbance were 'frozen' in time (i.e. fixed t in Eq. 2.3) the medium would appear like a periodic variation of density, with period $d=2\pi/q$. If light of wavelength λ were incident on such a medium it can be considered to be "Bragg reflected" from the density variations (Figure 1) [42].

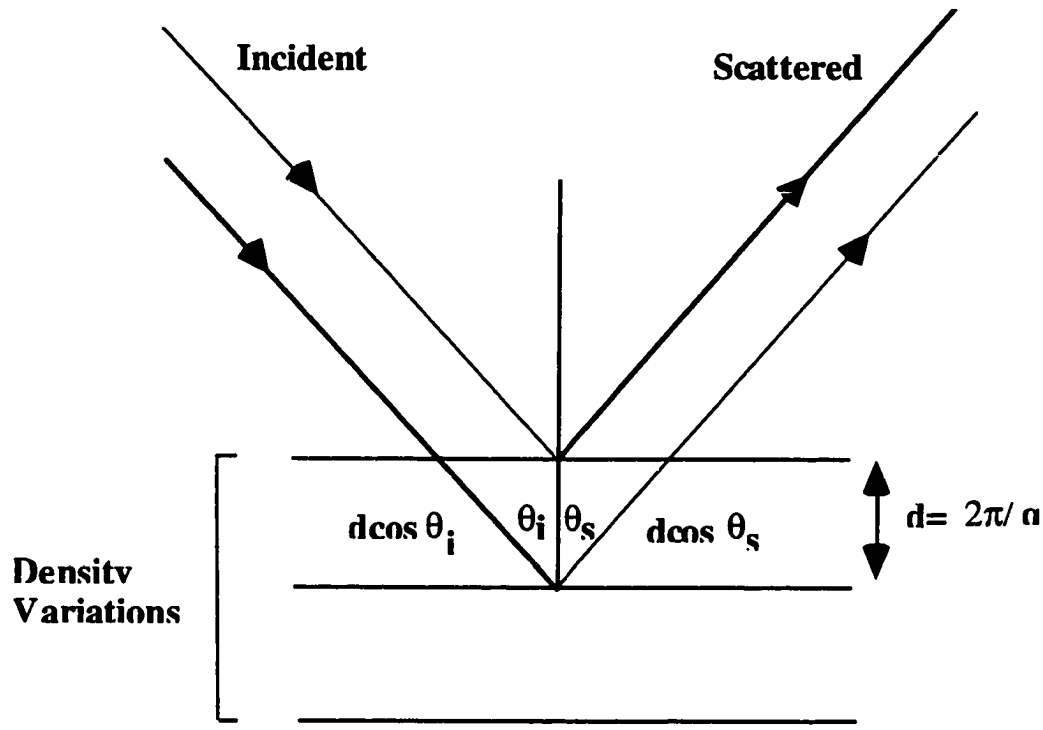

Figure 1. Scattering From Susceptibility Modulations.

The requirement for constructive interference demands that the optical path length difference of two rays be equal to λ. This can be determined from Figure 1 and written as;

$$n\, d \cos\theta_s + n\, d \cos\theta_L = \mathbf{d}\cdot(n\mathbf{e}_s - n\mathbf{e}_L) = \lambda \qquad 2.10$$

where n is the index of refraction, and $\mathbf{e}_L$ and $\mathbf{e}_s$ are unit vectors in the directions of incident and scattered light respectively. By multiplying both sides of 2.10 by $2\pi / \lambda\mathbf{d}$ we obtain the equation for wavevector conservation for Stokes scattering.

$$\mathbf{k}_s - \mathbf{k}_L = \mathbf{q} \qquad 2.11$$

A similar argument can be used to describe wavevector conservation in the case of anti-Stokes scattering. The above arguments show that the origin of wavevector conservation is the constructive and destructive interference between the radiation from the dipoles that compose the medium. The scattering from the susceptibility modulations that produce constructive interference contribute to the Raman spectrum (i.e. Raman active phonon). Conversely, susceptibility modulations that give rise to scattering that destructively interfere do not contribute to the Raman spectrum (i.e. Raman inactive phonon).

Disorder induced Raman scattering occurs in spectra acquired from crystals with defects, such as vacancies and interstitials. The presence of defects relaxes the condition for constructive and destructive interference so that scattering from the Raman active modes becomes less intense, and Raman inactive vibrational states become Raman active.

Ruby Fluorescence

When a semiconductor is illuminated with photon energy $\hbar\omega_L$, electrons in the valence band can be pumped into the conduction band, thus leaving a hole in the valance band (presupposing $\hbar\omega_L > E_g$). After relaxing to the bottom of the conduction band, the excited electron can radiatively recombine with a hole to produce a photon with energy ~ E_g, i.e. fluorescence. In the case of insulators (e.g. α-Al_2O_3) when the incident photon energy (~1.7 to ~3 eV visible light) is less than the bang gap energy (~9 eV), band gap fluorescence does not occur. Impurities in an insulator, however, can have electronic energy states that fall in the band gap. These states contribute to both absorption and emission of photons. Here we will describe the fluorescence of

ruby (Figure 2), which is Cr doped sapphire (α-Al_2O_3). The ruby fluorescence results from excitations of the Cr 3d electrons [44, 45] when Cr atoms are substituted for Al atoms in α-Al_2O_3.

When Cr^{3+} ions are substituted for octahedral coordinated Al^{3+} ions in α-Al_2O_3 the electric field of the six nearest neighbor oxygen ions (i.e. crystal field) deform the 3d orbitals. The effect of the crystal field is to split the orbital degeneracies. Additional splitting occurs due to spin-orbit interactions. It can be shown that the 28-fold degenerate ground state of Cr^{3+} ion is split by the crystal field into three levels (two 12-fold and one 4-fold). These levels are in turn further split by the spin orbit coupling yielding a total of 9 levels [44,45]. A few of theses states are plotted in Figure 3.

Most of the Cr^{3+} ion's energy states give rise to absorption bands, however few of these decay radiatively. When monochromatic blue light (E_L = 2.6 eV) illuminates

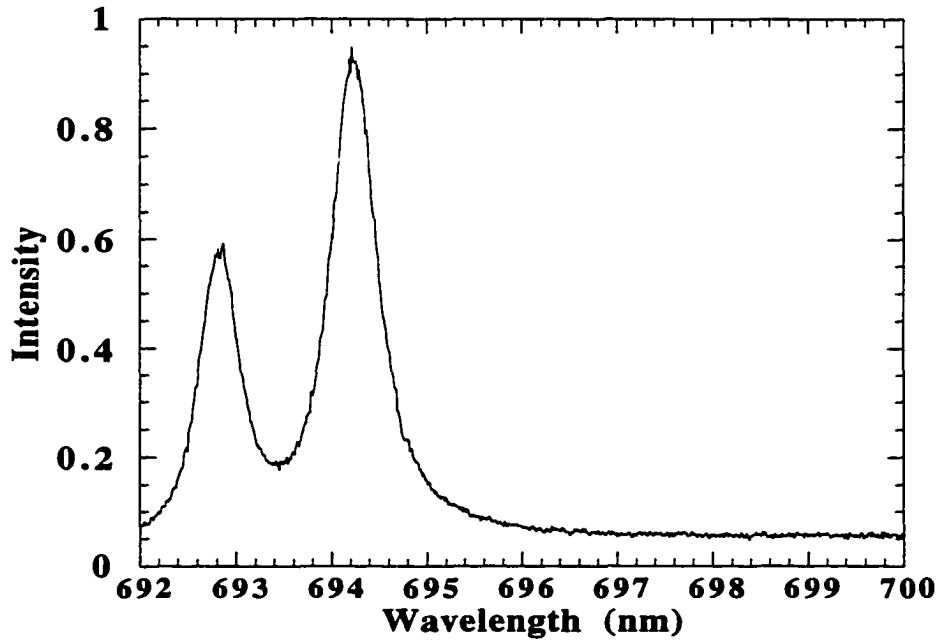

Figure 2. Spectrum of the Characteristic Ruby Fluorescence.

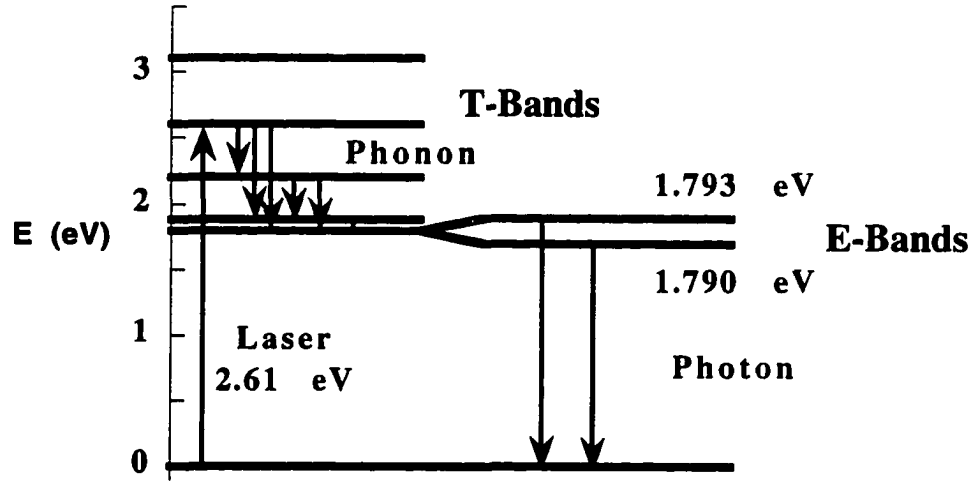

Figure 3. Electronic Levels of Cr^{+3} in α-Al_2O_3.

ruby the 3d electrons are pumped into the higher energy T-bands of the electronic energy spectrum (Figure 3). Most of the excited atoms can decay to lower energy states by nonradiative processes [45]. The nonradiative energy transitions occur by means of phonons - effectively due to the strong coupling between the electronic states and the vibrational lattice. Nonradiative decay is very probable between the closely spaced T-bands and between the T-bands and E-bands (Figure 3). However, the energy gap between E-bands and the ground state is too large for nonradiative transitions. That is to say, there are no phonons of energy 1.79 eV available for nonradiative decay. Consequently the E-states to the ground state energy transitions occur by means of photons which produce the characteristic ruby fluorescence shown in Figure 2. Because the excited electron undergoes several nonradiative energy transitions before it arrives at the radiative E-states to ground state transition, the frequency of the ruby fluorescence is unaffected by the frequency of the pumping light.

Ruby Piezospectroscopy

Because the 3d electrons are on the outside of the Cr^{+3} ions, they are particularly sensitive to changes in the crystal field produced by the neighboring atoms [46]. Because an external stress affects the atomic positions, it also produces changes in the frequency of the ruby fluorescence. The shift in frequency ($\Delta\nu$) of the fluorescence peaks due to stress can be described by [47]

$$\Delta\nu = \pi_{ij}\,\kappa_{ij} \qquad 2.12$$

In which π_{ij} are piezospectroscopic coefficients and κ_{ij} is the stress in the crystal reference frame. Because scales are polycrystalline, it is more convenient to deal with stresses in the substrate frame (σ_{ij}). We can write the stress in the crystal reference frame as:

$$\kappa_{ij} = a_{ik}\,a_{jl}\,\sigma_{kl} \qquad 2.13$$

where the a_{ij} are the direction cosines of one set of coordinate axes relative to the other; equivalently a_{ij} are the components of the rotation matrix. Thus Eq. 2.12 becomes:

$$\Delta\nu = \pi_{ij}\,a_{ik}\,a_{jl}\,\sigma_{kl} \qquad 2.14$$

where σ_{kl} is now in the reference frame of the substrate.

The piezospectroscopic coefficients have been measured under uniaxial compression and are listed in Table 1. The measurements of the π_{ij} have also

demonstrated that the off-diagonal terms of the piezospectroscopic tensor are zero (i.e. $\pi_{11} \neq \pi_{22} \neq \pi_{33}$ and $\pi_{ij} = 0$ when $i \neq j$) [47]. Eq. 2.14 can therefore be simplified to.

$$\Delta\nu = \pi_{ii}\, a_{ik}\, a_{il}\, \sigma_{kl} \qquad 2.15$$

The assumption of random orientation of the grains in a scale (an approximation borne out by X-ray investigations in Chapter V) allows an average to be made of all

Table 1

Piezospectroscopic Coefficients (cm^{-1}/GPa)

	π_{11}	π_{22}	π_{33}	$\pi_{11}+\pi_{22}+\pi_{33}$	reference
R1	2.56	3.50	1.53	7.59	47
R1	2.77	3.41	1.17	7.35	author
R2	2.65	2.80	2.16	7.61	47
R2	2.18	2.87	2.09	7.14	author
R1				7.53	48

possible rotation matrices ($\langle a_{ik}\, a_{il} \rangle = 1/3\, (\delta_{kl})$)[46]. Hence Eq 2.15 becomes

$$\Delta\nu = \pi_{ii}\, \sigma_{jj} / 3 \qquad 2.16$$

$$\Delta\nu = (\pi_{11} + \pi_{22} + \pi_{33})(\sigma_{11} + \sigma_{22} + \sigma_{33})/3$$

The quantity $(\sigma_{11} + \sigma_{22} + \sigma_{33})/3$ is the hydrostatic stress (σ_H) in the scale, thus

$$\Delta\nu = (\pi_{11} + \pi_{22} + \pi_{33})\, \sigma_H \qquad 2.17$$

is the frequency shift due to hydrostatic stress in a polycrystalline system.

Strains in the scales measured at room temperature are due mainly to thermal mismatch between scale and substrate. In these cases the resulting stress in the scale is biaxial where two of the σ_{ij} in Eq. 2.16 are equal and the third is zero. This leads to

$$\Delta\nu = 2/3 \, (\pi_{11} + \pi_{22} + \pi_{33}) \, \sigma_{in} \qquad 2.18$$

which allows us to extract the biaxial stress.

CHAPTER III

EXPERIMENTAL EQUIPMENT AND PROCEDURES

In this chapter experimental equipment and experimental procedures used during this work will be described. Much of the work relied on standard, commercially-available equipment and will not be described in detail. Rather, the specific aspects of the equipment that make the work possible will be described. First a description is given of the geometrical considerations which determine the conditions under which Raman and fluorescence spectra are recorded. The heart of the experiments, the spectrometer, will only be schematically described but emphasis will be placed on the particular performance features necessary for this work. Similarly, the CCD (charged coupled device) detection system will not be technically described, but rather its performance will be compared to the more conventional photomultiplier detection systems. Finally, details relating to sample preparation and heat treatments will be presented.

Experimental Setup

When planning a Raman scattering experiment one has a wide variety of sample geometries to choose from. This versatility is useful in single crystal investigation, where one can probe the symmetry of the Raman modes. Our samples however, are polycrystalline with small grains (< 0.5 μm), which makes probing vibrational mode symmetries impossible. The second restriction to the experimental geometry is that the samples are films on opaque substrates. The opaque substrate limits our options to a variation of the back-scattering geometry.

The scattered light from a material has both elastic and inelastic components. The elastically scattered light is always many orders of magnitude more intense than the inelastically scattered light. A Raman measurement attempts to investigate the inelastic scattering by separating it from the elastic scattering. Diffuse elastically scattered light needs to be avoided whenever possible.

When using a 'direct' back-scattering geometry the incident laser beam impinges the sample along the direction normal to the film surface and the scattered radiation is also collected along the surface normal (Figure 4). Back-scattering probes the phonons with wave vectors $\mathbf{q}= 2\ n\ \mathbf{k}_i$, where n is the index of refraction of the film and $\mathbf{k}_i$ is the wavevector of the incident laser light. The wavevector of the reflected laser light is $\mathbf{k}_r = -\mathbf{k}_i$. This setup works reasonably well for samples with smooth surfaces, however the surfaces of thermally grown scales are rough. A rough sample will cause a large amount of elastically diffuse scattered light distributed around the reflected laser beam ($\mathbf{k}_r$). The frequency analysis becomes difficult when a large amount of elastically scattered light enters the collection optics.

To reduce the intensity of the elastic contribution we modify the direct back-scattering geometry by rotating the incident laser beam to an angle of about 45° with respect to the surface normal (Figure 5). The angle that the reflected beam makes with the surface normal is -45°, consequently most of the diffuse scatter avoids the collection optics.

Figure 6 shows a block diagram of the experimental setup used to acquire macro-Raman and macro-fluorescence spectra. The sample, typically an oxidized alloy or compacted powder, is illuminated with a focused laser beam. The area of illumination is a circular spot with a diameter of about 80 μm. The laser used for this study was a krypton gas laser (model 171, Spectra-Physics). This laser can produce monochromatic light of several frequencies, ranging from blue to red. Because our

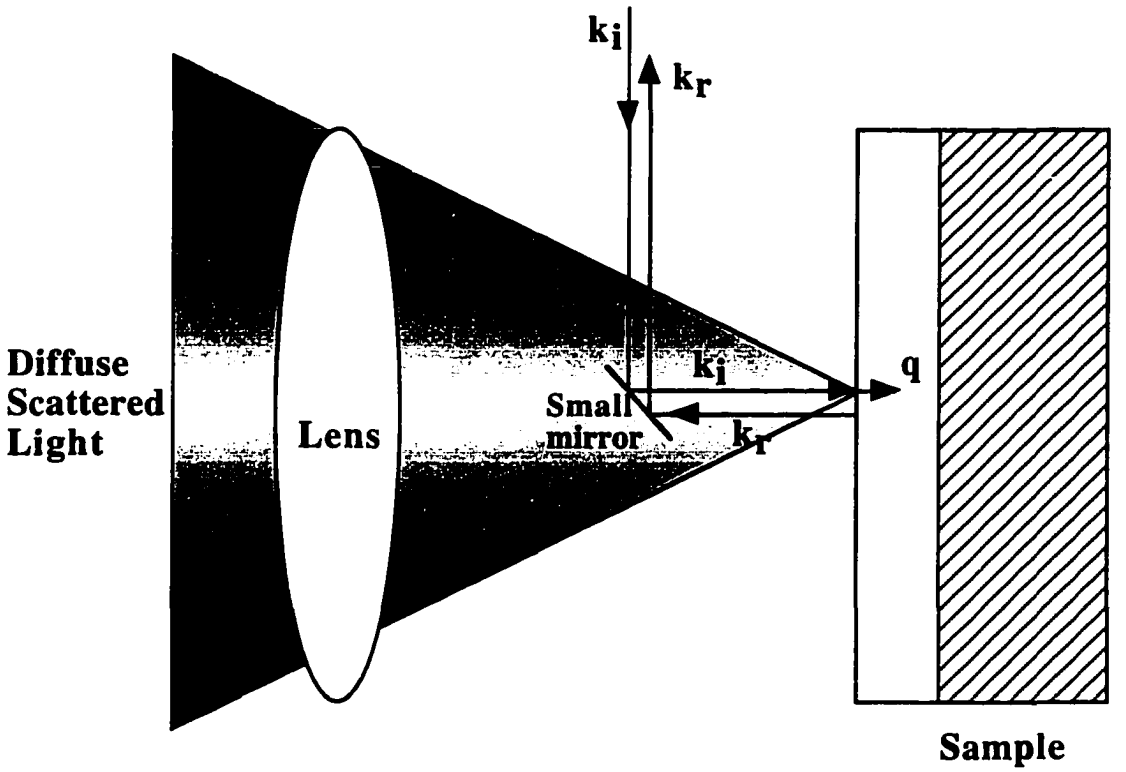

Figure 4. Direct Back-Scattering Geometry.

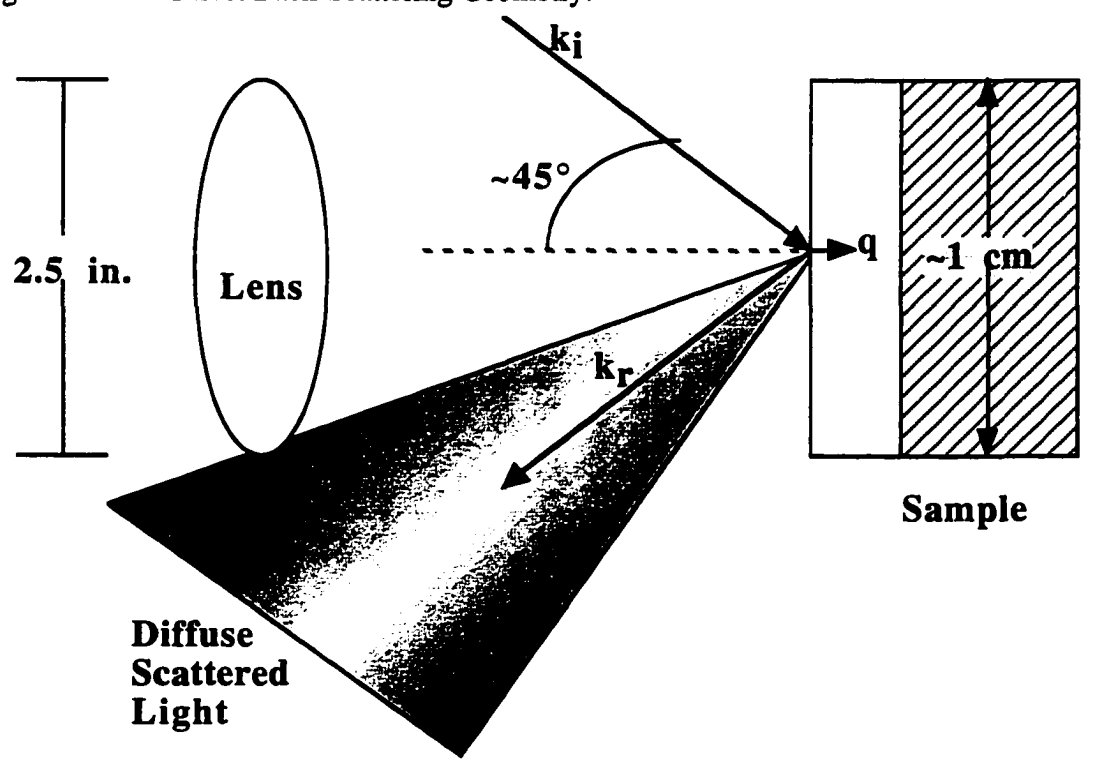

Figure 5. Modified Back-Scattering Geometry.

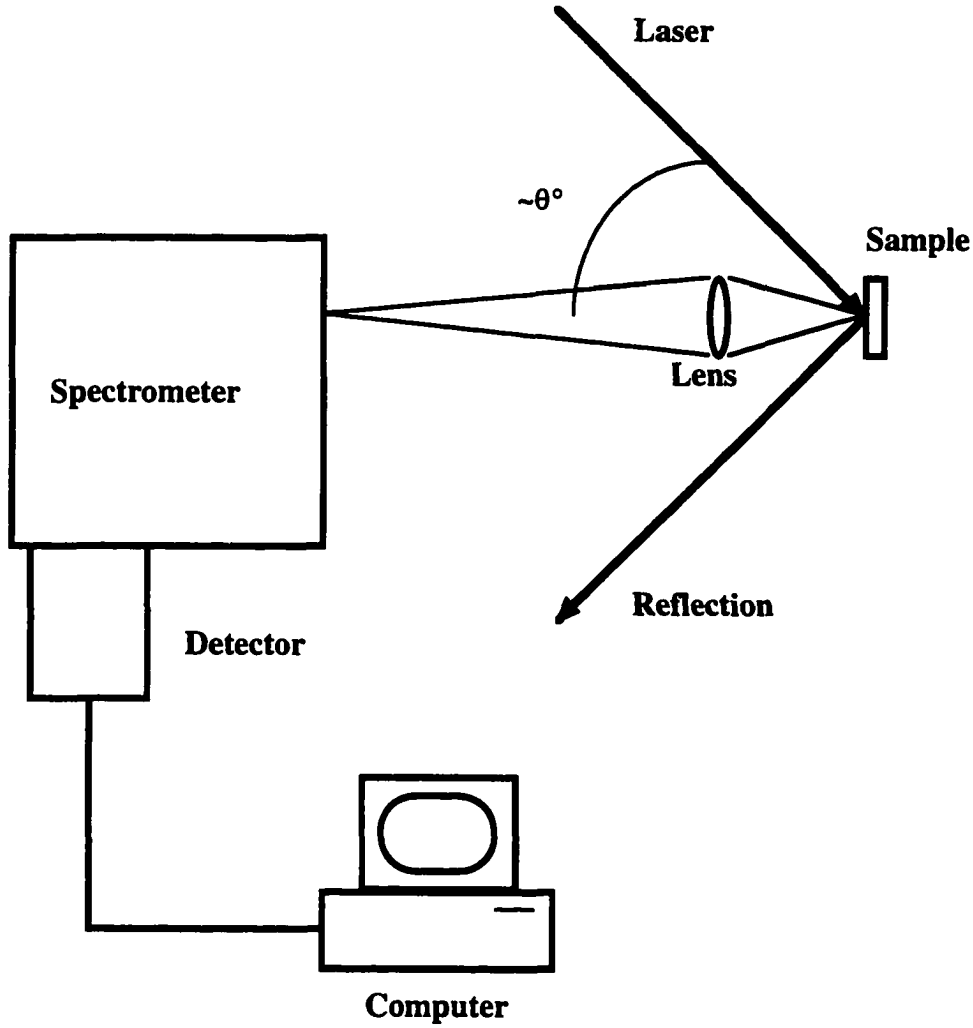

Figure 6. Experimental Setup for Both Macro-Raman and Macro-Fluorescence.

spectrometer and detector have a larger coverage in the blue end of the spectrum (Table 2 [49]), we did all our work with the krypton's 476.2 nm laser line. The laser power employed ranged between 50 and 100 mW. The angle θ that the incident beam makes with respect to the sample surface normal was in the neighborhood of 45°. The scattered light is collected along the sample surface normal with a camera lens (f number 2.8). The collection lens is positioned in order to avoid the reflected laser light. The collection lens focuses the scattered light onto the entrance slit of a spectrometer

(T64000, Jobin Yvon). The spectrometer frequency-analyzes the scattered light, by using diffraction gratings to spatially separate the various frequencies. The resulting spectrum is imaged onto the surface of a CCD detector. The particular 1 x 1 inch CCD used for this study was a Princetion Instruments LN/CCD-1024TKx. The array size is 1024 X 1024 pixels, and it is liquid nitrogen cooled. The detector sends an electronic signal to a computer where data acquisition software produces a digital representation of the spectrum.

Table 2

Coverage on 1 Inch CCD (1800g/mm Gratings)
T64000, Jobin Yvon

Central Frequency (nm)	Band Width (cm^{-1})
350	1594
400	1182
450	914
500	708
550	566
600	453
650	367
700	296
750	240

In order to acquire micro-Raman and micro-fluorescence spectra, the collection optics in Figure 6 are replaced with an optical microscope (BHSM-L-2, Olympus). Because the sample having an opaque substrate the microscope had to be used in the reflection geometry. Here the objective lens (typically a 100 x) is used to both focus

the laser light to a spot size of about 1 μm and to collect the light scattered from the sample. The micro- set up was found to produce Raman spectra of lower quality than the macro- set up, due to the very intense contribution of elastically scattered light. The ruby spectra were not usually affected by the elastically scattered light, because of the large frequency difference between the red ruby and blue elasticly scattered light. Again the spectrometer is used for frequency analysis and the CCD is used to measure the spectrographic output.

Spectrometer

The light scattered by the sample was analyzed by a triple diffraction grating spectrometer. Figure 7 is a schematic depiction of such a device. The three gratings are synchronously driven by stepper motors that are computer controlled, however the dispersion is not additive. Because we are using a 1 inch CCD, the first two gratings are used for the stray light rejection and only the third grating is used for the frequency selection.

The light coming from the entrance slit (typically 200 μm wide) is frequency dispersed by the first grating. The spectrum produced by grating 1 is imaged onto the intermediate slit 1. This slit is typically set to a width of about 25000 μm (1 inch), and functions as a optical band pass filter. This slit removes both high and low frequency light. Its frequency width can be determined from Table 2. This is the first step in removing the elastic scattering from the inelastic contributions. The central frequency and the band pass are set such that most of the elastically scattered light is rejected at this slit, while the inelastically scattered light, in the frequency range of interest, passes through. Grating 2 collects the dispersed light that passes through intermediate slit 1 and reassembles it into a narrow beam. That is to say, grating 2 un-disperses the light, and focuses (all frequencies) onto the intermediate slit 2 (typically 200 μm wide).

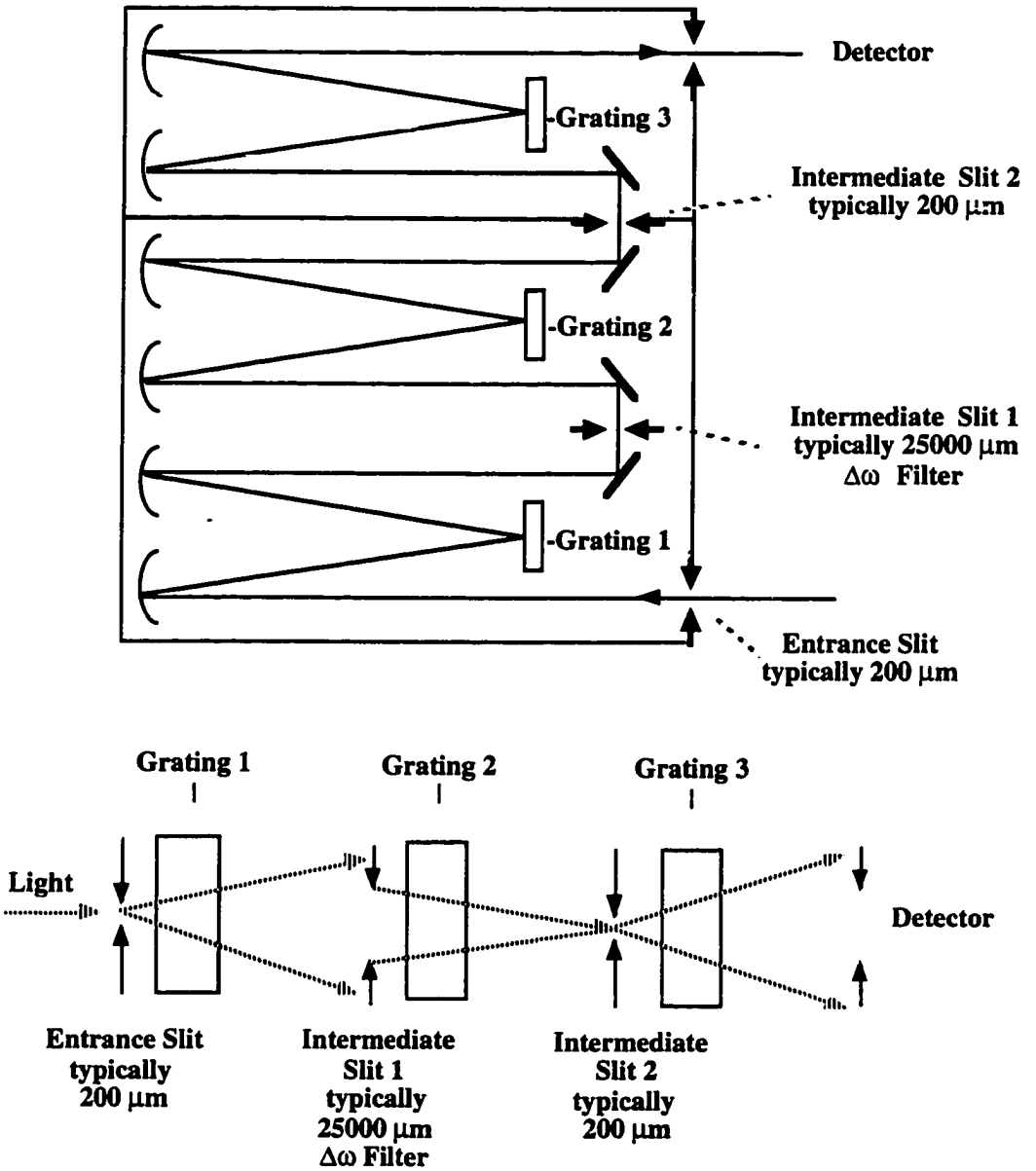

Figure 7. Schematic of a Triple Diffraction Grating Spectrometer.

Any unwanted leakage of elasticity scattered light is again rejected at this slit. Grating 3 re-disperses the light and images the spectrum onto the 1 inch CCD, where a filtering process similar to the one at intermediate slit 1 removes any remaining elasticity scattered light. The 1024 pixel wide CCD performs like a multichannel analyzer.

Detectors

Prior to the recent development of the CCD, the detector used for Raman spectroscopy was the photomultiplier tube (PMT). The PMT is based on the photoelectric effect, while the CCD is a two dimensional array of photo diodes which act as a position sensitive detector. The PMT utilizes single channel detection while the CCD utilizes multichannel detection. It is the multichannel feature of the CCD that leads to its much higher efficiency compared to that of the PMT (Figure 8).

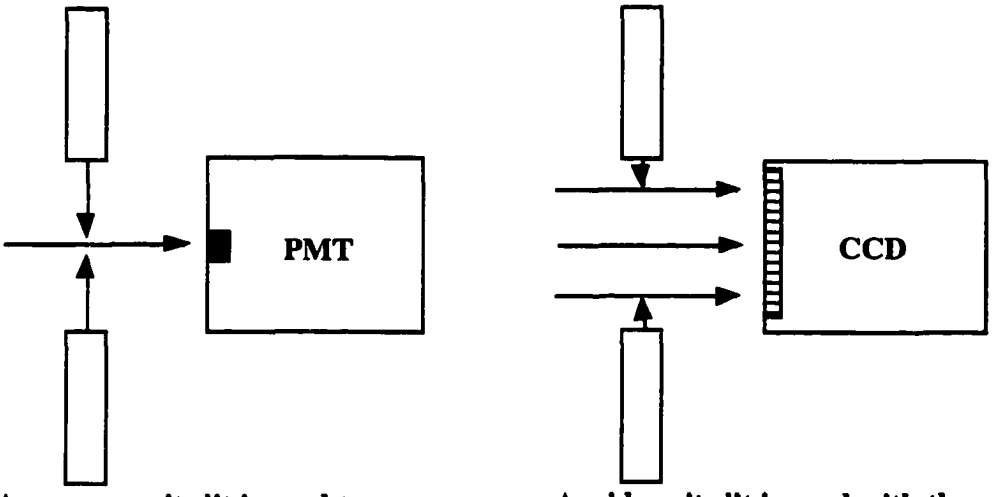

Figure 8. Exit Slit Comparison Between PMT and CCD.

For single channel operation the exit slit of the spectrometer is reduced to about 50 μm, which reduces the band pass in the blue to about 1.6 cm^{-1}. The exit slit width for operation with a 1 inch CCD is 25000 μm, from Table 2 the corresponding band pass is about 800 cm^{-1} Thus the multichannel detector has a spectral throughput that is 500 times larger than the single channel.

The procedure for acquiring a 800 cm^{-1} wide spectrum using a PMT, with the parameters described above, is as follows. The spectrometer is parked at a frequency, 21000 cm^{-1} (= 476.2 nm) for example. A one second exposure will produce one data point. Then the spectrometer has to be repositioned at 21001.6 cm^{-1} (step of one band width 1.6 cm^{-1}) for the next one second exposure and data point. After 500 steps a 800 cm^{-1} wide spectrum containing 500 data points is produced. When using a CCD, each column of pixels represents a data point, or a single channel. For the CCD described above, a one second exposure produces 1024 data points and a spectrum 800 cm^{-1} wide (Table 2).

Alloy Preparation and Oxidation

Small square samples (1 cm^2 or smaller) were cut from larger alloy sheet stock (~1 mm thick). The surfaces of each sample was polished with successively finer polishing grit (diamond or alumina). A typical grit series were 30 μm, 12 μm, 6 μm and 1 μm. Typically the surface produced by commercially-available automatic lapping equipment was sufficiently flat for most of the experiments. After polishing, the samples were ultrasonically cleaned first in acetone and then in methanol.

Some of the investigations involved studying corrosion at microscopic distances from the edges of samples. This required that the intersection of two sample surfaces had to be as sharp as possible. Early attempts using standard polishing techniques often produced edges with large radii of curvature, typically ~20μm, which was unacceptable. In order to produce sharper samples edges careful blocking techniques had to be used. Figure 9 is a drawing of a jig that was used to minimize the edge rounding effect. The sample, with its two large polished surfaces, is sandwiched

between two large pieces of brass. Since most of the rounding occurs at the edge of the brass, sharp sample edges, typically ~1 to 2μm radius, are obtained.

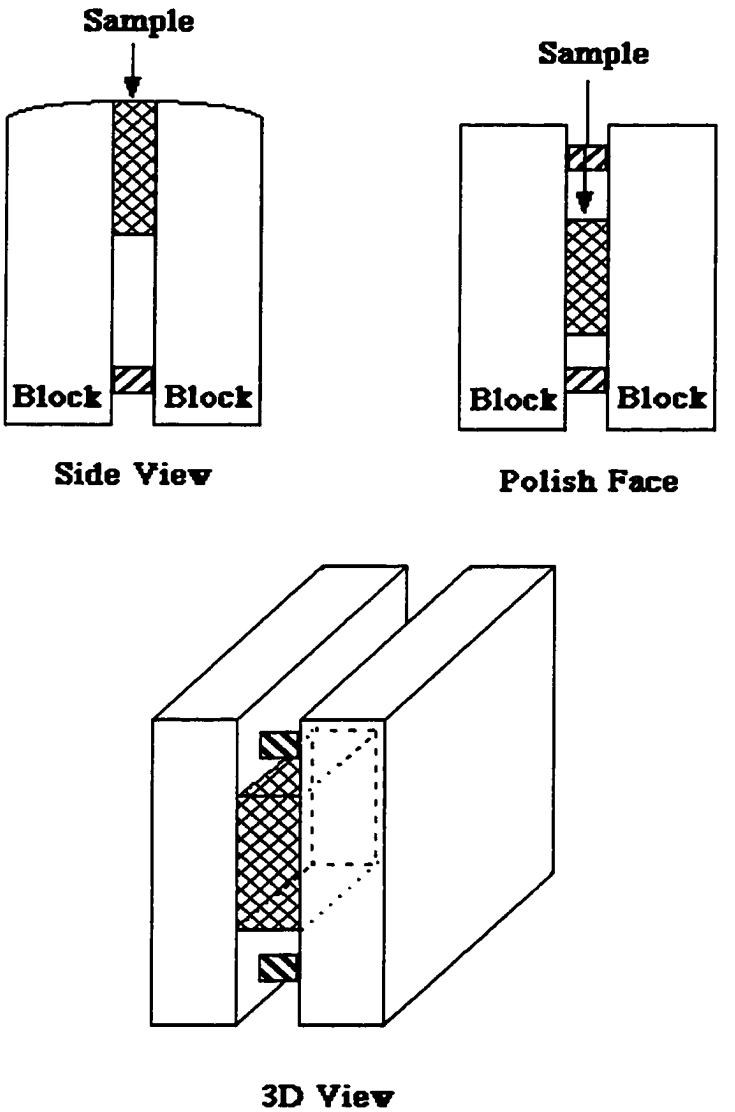

Figure 9. Polishing Jig. Minimizes the rounding of the sample's edges.

Since many high temperature applications of metallic alloys are under ambient atmospheric conditions, no attempt was made to control the chemical content of the gases in the oxidation environment. The samples were corroded in air using a Lindberg box furnace. The furnace was preheated to the desired temperature, and the room

temperature samples would be placed into the hot furnace. The corrosion that occurs during the period where the sample is heating from room temperature to furnace temperature is not considered, because the time required for the small samples to reach oxidation temperature is small compared to the heat treatment time. After the desired heat treatment, samples would be removed from the furnace into the room temperature lab atmosphere and allowed to cool (i.e. air quenching). In anticipation of thermally generated stress developing between the oxide scale and the alloy, the air quenching was assumed to produce the smallest creep effects. After the sample cooled to room temperature, spectra were acquired. The thermal histories of the samples were chosen to facilitate the evaluation of the light scattering technique. It was found that cyclic histories were more efficient for our purpose, since they eliminate the need for large numbers of samples, and the variation in the alloy composition that can occur from different lots. The precise thermal histories of the samples will be indicated with the presentation of the data (in Chapters IV and V).

During the course of this investigation it became necessary to fit our spectra to obtain accurate spectral positions. Although such fitting routines are commercially available, they typically handle a single spectrum at a time, and require a considerable amount of direct supervision. Because it was often necessary to fit many spectra (i.e. >50 per experiment) we developed a C++ program designed to fit multiple ruby spectra without supervision. Each spectra was fitted with two Lorentzian and a quadratic background, and up to 999 spectra could be fit in a single run. The use of our fitting routine not only greatly reduced the labor intensive fitting procedure, but the peak position thus obtained also reduced the experimental errors.

CHAPTER IV

RAMAN SCATTERING AND SCALE PHASE IDENTIFICATION

Introduction

As discussed in the introduction, the purpose of this thesis was to evaluate the use of optical techniques as tools for the investigation of the oxidation of steels. Of particular interest are steels used in high temperature environments where oxidation is often the principal source of failure. The objective is to utilize these techniques to assist in understanding the complex, and often not well understood, issues which occur during oxidation and which are not fully addressed by other techniques.

In this chapter the Raman scattering technique will be evaluated. There are two aspects to this evaluation, one is to determine if the technique is capable of detecting the weak signals expected from the thin scales which form on steel surfaces, the second is to see if the information obtained is relevant to improve our understanding of oxidation. Raman scattering has received little attention in the field of corrosion [12, 20-37]. The reason for its limited use has been long data acquisition times, which are required to obtain suitable spectra from thin surface oxides. Because advances in detection systems, viz. multichannel CCD (charge coupled devices), have recently provided dramatic improvement in the sensitivity of Raman scattering experiments, we decided to reevaluate the technique.

The first step in the evaluation was to explore the sensitivity of our particular Raman equipment to a thin scale. This was accomplished by measuring a ~1 cm square ~1 mm thick coupon of commercially available stainless steel before and after oxidation (Figure 10). Prior to oxidation the sample was polished with 30 μm diamond paper.

The corrosion was carried out by heating the sample to 900°C for 1 hr, in air. Spectra were acquired for 500 sec at room temperature, using the multichannel CCD.

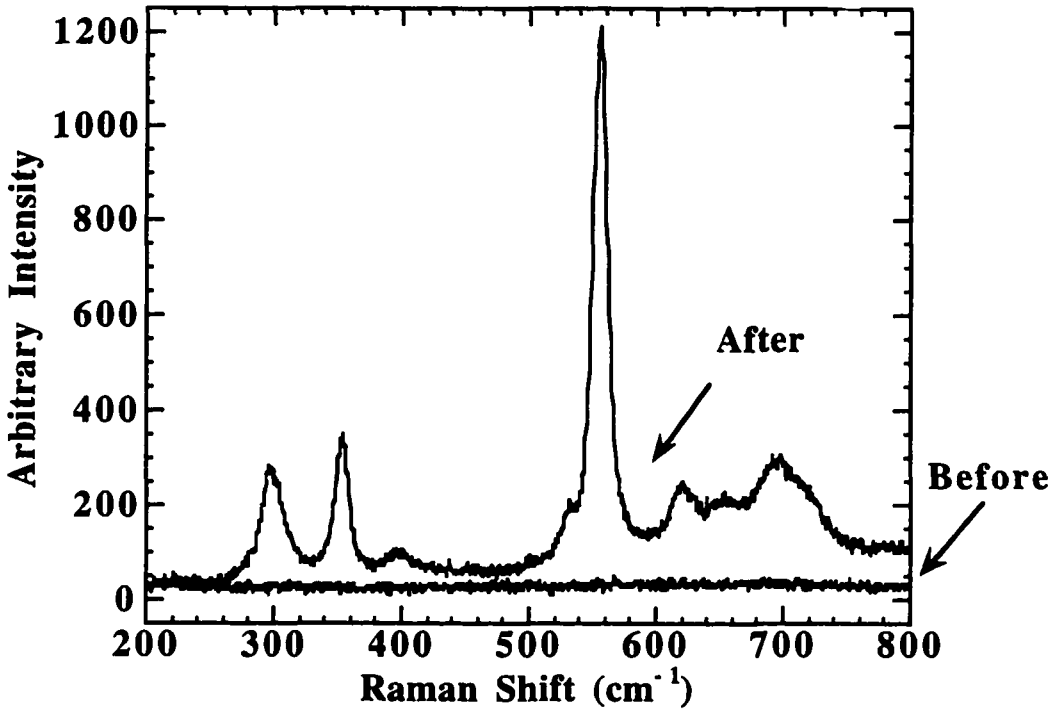

Figure 10. Raman Spectra From Stainless Steel. Spectra acquired, using a multichannel CCD, before and after the sample was oxidize, in air, at 900°C, for 1 hr.

The spectra from the unoxidized sample is featureless. Through the course of this study it was observed that bare metals and alloys consistently produced a featureless spectra. This is not surprising because the scattering volume in a conductor is small, due to the short penetration depth of light. It is also consistent with the fact that most alloys have an underlying BCC or FCC structure, both of which have no Raman active modes. However the oxidized sample shows a strong Raman signal, where all the peaks can be attributed to the scale. Figure 10 not only illustrates clearly that Raman scattering does provide information about the oxide scale but also that this information requires only 8 min to acquire. The equivalent spectra using photon

counting technology would require an estimated 3 hrs to acquire. Because of the short acquisition times, the lack of any sample preparation and the non-destructive nature of the technique, it is clear that if the information extracted from the Raman spectra can be shown to be useful in understanding the oxidation process, then Raman spectroscopy has a strong potential of becoming a powerful tool in such investigations.

The remainder of this chapter will be devoted to the interpretation of spectra such as that shown in Figure 10. Since the steels of interest are fabricated with Fe, Ni, Cr, and Al, it is obvious that the scales must be composed of oxides of these elements. The nrxt step is to accumulate spectra of known oxides to compare with Figure 10; this is outlined in the following section. Results from a study of the oxidation of elemental metals, and alloys of increasing complexity will then be presented. The chapter ends with a summary of the information extracted, using Raman scattering, about the oxidation process.

Oxide Standards

Raman scattering measures optical phonons corresponding to the normal modes of atomic vibrations in a material. Because most materials have unique vibration states, the Raman spectra from different oxides are usually quite distinct. That is to say each material has its own "fingerprint" spectrum and in principle it is simple to identify and track the evolution of various constituents in the oxide scale.

Our investigation of oxide fingerprint spectra starts with the two oxides most favorable as protective scale, namely chromia and alpha alumina (Cr_2O_3, α-Al_2O_3). Both oxides have a Rhombohedral structure referred to as corundum [50]. The spectra in Figure 11 are from pure chromia powder and an alumina single crystal substrate. All the samples used for standards were at least 99% pure. The spectra are offset and rescaled for clarity. The peak positions and relative peak intensities are dramatically

different, thus identifying these two phases in a scale should be straight forward. By comparing the spectra from the Cr_2O_3 powder to the spectrum of oxidized stainless steel in Figure 10 we see the scale is composed mostly of chromia.

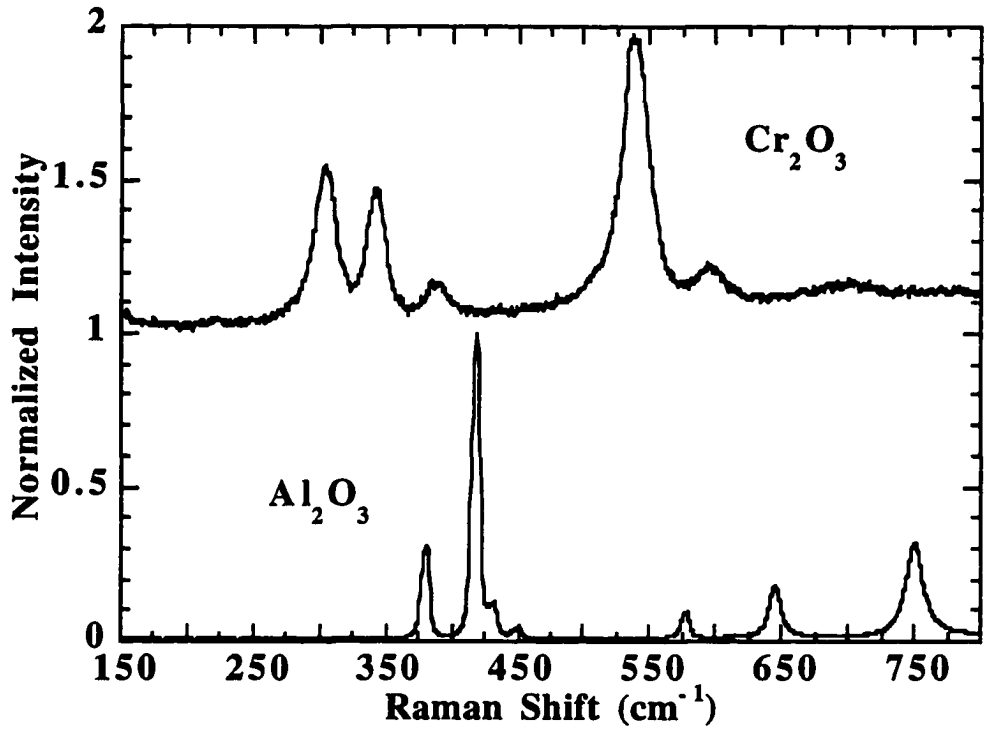

Figure 11. Raman Spectra From Polycrystalline Cr_2O_3 and Single Crystal α-Al_2O_3.

A large number of alloys contain abundant iron. Figure 12 are spectra from reagent grade powders of two of the chemical phases of iron oxide, magnetite (Fe_3O_4) and hematite (Fe_2O_3), which have spinel (cubic) and corundum structures respectively [50, 51]. Note that the spectrum in Figure 12 corresponding to Fe_3O_4 has weak lines at the Fe_2O_3 positions; this is a clear indication that our sample was not single phase magnetite but contained some hematite contamination. Again the uniqueness of the peak position and relative peak intensities ought to allow us to distinguish these phases in a scale.

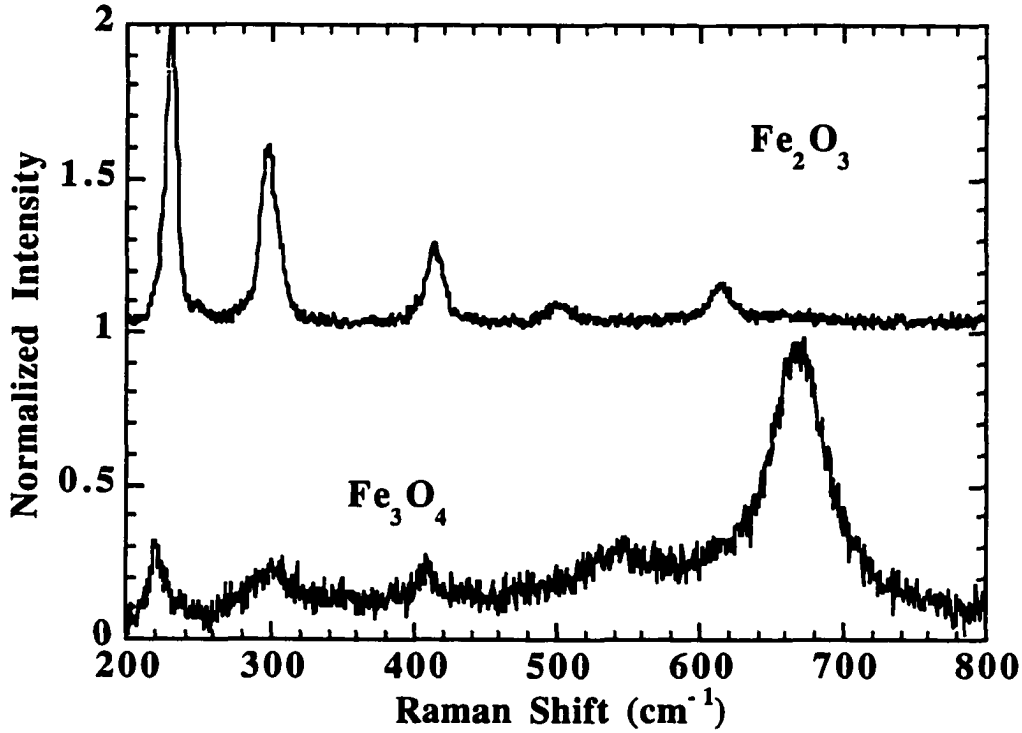

Figure 12. Raman Spectra From Polycrystalline Fe_2O_3 and Fe_3O_4.

Pure samples of FeO were not obtained, so spectra are not provided. However FeO has been reported to have one Raman peak at ~663 cm^{-1} [23, 52]. However, care has to be taken because in the literature Fe_3O_4 and FeO have been assigned peak position at similar energy. This coincidence may be due to an FeO sample being partly oxidized into Fe_3O_4. FeO and NiO are reported to be NaCl structure [53], which has no first order Raman active modes. However in the case of NiO this shortcoming has been circumvented by utilizing second order Raman. The spectra in Figure 13 is from a 25 μm thick, high quality (green), single crystal NiO film. The peak at ~1100 cm^{-1} and at ~1550 cm^{-1} are due to second-order Raman and two magnon scattering respectively [54]. The NiO spectrum makes for an excellent fingerprint because its features have dramatically different Raman shifts.

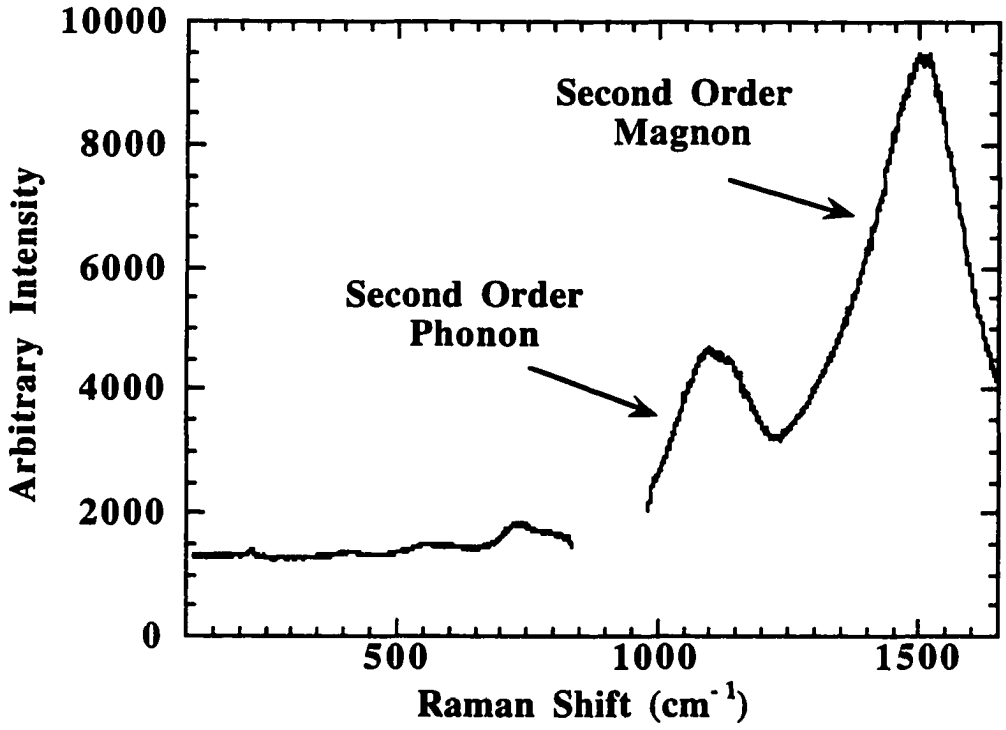

Figure 13. First and Second Order Raman Spectra From a 25 μm Thick Single Crystal NiO Film.

The fingerprint spectra, from stoichiometric oxides, presented thus far will make it possible to study corrosion. However, complications will arise due to the effects that defects and vacancies have on Raman spectra. Additional complications will arise due to some oxides having more than one crystal structure for a given stoichiometry. A third source for complication is with oxides that have more than one type of metallic element, such as AB_2O_4 and ABO_3, where A and B are different metal ions. Additional fingerprint spectra have been obtained and are catalogued in Appendix A. We will use the fingerprint spectra that we have accumulated to study corrosion and we will address the above complications as they arise.

Corrosion of Elemental Metals

As an initial test we investigated the oxidation of pure Fe, Co, Ni and Cr which are major constituents of most steels. These were in the form of: (a) bulk polycrystalline Fe and Ni, (b) a Cr single crystal and (c) a thin film (~1 micron thick) of Co sputtered onto a sapphire substrate. Due to the low melting point of aluminum (660°C [55]), high temperature corrosion studies are not possible on metallic Al. However the polymorphs of Al_2O_3 were investigated using powder samples of alumina. The first purpose of these initial tests is to explore the fingerprinting technique without the complications due to the aforementioned oxides of the form AB_2O_4 and ABO_3. The second purpose is to develop an understanding of the corrosion of the elements that compose more complicated steel alloys.

The polycrystalline samples were small plates (1 cm^2 or less) cut from rolled sheets (~1 mm thick) of each metal. The surfaces were finished with 1 μm diamond polishing grit. All of our spectra were acquired in only 500 sec. We have performed all our measurements at room temperature after annealing the samples at specified temperatures and times. All heat treatments were done in air for one hour duration at the desired temperature. Higher temperature anneals were performed on the same sample that was previously subjected to lower temperature anneals; i.e. oxide scale growth was cumulative with increasing temperature. Thus the scales observed at higher temperatures also reflect the "pretreatment" oxidation resulting from thermally cycling to sequentially higher temperatures. At the highest temperatures (~1000°C) the scale growth is rapid, and thermal history probably becomes relatively unimportant. The above treatment of the metallic samples was reproduced when we investigated the commercial available alloys, discussed in the next section.

Figure 14 shows the temperature dependence of Raman spectra observed on thermally treated pure (bulk) Fe. By comparing Figure 14 to Figure 12, we see that at low temperatures (~ 300°C) the dominant observable species in the oxide is magnetite (Fe_3O_4) which is slowly replaced by hematite (Fe_2O_3) as the temperature is raised. Above 800°C, the Fe_3O_4 is no longer visible in the spectrum. Aside from the magnetite and hematite, no other features are observed even to the highest temperatures reached (~1000°C) and no evidence of spalling was visually observed. The fingerprinting technique appears to work nicely for iron oxide scale. However because our sensitivity to FeO is not known, we are not willing to exclude it presence in the scale. The NaCl structure of FeO is normally first order Raman inactive, but FeO is known to have several defect structures [56] which may be able to produce disorder induced Raman modes. Sorting out the details of the Raman spectra of defective FeO is a subject for further study.

Figure 15 shows the temperature dependence of the Raman spectra observed from the oxidation of a Co film. By comparing the spectra in Figure 15 to the standards in Appendix A, we see that Co_3O_4 forms at 300°C and persists to 600°C. Above 600°C the Co film and scale catastrophically debonded from the sapphire substrates. Once again the fingerprinting technique works nicely for the corrosion of Co. Cobalt is known to form CoO which like FeO has a NaCl structure [53] and may only be first order Raman active if a sufficient number of defects are present. Defected cobalt oxide was not studied, and the presence of CoO in the scale can not be excluded on the bases of these Raman experiments.

The spectra in Figure 16 show the temperature dependence of the Raman spectra observed from the scale formed on the Ni sample. By referring to Figure 13 we see that the peaks at ~1100 cm^{-1} and at ~1550 cm^{-1} are due to second-order phonon and magnon scattering respectively. As mentioned earlier, stoichiometric compounds that

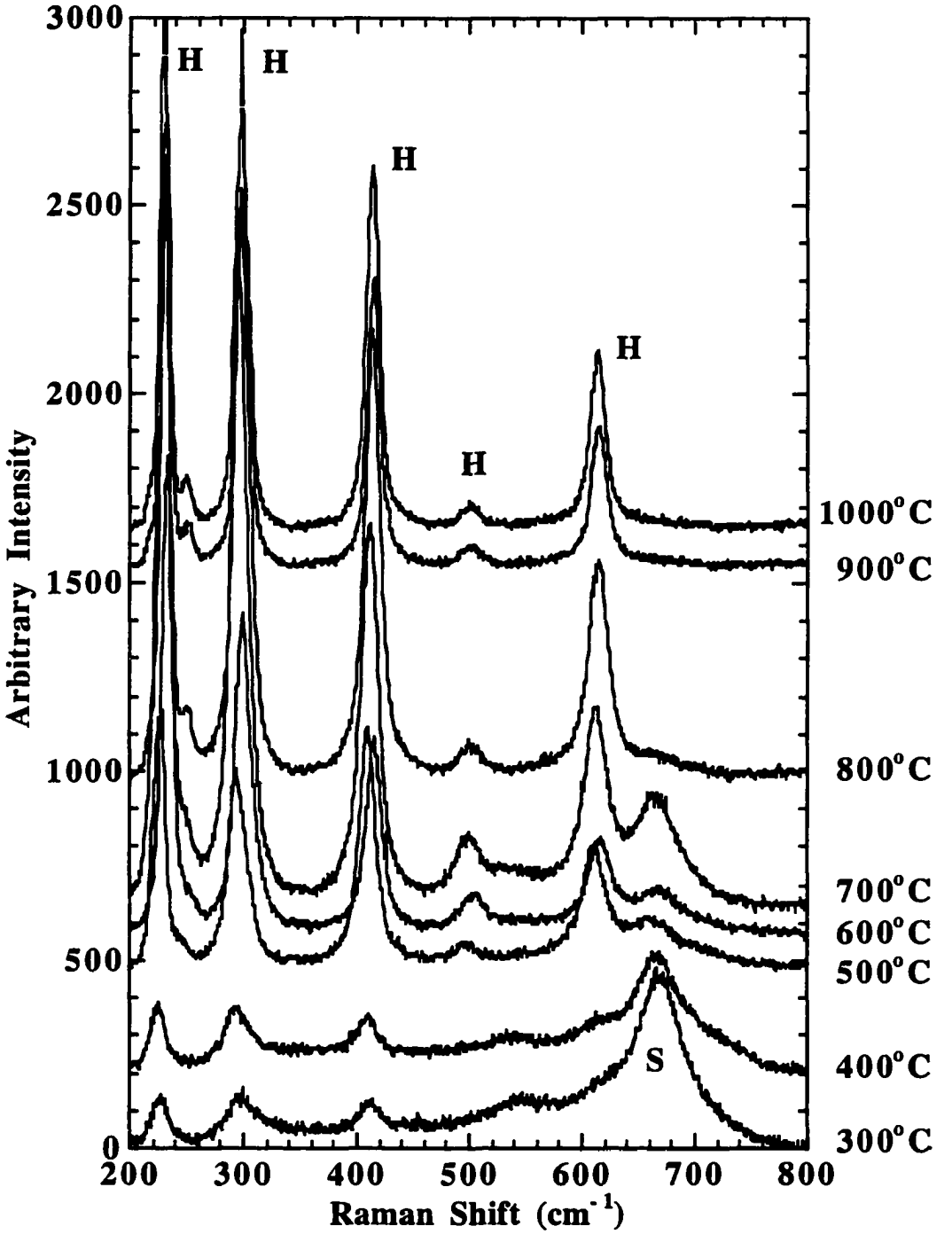

Figure 14. Raman Spectra From Oxidized Iron. Sequential oxidation in air for 1 hr at each of the indicated temperatures. The H and S indicates Fe_2O_3 and Fe_3O_4 respectively.

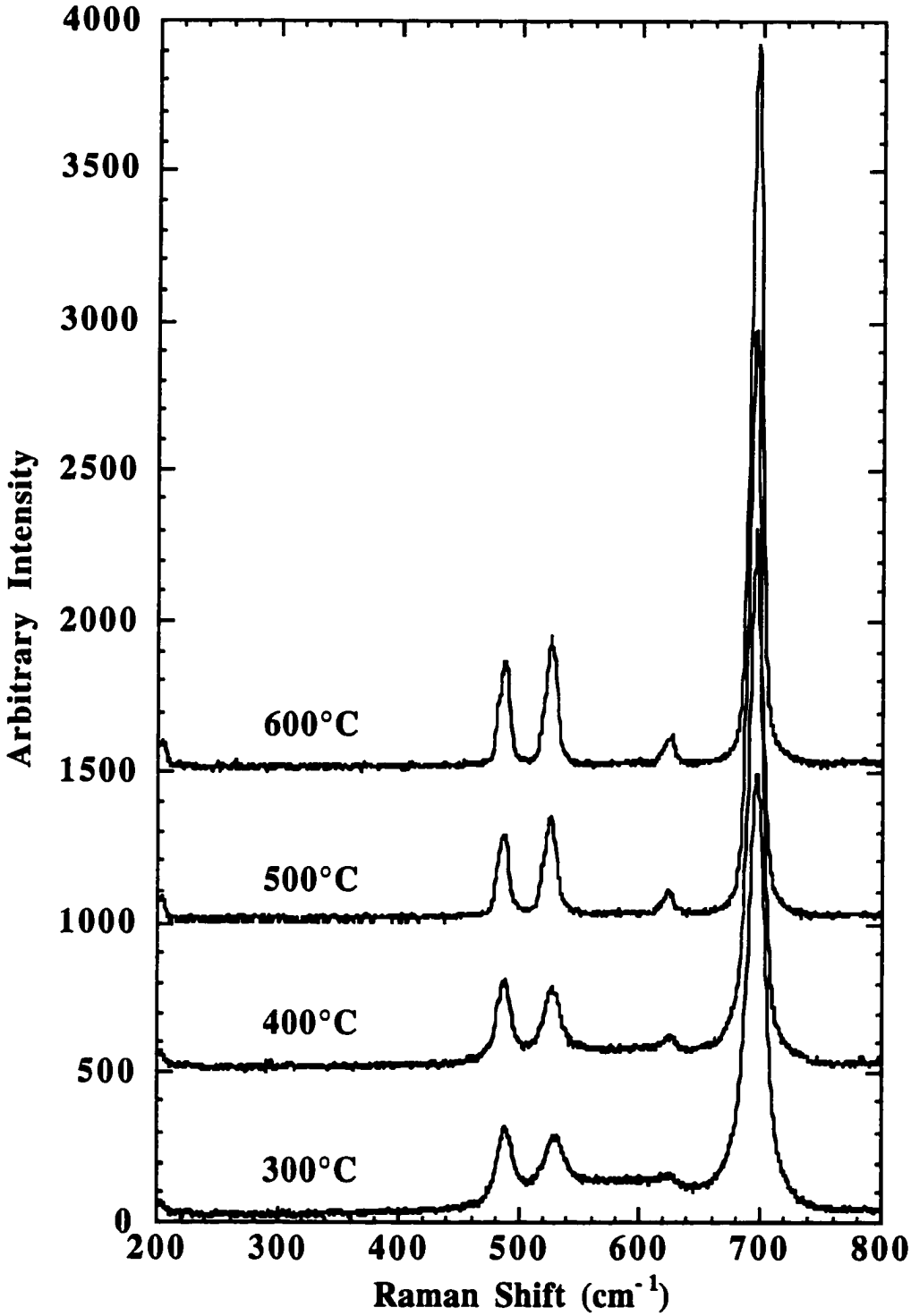

Figure 15. Raman Spectra From an Oxidized Cobalt Film. Sequential oxidation in air for 1 hr at each of the indicated temperatures.

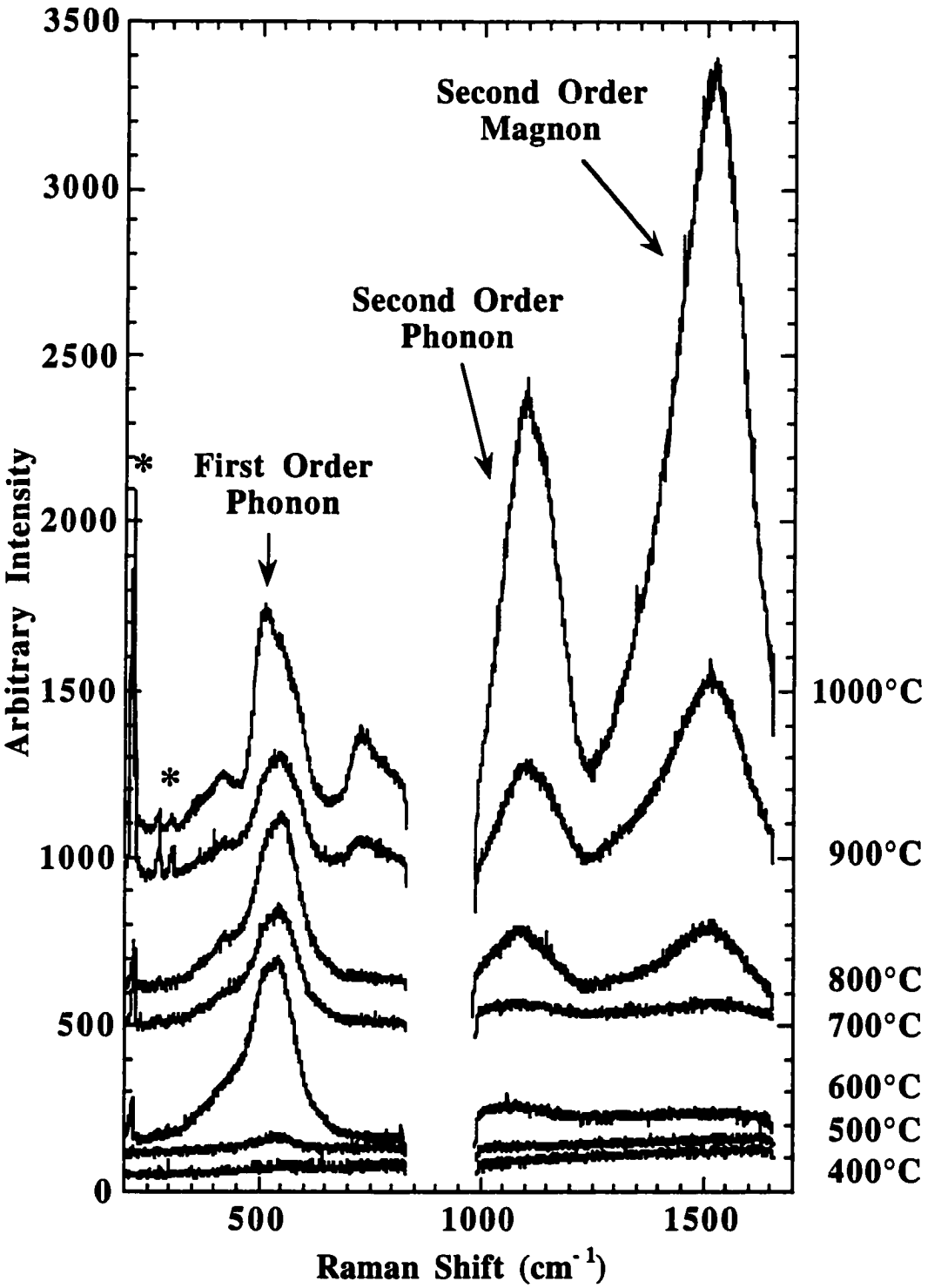

Figure 16. First and Second Order Raman Spectra From Oxidized Nickel. Sequential oxidation in air for 1 hr at each of the indicated temperatures. The * indicates plasma lines from the Kr laser.

have the sodium chloride structure, like NiO, have no allowed first order Raman scattering, but vacancies and impurities can break the local symmetry, allowing disorder induced Raman scattering to be observed. There are compelling arguments that the peak seen at ~550 cm^{-1} in the Ni-oxide scale is due to disorder induced scattering from phonons that are normally Raman inactive. The NaCl structure has one infrared active mode. For NiO it has been measured and found to be at ~550 cm^{-1} [57]. This means that there exist vibrational states at the proper energy to produce a Raman peak if the structure of the material is sufficiently disordered to break the Raman selection rules. A second argument is that the first order peak is at about half the energy of the second order phonon peak, at ~1100 cm^{-1}.

After 1 hour at 500°C a measurable amount of NiO forms on the surface. As expected for NiO, no phase change is observed at higher temperatures. Interesting is the temperature dependence of the peak intensities. For heat treatments between 600°C and 1000°C the intensity of the disorder induced peak (~550 cm^{-1}) remains relatively constant while the intensity of the allowed second order scattering (~1100 cm^{-1}, ~1550 cm^{-1}) increases dramatically. This is consistent with the disorder decreasing at higher temperatures, while the total scale thickness increases.

The disorder-induced Raman spectra for NiO has been reported to be at ~550 cm^{-1} [31, 58], and has been attributed to oxygen richness. However, the oxygen stoichiometries of the samples in the literature were not measured. The oxygen richness was determined by the color (black) of the samples. In principle Ni-richness can also produce disorder-induced Raman modes. The oxygen stoichiometry of our samples was not measured, but we would like to argue that the scale could be Ni rich, based on the behavior of the Fe-oxide scale in Figure 14. At low temperatures the Fe_3O_4 scale has a higher Fe content than the Fe_2O_3 scale observed at high temperatures. The effect that vacancies have on the Raman spectra from NiO requires further study.

The above finding is relevant to other oxides that share the NaCl structure, such as the already mentioned FeO and CoO. Even though an oxide has no first order Raman active modes, it may still be fingerprintable by means of second order Raman, second order magnon and disorder induced Raman.

For Cr (Figure 17), after the one hour oxidation below 500°C, we observe a broad peak near ~670 cm^{-1}. At 600°C and 700°C we observe the appearance of a number of sharp features; again comparing to Figure 11, we see that all except one of these features (~670 cm^{-1} labeled S/D in the figure) are consistent with Cr_2O_3. Finally, above 700°C the scale becomes a stable Cr_2O_3 . No additional features are observed in the spectra even at the highest temperatures and no visual spalling is observed in the samples.

Raman fingerprinting clearly identifies the stoichiometric compound Cr_2O_3. Features like the additional sharp peak labeled S/D have been observed in ternary chromia forming alloys, where it has been attributed to mixed spinels [20-23, 26-29, 31] like $FeCr_2O_4$ and $NiCr_2O_4$ [20-23, 26, 27, 29, 30]. There are a number of spinels that produce a peak in the neighborhood of ~670 cm^{-1}, so a spinel like Cr_30_4, if it exists, might also show a similar feature. Powder samples of Cr_3O_4 are not available for fingerprinting. However there is evidence from RHEED and SIM/Auger experiments [30, 59] which show that at low oxidation temperatures two other Cr-oxide phases form on Cr metal; one of these phases is thought to be Cr_3O_4 with a spinel structure. However a careful examination of the literature has unearthed a second possible source of the S/D peak in the Cr-oxide. Iron doped Cr_2O_3 can generate a disorder-induced Raman band in the neighborhood of ~670 cm^{-1} [60, 61]. Since the Cr-oxide scale that forms on Cr-metal at low temperature may possess either chromium or oxygen vacancies, they could also cause a disorder-induced Raman peak at ~670 cm^{-1}, similar to the effect observed during the corrosion of Ni.

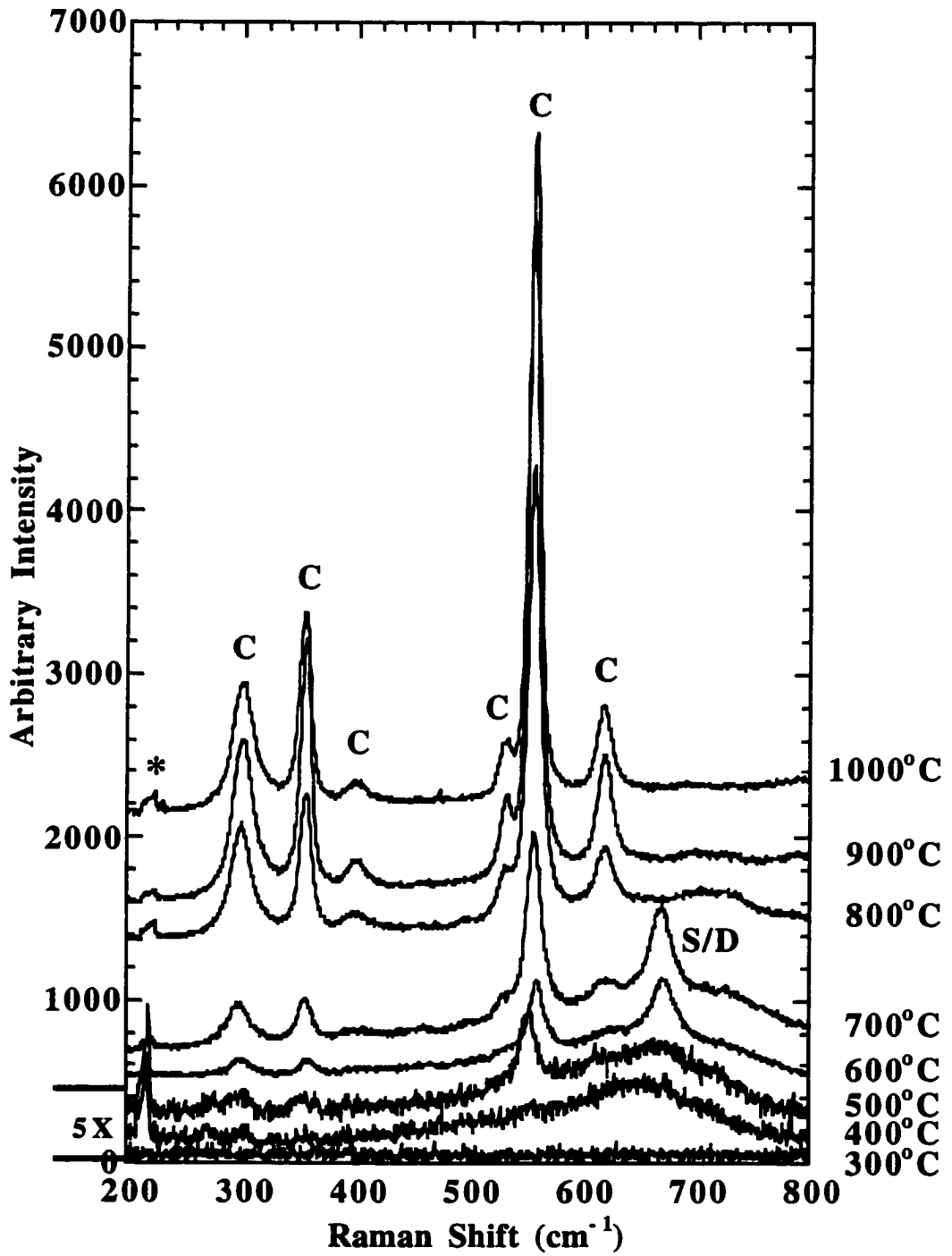

Figure 17. Raman Spectra From Oxidized Chromium. Sequential oxidation in air for 1 hr at each of the indicated temperatures. The C indicates Raman peaks from Cr_2O_3. The S/D indicates Raman peaks from either an unidentified spinal or disorder induced Raman scattering. The * indicates plasma lines from the Kr laser.

The broad feature seen at ~670 cm^{-1} in Figure 17 at temperature below 500°C, will be seen again when we investigate the corrosion of Fe-Ni-Cr alloys. It is possible that at low temperatures a very disordered, or perhaps amorphous, spinel or corundum structured Cr-oxide is formed which then evolves into an ordered structure at around 550°C, thus causing the broad peak at ~670 cm^{-1} to sharpen into the band labeled S/D. More work is needed to resolve these issues but it is clear that Raman scattering can be a convenient tool to aid in such an investigation.

Scales composed of α-Al_2O_3 are considered to be of exceptional quality, because they are slow growing and highly stable. The main weakness of the α-Al_2O_3 scale is its high susceptibility to cracking and spalling [62]. Because pure α-Al_2O_3 forms at temperatures greater than ~1000°C, studying its formation on Al is not possible, because aluminum melts at 660°C [55]. Al_2O_3 is considered to be highly stoichiometric, however at temperatures below ~1000°C it is known to exist in various other metastable crystalline structures. Because there are many reports of metastable alumina forming on high temperature alloys [62, 63, 64], it is prudent to perform Raman studies on some of the other non-α crystalline phases of Al_2O_3. Some of the results from Raman spectroscopy are presented in this section of the dissertation, but a more detailed discussion has been reserved for Appendix B.

In an effort to understand how the α-phase is generated in scales, we have investigated the temperature induced γ to α transition. This transition is reported to occur via an intermediate phase (κ or θ [65-69]). In order to facilitate our Raman study reagent grade γ-Al_2O_3 was obtained from a chemical supply company. A sample of the as received powder was pressed at ~5000 psi of pressure, into a pellet ~1 cm diameter and ~0.5 cm tall. The pellet was sequentially heat treated from 600°C to 1200°C in steps of either 50°C or 100°C, for one hour at each temperature. Raman scattering, ruby fluorescence and X-ray powder diffraction (XRD) measurements were performed

at room temperature between each treatment. The Raman spectra are presented in Figure 18. The remainder of the data is in Appendix B.

At temperatures below 800°C the X-ray data confirm that the sample is γ-Al_2O_3, however the Raman spectra are almost featureless, save a broad fluorescence background and a weak peak at ~520 cm^{-1}. For temperatures between 900°C and 1150°C the Raman spectra contain peaks that are clearly not attributable to α-Al_2O_3, so they must originate from an intermediate transient phase. The positions of the non-α peaks are ~255 cm^{-1}, ~335 cm^{-1}, ~620 cm^{-1}, ~710 cm^{-1}, ~780 cm^{-1}. This transient phase has been identified as κ-Al_2O_3 by XRD. The Raman spectrum taken after the 1200°C anneal is identical to the fingerprint spectrum from the single crystal α-Al_2O_3 in Figure 11.

We have used Raman fingerprint technique in conjunction with XRD to track the crystal phase evolution of the γ to α alumina transition, and in the process pick up two new Raman fingerprints. The fingerprint for γ-alumina is of poor quality. Since the 520 cm^{-1} line is very weak even in the bulk sample, it is doubtful that it can be observed in a thin scale. On the other hand the 255 cm^{-1} peak from κ-Al_2O_3 will turn out to be significant when investigating scales.

The initial test of the fingerprinting technique provides some interesting results. The phase of a mature scales (i.e. higher temperature scales) are easily identifiable. This work also show that scales are not usually composed of perfectly stoichiometric reagent grade oxides. We have also shown that early stage oxidation, transient phase behavior, and defect structures are also detectable using the Raman scattering technique.

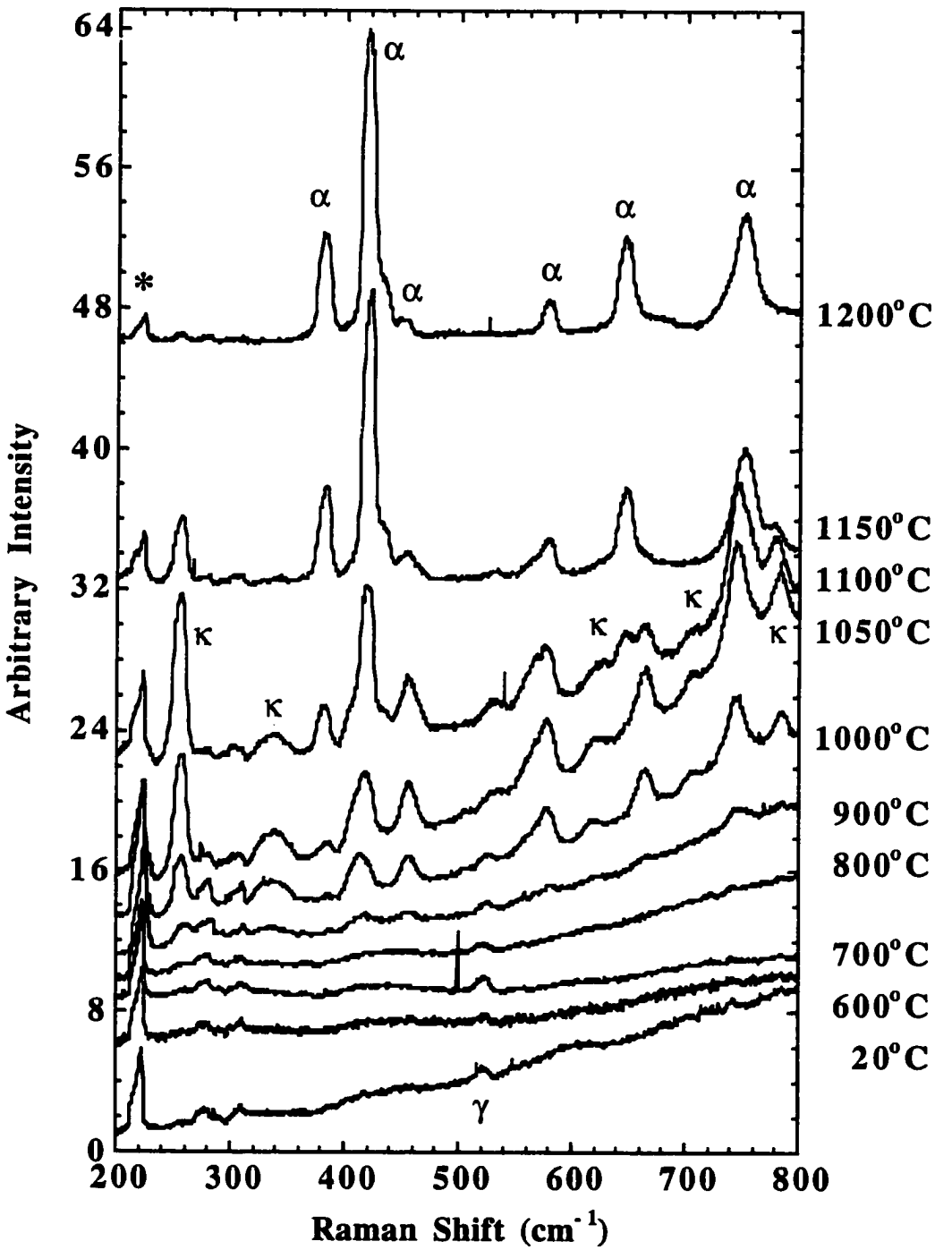

Figure 18. Raman Spectra From Heat Treated Alumina. Sequentially heat treated in air for 1 hr at each of the indicated temperatures. The α, κ and γ indicates Raman peaks from α-, κ- and γ-Al_2O_3 respectively The * indicates plasma lines from the Kr laser.

Commercially Available Alloys

The samples investigated here are alloys with compositions based on commercially available stainless steels. Off the shelf alloys often contain small amounts of elements, such as carbon, silicon, and boron, that adjust their mechanical properties. Most of our samples do not contain these additives. Commercially available alloys also often contain, in small quantities, what are commonly referred to as reactive elements (e.g. Zr, Y, and Hf) that improve corrosion resistance. Surprisingly, even though the inclusion of these reactive elements is done routinely, the mechanism by which the reactive elements improves corrosion resistance is still not known. Since there are many theories proposed to explain the reactive elements effect we have prepared samples with and without reactive elements for comparative purposes. In the following investigation of alloys we should anticipate complications due to oxides of the form AB_2O_4 and ABO_3, where the fingerprinted of many are cataloged in Appendix A.

The remainder of the alloy samples in this chapter received similar surface finishes and similar sequential thermal histories as the elemental samples of the previous section. Again the Raman data was acquired in air with the same 500 sec data acquisition time.

Oxidation of Fe-Cr-Ni Alloys

Raman spectra from oxide scales thermally grown on Fe-Cr-Ni samples are presented in Figures 19-21: Fe-25Cr-20Ni, with and without the reactive element Zr, and the Ni free alloy Fe-24Cr-3Zr. All concentrations are given in wt. % and the balance is

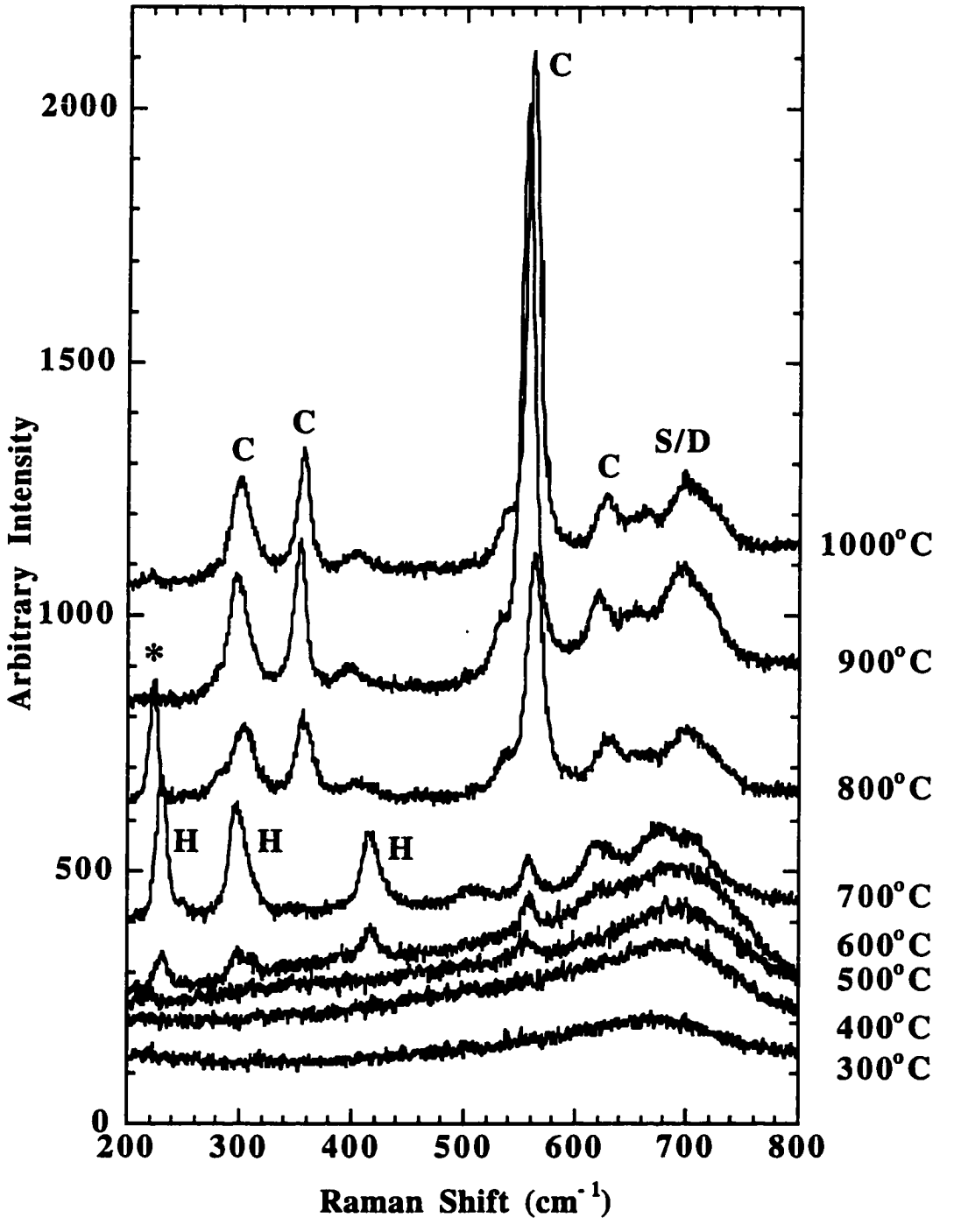

Figure 19. Raman Spectra From Oxidized Fe25Cr20Ni. Sequential oxidation in air for 1 hr at each of the indicated temperatures. The C and H indicate Raman peaks from Cr_2O_3 and Fe_2O_3 respectively. The S/D indicates Raman peaks from either an unidentified spinal or disorder induced Raman scattering. The * indicates plasma lines from the Kr laser.

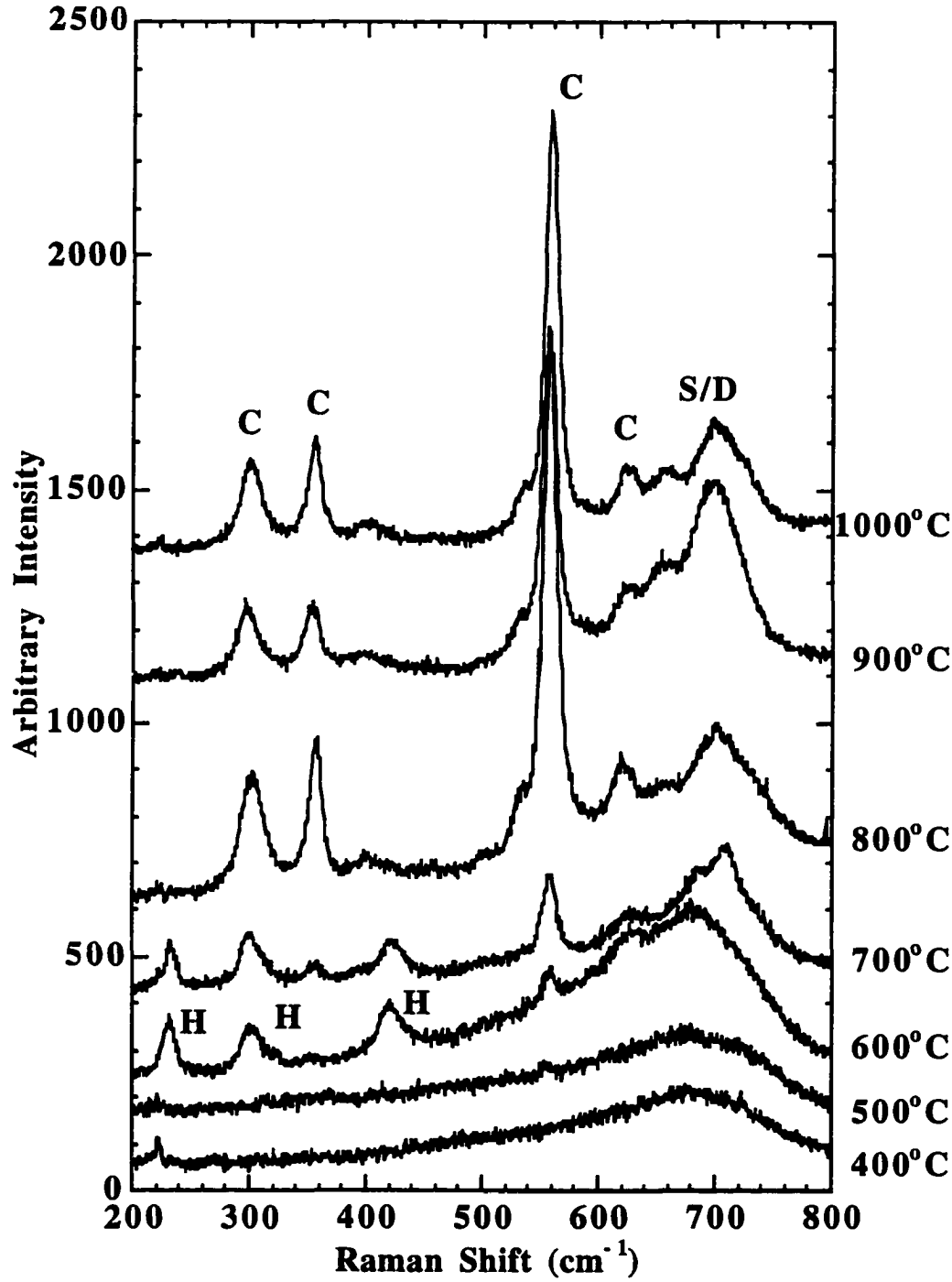

Figure 20. Raman Spectra From Oxidized Fe25Cr20Ni-3Zr. Sequential oxidation in air for 1 hr at each of the indicated temperatures. The C and H indicate Raman peaks from Cr_2O_3 and Fe_2O_3 respectively. The S/D indicates Raman peaks from either an unidentified spinal or disorder induced Raman scattering. The * indicates plasma lines from the Kr laser.

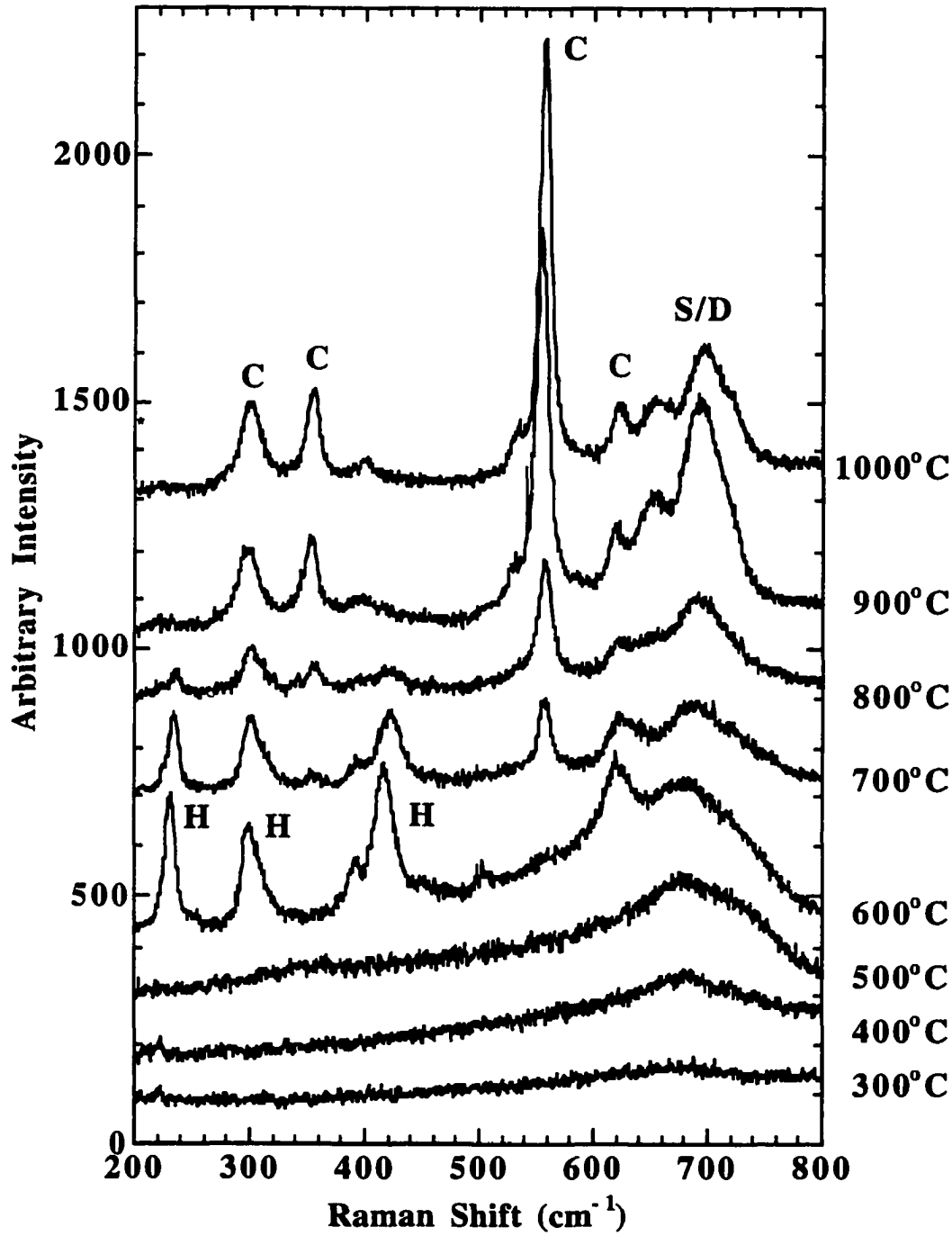

Figure 21. Raman Spectra From Oxidized Fe25Cr-3Zr. Sequential oxidation in air for 1 hr at each of the indicated temperatures. The C and H indicate Raman peaks from Cr_2O_3 and Fe_2O_3 respectively. The S/D indicates Raman peaks from either an unidentified spinal or a disorder induced Raman scattering. The * indicates plasma lines from the Kr laser.

iron. These alloys are iron based and are known to form chromia scales at high temperatures.

The lowest temperature at which we observe a Raman signal is 300°C. This broad, rather featureless spectrum is essentially identical in all three samples and dominates at temperatures below about 500°C. This broad feature shows a strong similarity to the low temperature spectrum in Figure 17 obtained from pure Cr treated at 400°C. For treatments up to 500°C, in all three alloys, the intensity of the broad feature systematically increases; no other significant changes are detected. We have found, however, that the spectral features observed at these low temperatures do depend on the thermal history experienced by the sample. We will return to this point later.

Above 500°C, Fe_2O_3 peaks appear, they are labeled H (hematite) in the figures. As the oxidation temperature is increased to ~700°C, these peaks dominate the spectrum. The chromia peaks become visible near 700°C and become the dominant species above 800°C where the Fe_2O_3 peaks disappear. At ~ 700°C and above, the broad feature (~670 cm^{-1}) observed at low temperatures develops into several broad peaks, starting at ~650 cm^{-1} and ending at ~700 cm^{-1} (labeled S/D in the figure). By comparing the spectra in Figure 12 for the spinel Fe_3O_4 and spectra in Appendix A for the spinel structured oxides $NiFe_2O_4$ and $NiCr_2O_4$ we see there are several AB_2O_4 oxides that have there strongest peaks in this region. In reference 60, MaCarty etal. report that the stoichiometric compound $FeCr_2O_4$ (spinel) has one strong peak at ~686 cm^{-1}. MaCarty also reports that the solid solutions $Fe_{3-x}Cr_xO_4$ ($0.04<x<1.6$) and $Fe_{2-x}Cr_xO_3$ ($0.27<x<1.60$) have strong Raman peaks between 664 cm^{-1} and 686 cm^{-1}. We conclude that the features in the spectra from the scale, labeled S/D in Figures 19-21, are due to some mixture of AB_2O_4 and ABO_3 (where A = Ni, Fe, Cr and B = Fe, Cr) the exact composition cannot be identified by Raman fingerprinting. A similar

conclusion was reached by Graves et al. for the compounds Fe_3O_4, $NiFe_2O_4$ and $MnFe_2O_4$.[70] It seems clear that the additional peaks we see at high temperature are due to a mixed oxide of some form. It is possible that at low temperatures (below 500°C) a disordered perhaps amorphous structure is formed which then evolves into an ordered structure at around 550°C, causing the spectra to develop sharper peaks.

Above 1000°C spallation occurs and large variations occur in the Raman spectra acquired from different points on the sample surface. In these samples the evolution of the scales (as observed with Raman scattering) shows no systematic variations due to the presence of either Ni or Zr. Investigation by second order Raman scattering shows no evidence of any NiO in the scale.

We now examine some transient oxidation effects associated with different thermal histories about which very little is presently known. Figure 22 shows Raman spectra from Fe-25Cr-20Ni samples, each annealed for one hour at the indicated temperatures, but with no prior heat treatment at lower temperatures. These results differ from the corresponding spectra in Figure 19 for heat treatments at 400°C, 500°C and 600°C. The samples with no pretreatment (Figure 22) show a clear signal attributable to Fe_2O_3, while those that had been pretreated (beginning at 300°C; Figure 19) remain dominated by the broad Raman spectrum which we have not clearly identified. At T > 600°C, the effect of pretreatment diminishes. The transient Fe_2O_3 signal becomes prominent in both cases. With 1000°C treatments, the observed spectra, predominately Cr_2O_3, are essentially identical for both thermal histories.

Apparently, with pretreatment at ~300°C, the alloy develops an (unidentified) oxide scale which then acts to inhibit formation of the transient Fe_2O_3 phase (and the subsequent steady state Cr_2O_3 phase). It may be that, for operating temperatures below ~600°C, low temperature (~300°C) pretreatments will produce a

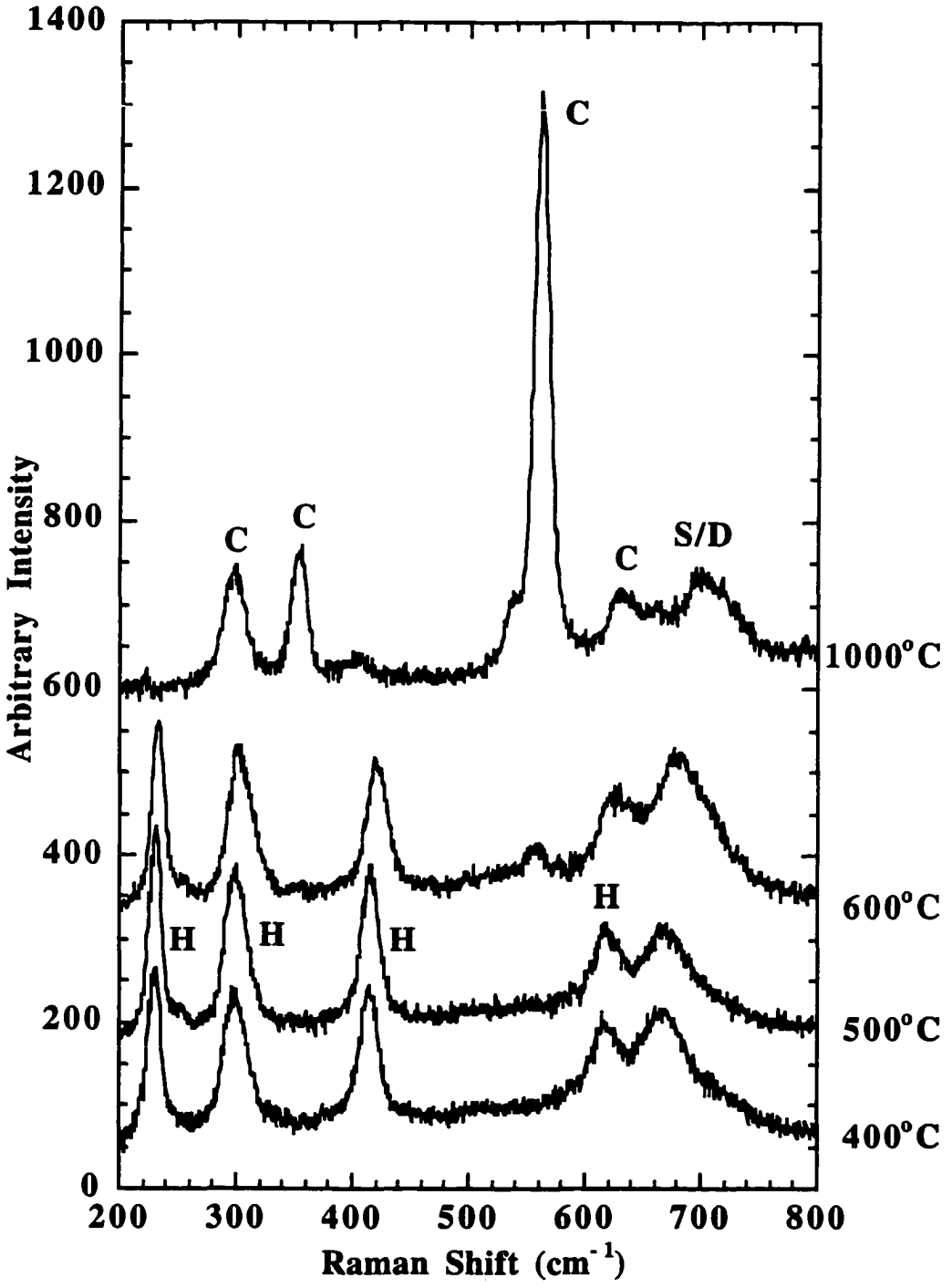

Figure 22. Oxidation of Bulk Fe25Cr20Ni, With No Thermal History. Oxidation in air for 1 hr at each of the indicated temperatures. The C and H indicate Raman peaks from Cr_2O_3 and Fe_2O_3 respectively. The S/D indicates Raman peaks from either an unidentified spinal or disorder induced Raman scattering. The * indicates plasma lines from the Kr laser.

scale that slows further scale growth and the evolution through subsequent transient phases. This thin pretreatment scale might provide some corrosion protection when the alloys are used in the temperature range of 500°C - 600°C.

To summarize this section. The fingerprint technique was successfully used to identify some of the transient and steady state oxide phases, during scale growth. The technique works especially well for Fe_2O_3 and Cr_2O_3. The presence of mixed oxides AB_2O_4 (A may equal B) and ABO_3 (A may not equal B), where A = Ni, Fe, Cr and B = Fe, Cr was detected. However peak overlap makes the exact composition of AB_2O_4 and ABO_3 impossible. At low temperatures, an unidentified phase was found to be dependent on thermal history. The presence of Ni and Zr in the alloy did not show any systematic variations in the scale evolution.

Oxidation of Fe-Cr-Al Alloys

Oxidation studies were also carried out on a series of alloys which are known to produce mature alumina scales. We chose Fe-5Cr-28Al (FA71), Fe-5Cr-28Al-0.1Zr-0.05B (FAL), Fe-18Cr-10Al (LBL) and Fe-18Cr-10Al-0.5Hf (LBL-Hf), all compositions are in at% and the balance is Fe. Zr and Hf are the reactive elements in the alloys. Because the compositions of the above alloys are quite similar, our Raman data will show that the scale phase evolution is also similar. However, in the next chapter we will show that the scale stress and ruby fluorescence signal strengths are dramatically different for each of the above alloys.

Figures 23 and 24 show Raman spectra from the LBL and LBL-Hf samples respectively. In both cases, the Fe_2O_3 signal appears after oxidation at 500°C. There may also be a weak Cr_2O_3 signal also visible as a transient oxide; it is observable in the Raman spectra between 600°C - 800°C. Also observed is the S/D peak which is similar

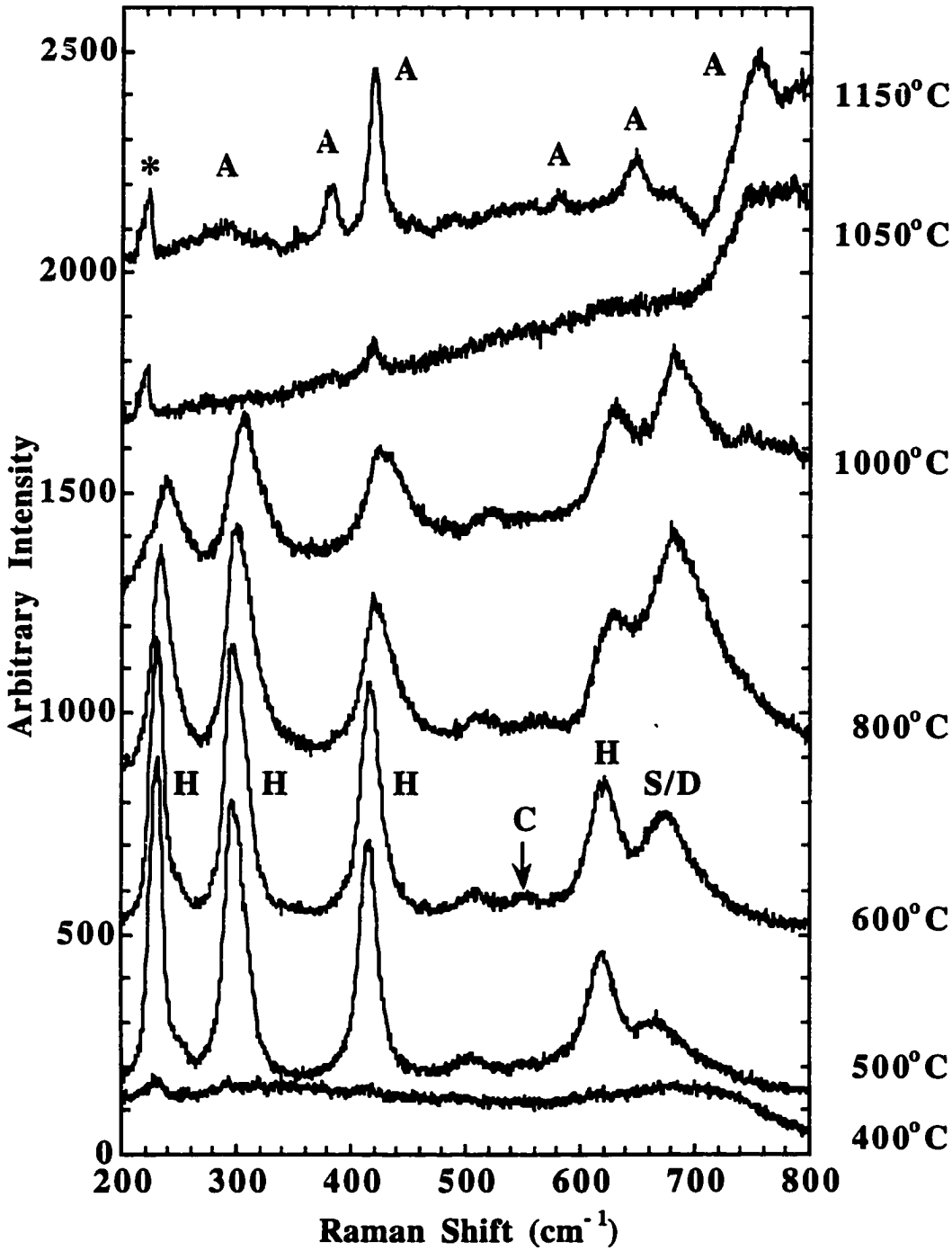

Figure 23. Raman Spectra From Oxidized LBL. Sequential oxidation in air for 1 hr at each of the indicated temperatures. The A and H indicate Raman peaks from α-Al_2O_3 and Fe_2O_3 respectively. The S/D indicates Raman peaks from either an unidentified spinal or disorder induced Raman scattering. The * indicates plasma lines from the Kr laser.

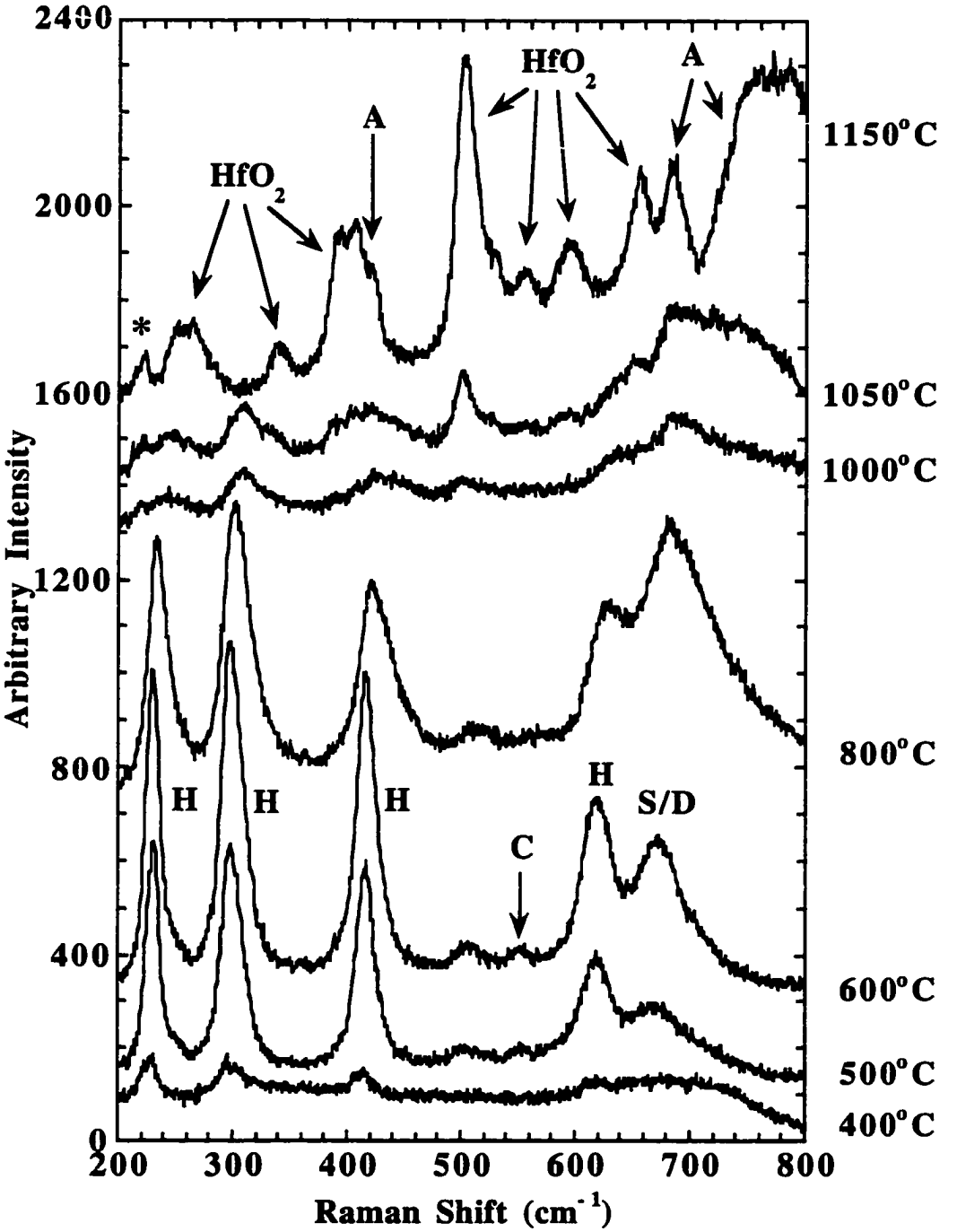

Figure 24. Raman Spectra From Oxidized LBL-Hf. Sequential oxidation in air for 1 hr at each of the indicated temperatures. The A and H indicate Raman peaks from α-Al_2O_3 and Fe_2O_3 respectively. The S/D indicates Raman peaks from either an unidentified spinal or disorder induced Raman scattering. The * indicates plasma lines from the Kr laser.

to the one seen in the spectra taken from the scales that formed on the Fe-Cr-Ni alloys. We attribute the S/D feature to a comparable mixed phase spinel or disordered corundum oxides, as we did before. When these alloys were oxidized at temperatures higher than 1000°C, both the Fe_2O_3, Cr_2O_3 and S/D Raman signals disappeared.

For LBL the Raman signal from α-Al_2O_3 (labeled A in the figure) dominates above ~1050°C. Because the Raman scattering from α-Al_2O_3 is weaker than that from Fe_2O_3 and Cr_2O_3, the alumina signal is not visible until the scale contains a relatively large volume fraction of the α-phase. This explains the spectra in the range 1050°C which show only weak features.

For oxidation above ~1000°C, the Hf-containing sample (Figure 24) shows many additional peaks relative to the Hf-free sample. These new peaks, which dominate the spectrum after high temperature oxidation, can be identified as due to HfO_2 (see Appendix A for fingerprint spectra). Since HfO_2 has a Raman cross section which is much larger than that of α-Al_2O_3, one should not infer that the scale is predominately HfO_2. Indeed, SEM (Energy Dispersive X-ray Analysis) measurements on a similar sample indicate that the scale has the (atomic) composition of 4% Hf, 21% Al at 1150°C. In both samples the high energy α-Al_2O_3 bands (at ~650 cm^{-1} and ~750 cm^{-1}) appear to be broader than the corresponding peak seen in single crystal α-Al_2O_3, Figure 11. This may be due to the presence of the spinel $FeAl_2O_4$, in the scale. Unlike the spinels discussed in the previous section, all which have a strong band at ~670cm^{-1}, the strong Raman peaks for $FeAl_2O_4$ are at ~650 cm^{-1} and ~750 cm^{-1} (see Appendix A for fingerprint).

Figures 25 and 26 show the Raman spectra taken from the scales that form on the alloys FA71 and FAL respectively. Like the previous samples we observe that at low temperatures, below ~850°C, the scale is composed of Fe_2O_3 and the unidentified mixed S/D oxides. At temperatures above ~1050°C the Raman signal from

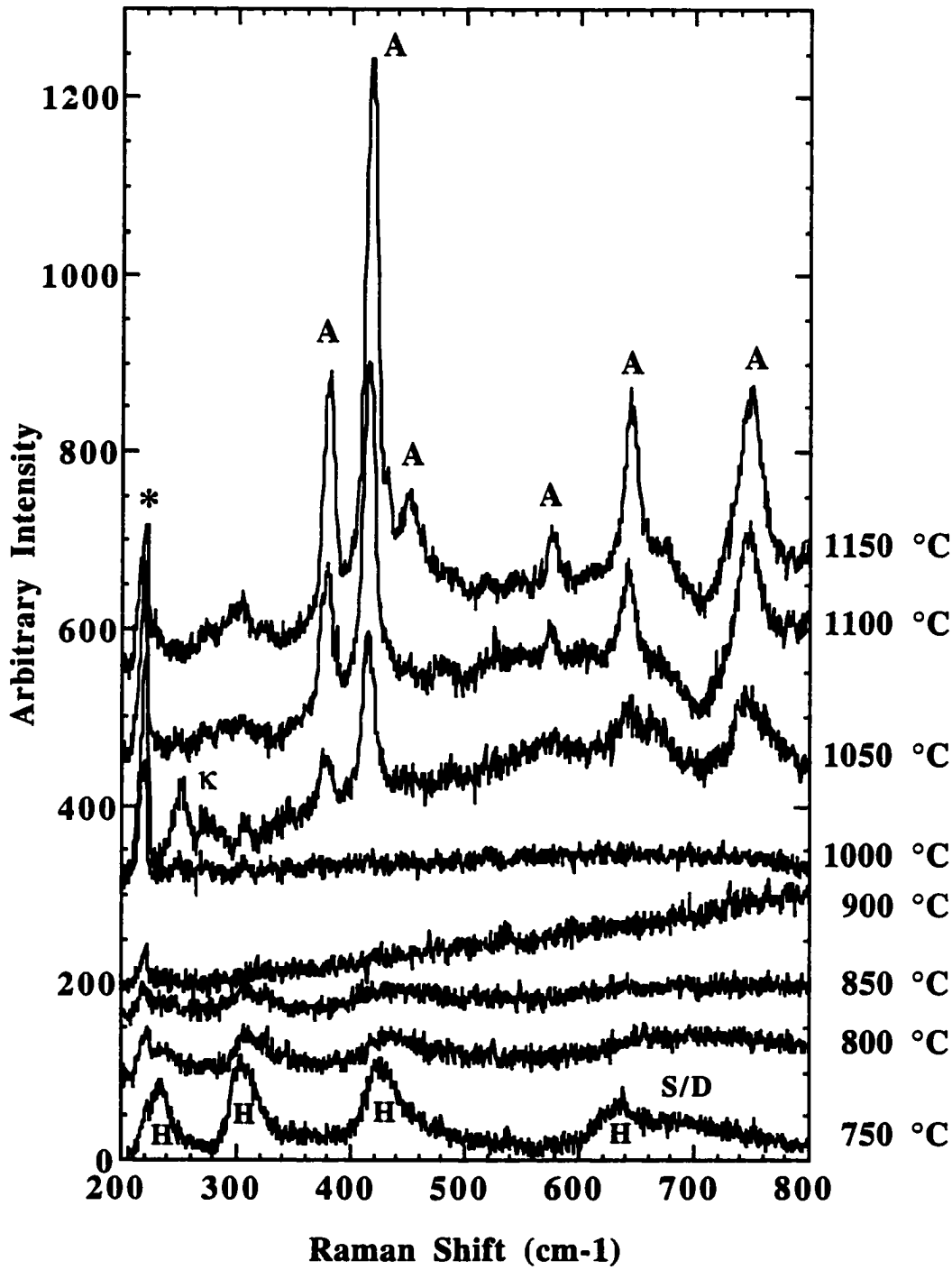

Figure 25. Raman Spectra From Oxidized FA71. Sequential oxidation in air for 1 hr at each of the indicated temperatures. The A and H indicate Raman peaks from α-Al_2O_3 and Fe_2O_3 respectively. The S/D indicates Raman peaks from either an unidentified spinal or disorder induced Raman scattering. The * indicates plasma lines from the Kr laser.

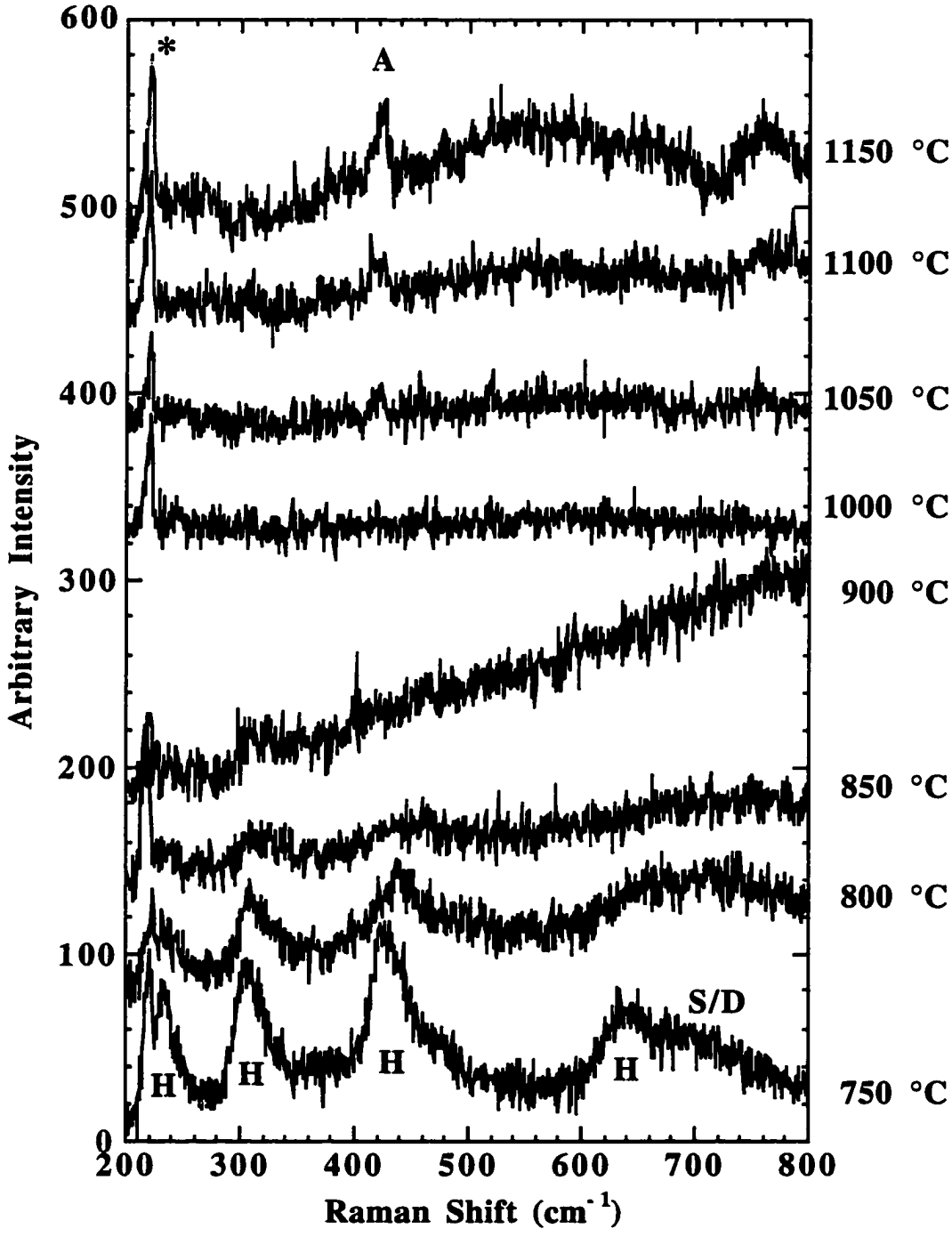

Figure 26. Raman Spectra From Oxidized FAL. Sequential oxidation in air for 1 hr at each of the indicated temperatures. The A and H indicate Raman peaks from α-Al_2O_3 and Fe_2O_3 respectively. The S/D indicates Raman peaks from either an unidentified spinal or disorder induced Raman scattering. The * indicates plasma lines from the Kr laser.

α-Al_2O_3 becomes apparent. However the α-Al_2O_3 Raman signal from the reactive element containing alloy (FAL) is about ten times weaker than the α-Al_2O_3 Raman signal from the Zr-free sample (FA71). Apparently the reactive element is retarding the formation of α-Al_2O_3. As mentioned earlier the Raman signal from γ-alumina is too weak to detect in a scale, but we attribute the Raman band, at 255 cm^{-1}, to κ-Al_2O_3 in the scale on the FA71 sample after the 1050°C heat treatment.

In the next chapter when we investigate the Ruby fluorescence signal strength. We will see dramatically weaker fluorescence signals from reactive element containing alloys. There we attribute this effect to the presence of transient Al_2O_3 in the scale that are stabilized by the reactive element. We will use the above Raman result to support our conclusions. The phase stabilization of metastable Al_2O_3 by the inclusion of La and Ce has been reported in the literature [67, 69]. We have produced similar phase stabilization with Zr in powdered alumina and the results are presented in Appendix B.

Oxidation of M-Cr-Al Alloys

Here we investigate the corrosion behavior of MCrAl(Y) alloys (M=Ni&Co). We chose the MCrAl(Y) alloys for this investigation because of their importance as a bond coat for thermal-barrier-coated systems. The particular compositions, in at% and balance Ni, for the alloys are Ni-23Co-20Cr-13Al and Ni-23Co-20Cr-13Al-0.3Y where Y is the reactive element.

Figures 27 and 28 show the temperature dependence of the Raman spectra observed from the scales formed on MCrAl and MCrAlY, respectively. Below 600°C we observed no Raman signal. At 600°C, we see a broad feature at about 670 cm^{-1}, which is similar to the feature that was observed on the Fe-Cr-Ni alloys and bulk Cr.

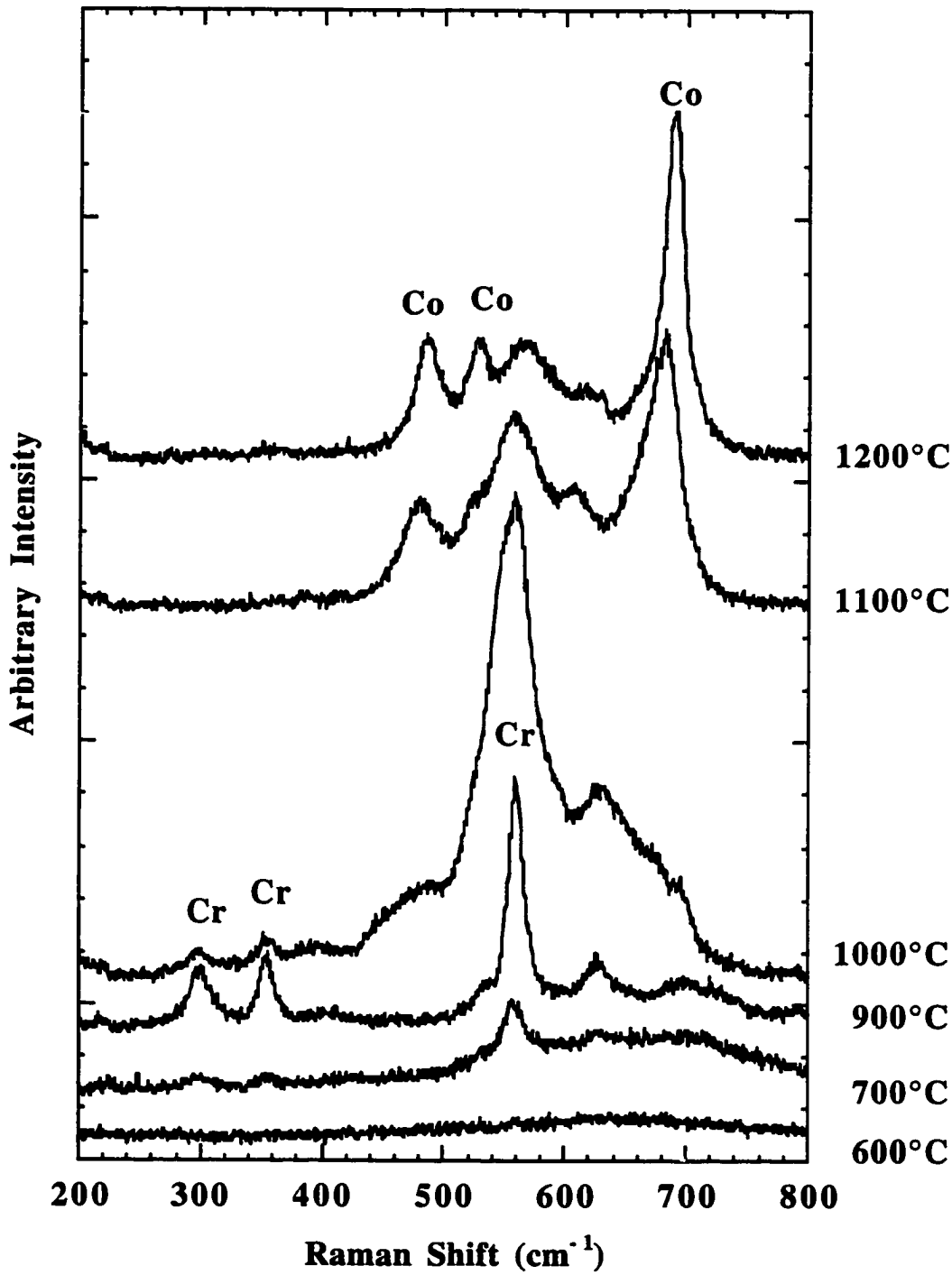

Figure 27. Raman Spectra From Oxidized MCrAl. Sequential oxidation in air for 1 hr at each of the indicated temperatures. The Cr and Co indicate Raman peaks from Cr_2O_3 and Co_3O_4 respectively. The * indicates plasma lines from the Kr laser.

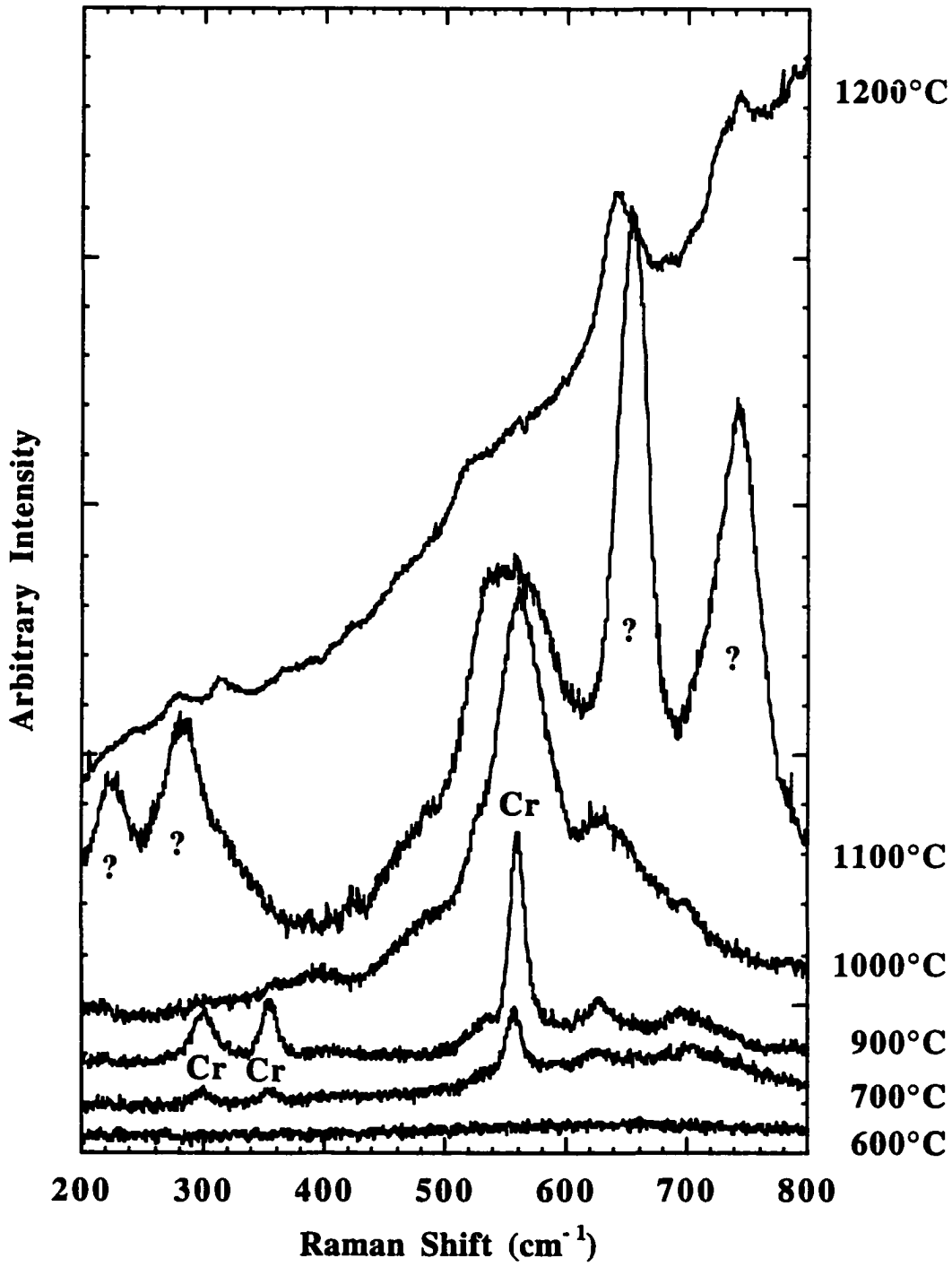

Figure 28. Raman Spectra From Oxidized MCrAlY. Sequential oxidation in air for 1 hr at each of the indicated temperatures. The Cr and ? indicate Raman peaks from Cr_2O_3 and an unidentified oxide phase respectively. The * indicates plasma lines from the Kr laser.

Here again we attribute this feature to an extremely disordered or perhaps an amorphous oxide layer. Above 700°C the Cr_2O_3 Raman peaks (labeled Cr in the figures) appear and dominate the spectra. After treatments at 1100°C and 1200°C extensive spallation was visually apparent in the Y-free sample. The Raman spectra of the scale that remains bonded to the alloy are dominated by Co_3O_4 peaks while Cr_2O_3 peaks were observed in the spalled material. Although it is tempting to conclude that spallation occurs at the Co oxide/Cr oxide interface, the present experiments do not allow us to rule out that the Co oxide is formed after spallation during cooling.

No spallation was visible on the MCrAlY sample at 1100°C and 1200°C and no Co_3O_4 peaks appeared in the Raman spectra. At these temperatures, however, we do observe Raman peaks from a phase we have not yet been able to identify. We do know that it is not due to any of the oxides we have fingerprinted thus far, nor to NiO or α-Al_2O_3. Although α-Al_2O_3 Raman peaks did not appear in the spectra taken from either the MCrAl or MCrAlY scales, we know it is present in the scale since we detect the ruby fluorescence.

Summary and Conclusion

This initial survey of the applicability of Raman spectroscopy to thermally grown oxide scales has yielded some very interesting results. Because of the short acquisition times, the lack of any sample preparation and the non-destructive nature of the technique, it is clear that, if the technique were applied to a newly invented high temperature alloy it would clearly provide a large amount of information about the transient and steady state oxide phases in the scale.

Raman spectroscopy clearly detects the presence of the following oxides: Cr_2O_3, α-Al_2O_3, Fe_2O_3, NiO, Co_3O_4 and HfO_2. The "fingerprinting" technique was found to be useful for identifying and tracking scale oxide phase behavior, during

transient oxidation, steady-state oxidation, and breakaway corrosion. We have also shown that scales are not composed of perfectly stoichiometric oxides, but contain phases with variable defect structures and with variable compositions. Although these disordered phases do have Raman signals, considerably more work is required before they can be reliably identified.

Scale stress is one of the principal causes of spallation and consequently it is of great interest. Prior to the ruby fluorescence technique, described in the next chapter, there were few convenient techniques for measuring scale stress. The ruby technique, however, only works for alumina scales. In principle, because Raman peak positions are sensitive to stress, they can also be used as a stress gauge. However because the position of the Raman lines are also sensitive to stoichiometric effects, the interpretation of the line shifts can be very complicated. A careful evaluation of the stoichiometric and compressional dependence will have to be undertaken before Raman spectroscopy can be used as a reliable tool for the measurement of scale stress.

CHAPTER V

RUBY FLUORESCENCE

Introduction

In the previous chapter we presented a comprehensive survey of the applicability of Raman spectroscopy as a tool for the investigation of the oxidation of stainless steels. Particularly, we studied steels used in high temperature environments where oxidation is often the principal source of failure. We have shown that the information extracted from the Raman spectra can be useful in developing an understanding the oxidation process. During the Raman investigation it was observed that many of the scales that formed on aluminum containing alloys fluoresced when irradiated with the laser. The origin of some of the florescence was found to be due to the presence of ruby in the scale. In this chapter we will focus all of our attention on the usefulness of the ruby fluorescence spectra, as a qualitative measure of the α-Al_2O_3 content in thermally grown scales, and as a quantitative measure of scale stresses.

Scale stress is one of the principal causes of spallation and consequently it is of great technological interest. The measurement of scale stress is, however, a difficult challenge and there has been no convenient technique which yielded this information. Although the ruby fluorescence has been used for decades as a stress indicator in diamond anvil cells [48] only recently has it been used to measure the stress levels in thermally grown oxide scales [12,32,35,64,71-78]. It is well known that the Cr impurities in α-Al_2O_3 produce the characteristic R-line fluorescence doublet at 6943 Å and 6929 Å. It is also known that the frequency of the fluorescence changes as a

function of the stress applied to the host material. Details relating the shift to average stress and or strain in a polycrystalline material can be found in Chapter II as well as in the literature [80-85]. Due to the fact that we are also interested in the oxide phases that compose the scale, we will also use the ruby fluorescence as a fingerprint for the presence of α-Al_2O_3 in the scale.

The equipment used to measure the ruby fluorescence is the same as that used to acquire Raman spectra, so it is a straight forward task to evaluate the sensitivity of our particular spectroscopy equipment to the fluorescence signal produced by a thin scale. Figure 29 contains example ruby spectra, taken from FA71 that has been systematically heat treated for one hour at the indicated temperature. Again the spectra have been rescaled and offset for clarity, and the signal strength for each spectrum (in counts per second) has also been included in the figure. The spectra were measured at room temperature, with acquisition times as long as 500 sec for the thinnest scales (i.e. below 850°C), and acquisition times as short as 1 sec for the thickest scale (i.e. 1000°C). Because of the short acquisition times, the lack of any sample preparation and the non-destructive nature of the technique, it is clear that if the information extracted from ruby spectra is useful in understanding the oxidation process, then the technique has a strong potential of becoming a powerful tool in such investigations.

In Figure 29, we see a dramatic increase in the fluorescence intensity as reaction temperature increases. We attribute this behavior to increasing scale thickness and an increasing fraction of α-Al_2O_3 in the scale. The lower spectrum in Figure 29, taken from a spalled scale, is identical to the bulk ruby fluorescence doublet. The other spectra in Figure 29 show red shifts indicative (Eq. 2.17) of a compressive stress in the

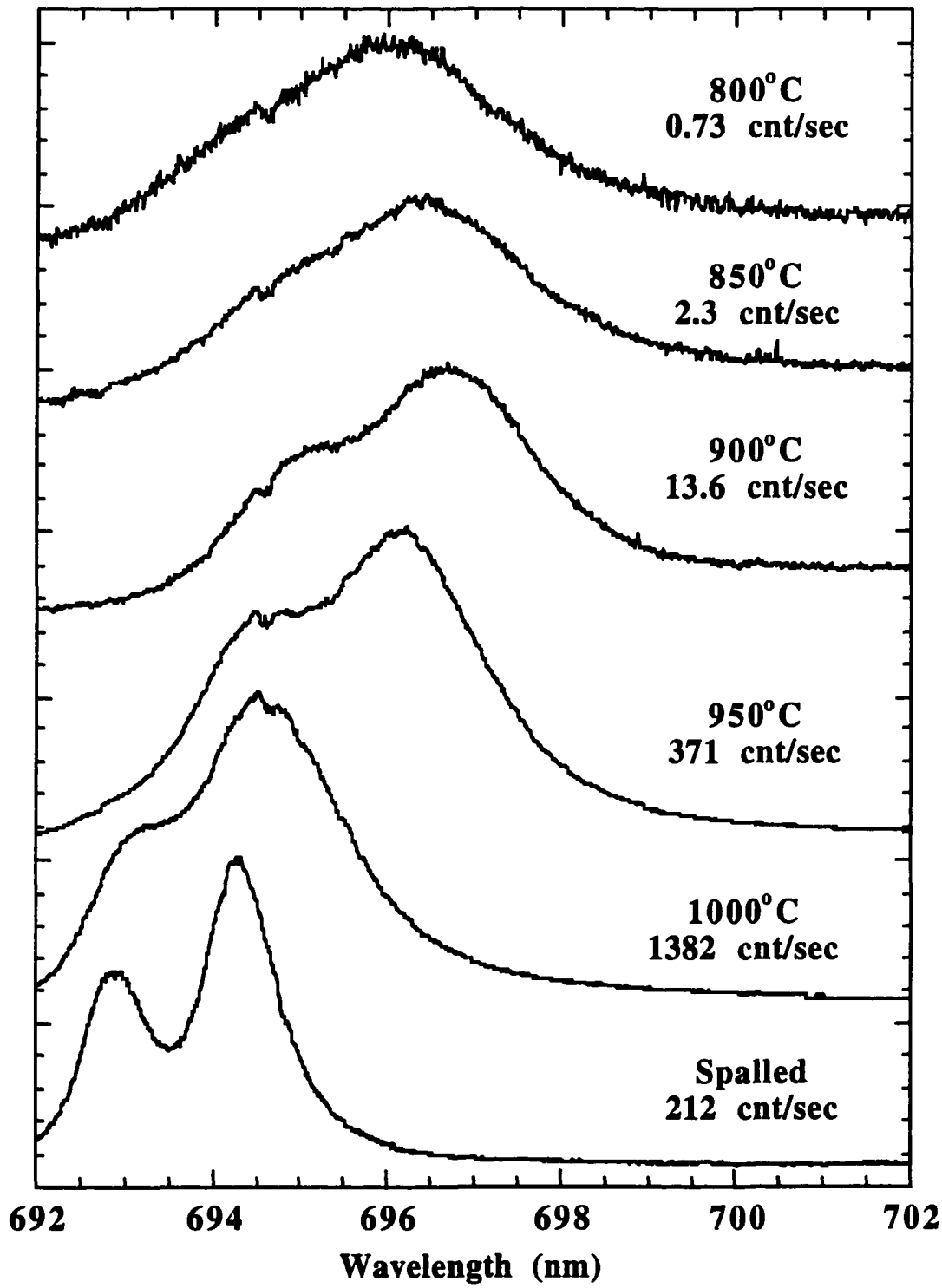

Figure 29. Ruby Fluorescence Spectra From Oxidized FA71. Sequential oxidation in air for 1 hr at each of the indicated temperatures.

scales. There is also substantial broadening of the spectra. Since broadening can be produced by a number of effects; e.g. crystalline anisotropy (which enters through the π_{ij} as well as the C_{ijkl}), strain inhomogeneity, point defect concentrations, etc., we make no attempt to extract information from the width of the ruby lines. Taking the shift in the peak position as a measure of the stress induced shift and applying Eq 2.17, we obtain the hydrostatic room temperature stress σ_H after the various heat treatments. By analyzing both the ruby intensity and peak position we are able to obtain information about the scale α-alumina content and the scale stress respectively.

The remainder of this chapter will be devoted to results extracted from spectra like the ones presented Figure 29. Consequently we will not be presenting ruby spectra but we will be reporting on peak intensities, peak positions, stresses and strains. We start by showing that the inclusion of a reactive element in an alloy has an affect on the intensity of the ruby doublet, and on the scale stress. We also compare strain data obtained from the ruby fluorescence technique to strain data obtained from X-ray diffraction.

As described in Chapter III Raman scattering and fluorescence studies can be performed with very high spatial resolution by the incorporation of microscope optics. Typically this type of equipment consists of a microscope interfaced to a spectrometer; our particular instrument allowed us to focus the incident laser beam down to ~2 microns and to collect the fluorescence from the illuminated region. This high spatial resolution has allowed us to investigate the stress field surrounding a surface convolution [86,87], and has allowed us to produce stress profiles near scale edges and corners [88,89].

The ruby technique for measuring stress has been applied to six of the alloys that were studied in the Raman investigation of the previous chapter. These are LBL, FA71, MCrAl, and the corresponding reactive element containing alloys LBL-Hf,

FAL, and MCrAlY respectively, where the compositions are given in the previous chapter. We find that, for thermally grown scales, sufficient Cr is supplied to the scale from the substrate material to produce a ruby doublet. We have also found many cases where the alloy is nominally Cr - free (i.e. NiAl), but contained sufficient Cr impurities for the scale to produce a ruby signal. The ruby frequency also has a temperature dependence, but since all observation were made at room temperature, it does not enter into our analysis. Since the changes in the ruby frequency observed in our investigations are quite large, the small frequency shifts due to changes in Cr concentration have been ignored [90].

Ruby Fluorescence Intensity

In the previous chapter we presented Raman spectra from four Fe-Cr-Al alloys, namely Fe-5Cr-28Al (FA71), Fe-5Cr-28Al-0.1Zr-0.05B (FAL), Fe-18Cr-10Al (LBL) and Fe-18Cr-10Al-0.5Hf (LBL-Hf), all compositions are in at% and the balance is Fe. Again Zr and Hf are the reactive elements that improve corrosion resistance. Here we report on the information obtained from ruby fluorescence spectroscopy. In this section we will discuss the fluorescence signal strength, in the following sections we report on the scale stresses and strains. The samples were given the same sequential thermal histories as the alloys in the previous chapter. Figures 30 and 31 are plots of ruby fluorescence intensity as a function of the treatment temperature for the scales accumulated on FA71/FAL and LBL/LBL-Hf respectively. The fluorescence signal is first detectable in the scales after the treatment at ~ 750°C. The intensity of this signal grows very rapidly as the sample undergoes the additional oxidation treatments. Above 1000°C the ruby signal from FA71 and LBL increases much more rapidly than the signal from their reactive element doped counterparts (FAL and LBL-Hf respectively).

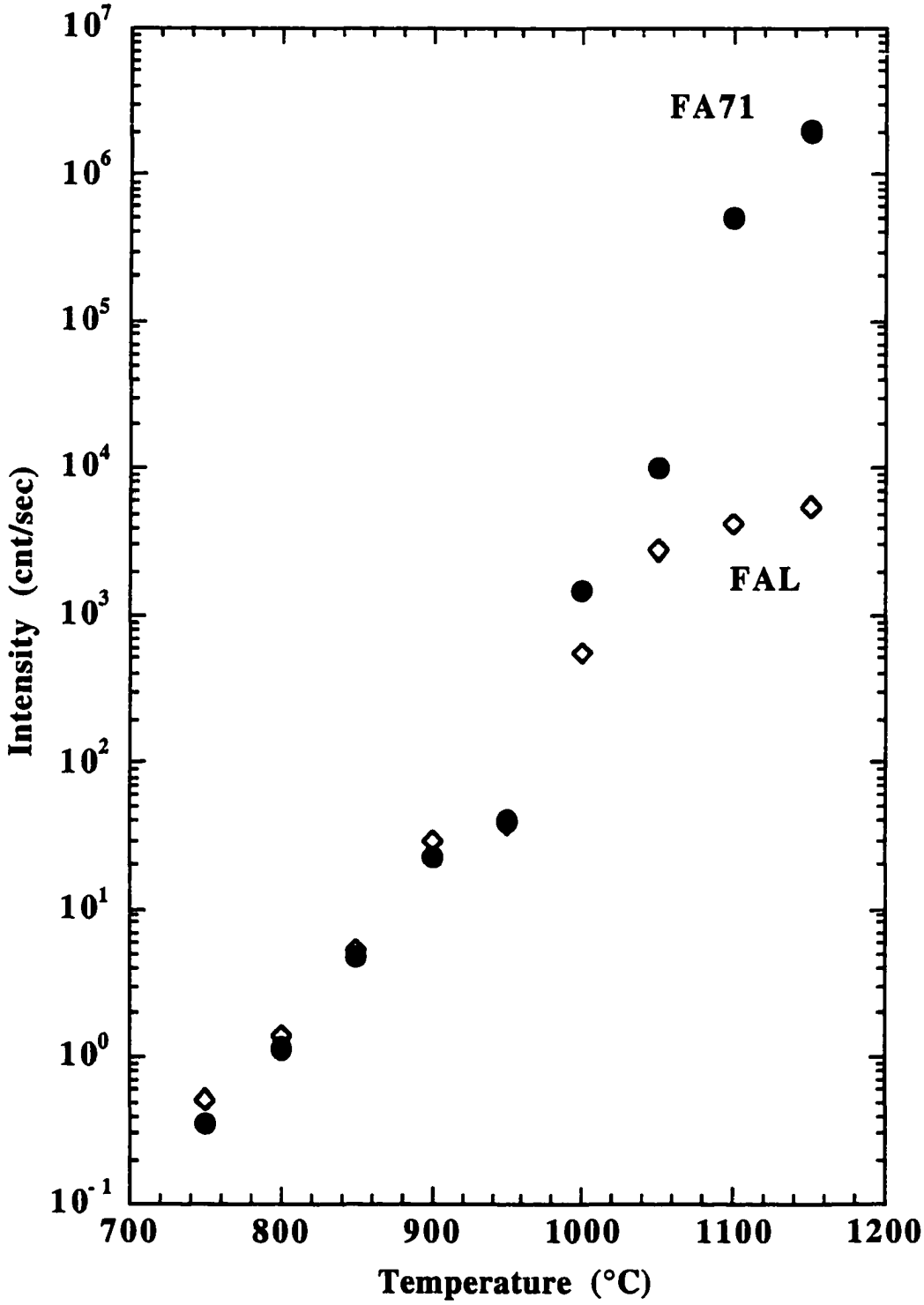

Figure 30. Ruby Fluorescence Intensities From Oxidized FA71 and FAL. Sequential oxidation in air for 1 hr at each of the indicated temperatures.

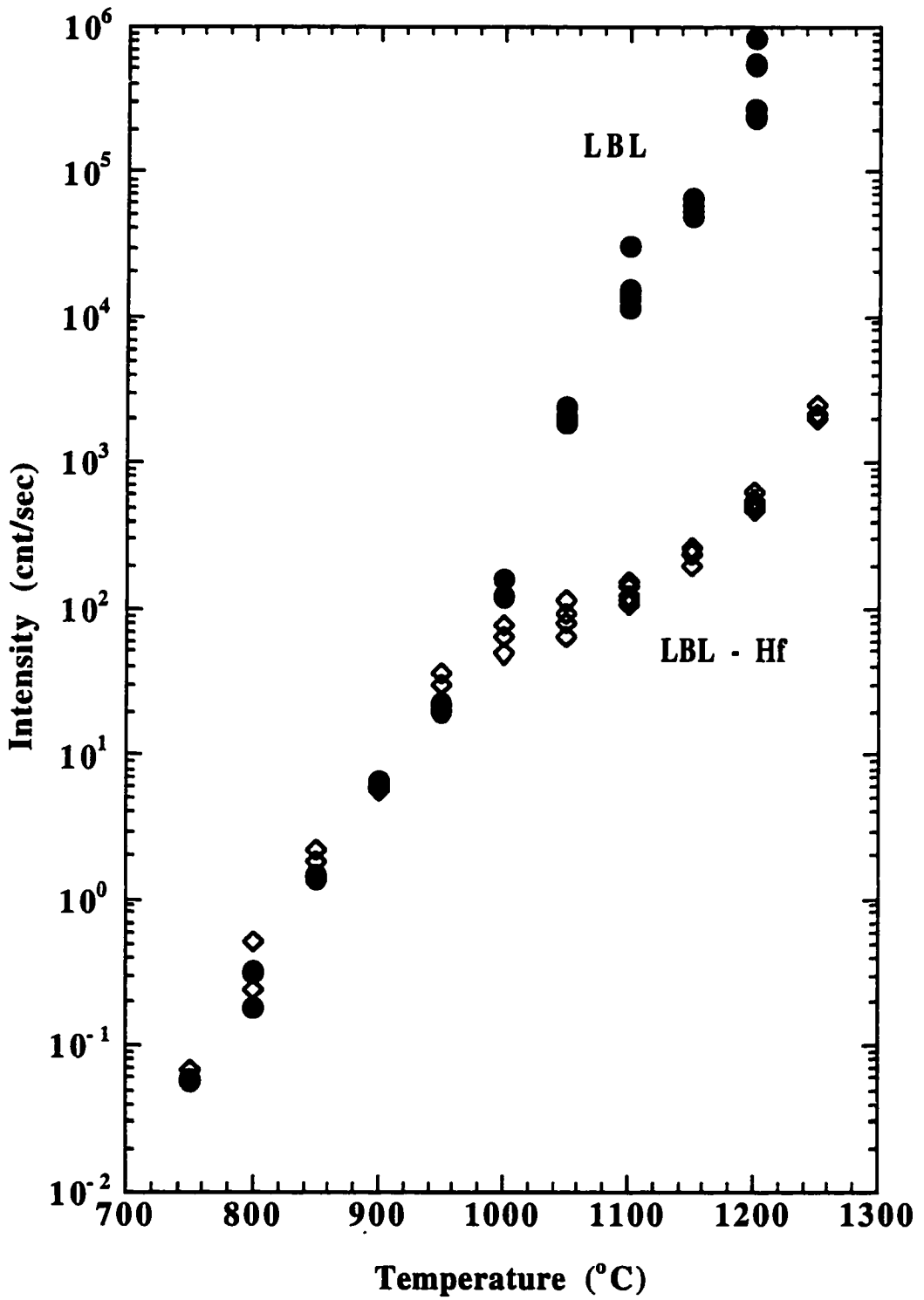

Figure 31. Ruby Fluorescence Intensities From Oxidized LBL and LBL-Hf. Sequential oxidation in air for 1 hr at each of the indicated temperatures. Each data point represents a different spot on the samples.

By 1100°C, the intensity difference, for both sets of alloys, is more than two orders of magnitude.

The two interesting trends in the intensity data are; the logarithmic temperature dependence, and the intensity difference between the alloys that contain a reactive element versus the respective reactive element free alloys. Because we know (see below) the scale thickness changes by about a factor of ~14, between 800°C and 1100°C, while the ruby signal strength increases by a factor of ~250, we conclude that most of the change in the fluorescence signal strength results from an increase in the fraction of α-Al_2O_3 in the scale. This might occur by direct growth or by conversion of metastable oxide phases (e.g. θ-, κ- or γ-Al_2O_3) to α-Al_2O_3. Consequently the reactive element must play a role in slowing the growth of α-Al_2O_3 and/or in slowing the conversion of transition aluminas to α-Al_2O_3. This conclusion is consistent with the Raman data (Figures 25 and 26) taken from the FA71/FAL scales that show that the α-Al_2O_3 Raman peaks are about 10 times stronger in the scale that formed on FA71 than in the scale that formed on FAL. However, the only evidence that we have of the existence of transient alumina in the scales is a weak κ-Al_2O_3 Raman peak, presented in Figure 25, acquired from FA71 after the 1050°C heat treatment.

To further our understanding of the phase transition in alumina, we have recorded fluorescence spectra from powders of nominally pure γ-Al_2O_3 and from γ-Al_2O_3 doped with 1 wt% ZrO_2. The powders samples were mixed, ball milled and pressed into pellets. Then sequentially heat treated from 400°C to 1200°C in steps of either 50°C or 100°C, for one hour at each temperature. The recorded fluorescence intensity data is plotted in Appendix B. As in the scales, we found a similar logarithmic temperature dependence and a large discrepancy in the signal intensity for the doped and undoped samples. The discrepancy is close to a factor of 12, which is similar to what is seen in the scales. X-ray and Raman measurements were also made of the

powder samples, and they support the phase transformation explanation of the fluorescence data.

Before we can unequivocally claim that the behavior observed in Figures 30 and 31 is due to a phase transition we must consider the change in the scale thickness and the change in the scale Cr content. Coworkers of the author, using optical reflectivity [89] and refracted X-ray fluorescence techniques [91], have performed careful scale thickness measurements on a sample of LBL-Hf that was subjected to a similar sequential thermal history as the sample in Figure 31. They reported an average scale thickness of 0.07 μm at 800°C and 0.95 μm at 1100°C [92]. This can account for an increase in ruby fluorescence intensity a bit larger than one order of magnitude. However, for the same temperatures in Figure 31 the ruby fluorescence intensity increases by more than two and a half orders of magnitude for the LBL-Hf sample, and four and a half orders of magnitude for LBL. This leads us to conclude that the change in the scale thickness contributes to part of the logarithmic temperature dependence of the fluorescence intensity.

However at higher temperatures (i.e. 1100°C) the reactive element free alloys would have to have a two orders of magnitude thicker scale than their reactive element doped counterparts. Since no such thickness difference has been measured at Argonne National Laboratory, the scale thickness variations can not account for all of the behavior observed in Figures 30 and 31.

SEM (Energy Dispersive X-ray Analysis) measurements, performed by coworkers of the author [91], on the scales that form on the LBL and LBL-Hf samples indicate that the Cr content drops by about a factor of three between 900°C and 1150°C. The scale Cr concentration was also found to be unaffected by the presence of a reactive element in the alloy. The SEM finding leads us to conclude that the observed behavior in Figures 30 and 31 can not be due to variations of Cr content in the scale.

Reactive Element Effect

As discussed in the previous section, the fluorescence signal strength is clearly affected by the presence of a reactive element in the alloy. Here we report on the effects that the reactive element has on the scale stress. Figure 32 shows the residual scale stresses as determined from the ruby fluorescence peak position. The stresses were calculated using Eq. 2.17 and represent the hydrostatic component of the stress. Since the values are negative they indicate that the stresses are compressive. The open diamonds and closed circles represent FAL and FA71 respectively. Up to ~ 900°C, both alloys show scales that develop increasing compressive stress as the reaction temperature is increased. At T ~ 950°C, the FA71 alloy begins to show stress relaxation indicating the onset of scale failure. With increasing reaction temperature, the scale exhibits catastrophic failure and apparently becomes completely debonded at T > 1000°C; small spalled flakes are visually observable. For the accumulating scale on FAL, however, increasing compressive stress-buildup is observed to the temperatures of 1150°C. This is a dramatic manifestation of the reactive element effect: samples containing a reactive element develop thermally grown scales that are capable of sustaining substantially larger compressive stress than scales on the reactive element free alloys. The spread in the data represent the spot to spot variation on the surface. In some cases they correspond to stressed and almost stress free regions which we interpret as non-uniform stress relief, presumably associated with micro-cracking or debonding in specific regions of the scale.

In order to develop a better understanding of the scale stress presented in Figure 32 we have calculated the stress expected from the thermal expansion mismatch between α-alumina and the alloy (solid line in the Figure). An analytical solution exists for the

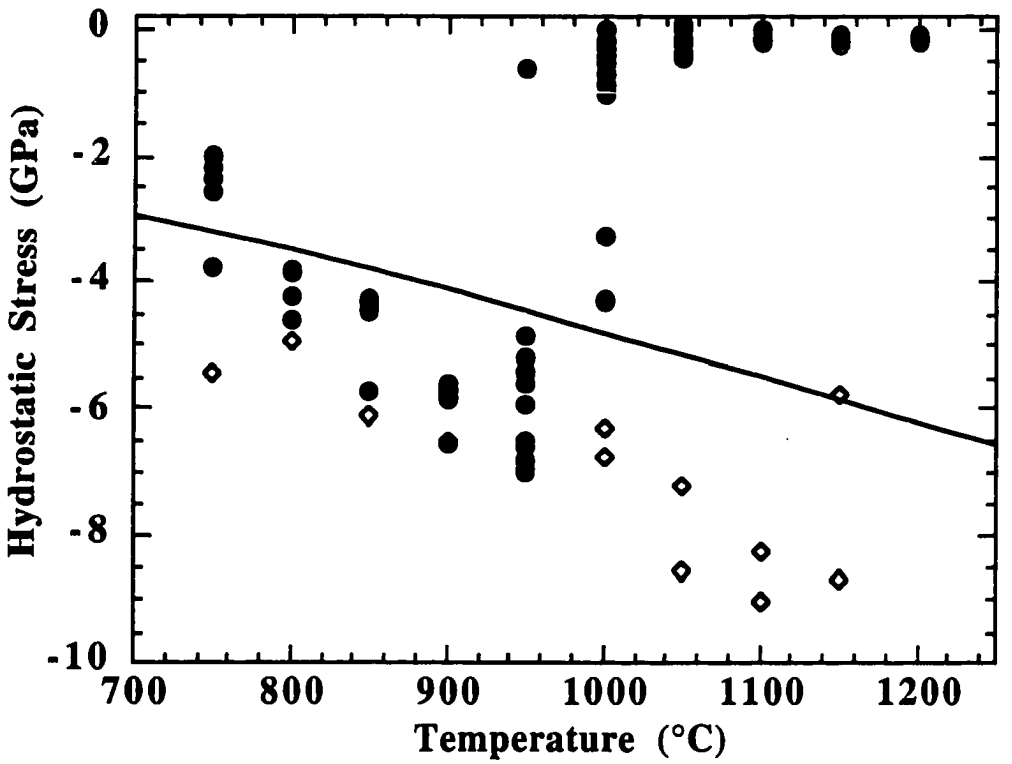

Figure 32. Hydrostatic Stress FA71 and FAL. Solid circles and open diamonds correspond to FA71 and FAL respectively. Each data point represents a different spot on the samples.

uniaxial stress in an infinite plate of joined dissimilar materials.[93,94] Assuming elastic behavior, uniform cooling, constant mechanical and thermal properties, the uniaxial stress (σ_S) in the scale is given by:

$$\sigma_s = [E_s/(1 - \nu_s)] (\alpha_s - \alpha_a) \Delta T \qquad 5.1$$

Where E_s and ν_s are Young's modulus and Poisson's ratio of the scale respectively. The α_s and α_a are the temperature dependent coefficient of thermal expansion of the scale and alloy respectively [95,96]. The ΔT is the temperature change on cooling. Since the stress is biaxial (and the component normal to the interface is zero) the hydrostatic stress is $\sigma_H = 2\sigma_s/3$. Because the α_a of FA71 and FAL are not known, we

have used thermal expansion data for FA129 (Fe-5Cr-28Al-0.5Nb-0.2C [95]) since it is expected to be close to that of FA71 and FAL. For an α-Al_2O_3 scale we use 380 GPa and 0.25 for Young's modulus and Poisson's ratio respectively [97,98]. Equation 5.1 is offered as an estimate of the expected stress for the case where the scale thickness is much much thinner than the alloy. In a following section we will incorporate scale and substrate thickness information into equation 5.1. The calculation also does not account for growth stress or creep effects. Because the calculated thermal stress is less than the measured stress, we might conclude that compressive growth stresses have developed and they add to the thermal mismatch stress. To reconcile the measured and the calculated stress may require more accurate thermal expansion and mechanical data. To determine the role of growth stress, the scale stress could be measured at the oxidation temperature, prior to the thermal cycling that produces mismatch stresses. However the ruby fluorescence technique can not be used at high temperature, so perhaps an in-situ x-ray investigation may be required.

Figure 33 shows the residual scale stress measurements for the LBL alloys. The open diamonds and closed circles represent LBL-Hf and reactive element free LBL alloys respectively. Again the solid line is the calculated thermal mismatch stress (Eq 5.1). The thermal expansion data is from an alloy with composition Fe-18Cr-5Al [99], which we consider to be comparable to the LBL alloys. In these scales, the stress buildup resulting from oxidation at a given temperature is substantially smaller than what is observed in FAL and FA71. It is also less than that expected from thermal mismatch. Stress relaxation begins to occurs near 1000°C in the Hf-free alloy (Figure 33), but unlike FA71, relief is gradual without abrupt change. As in Figure 32 we observe that substantially larger stress can be sustained in the scale grown on the alloy that contains the reactive element. Again the spread in the measured stress values is

attributed to non-uniform stress relief, presumably associated with local microcracking or local debonding.

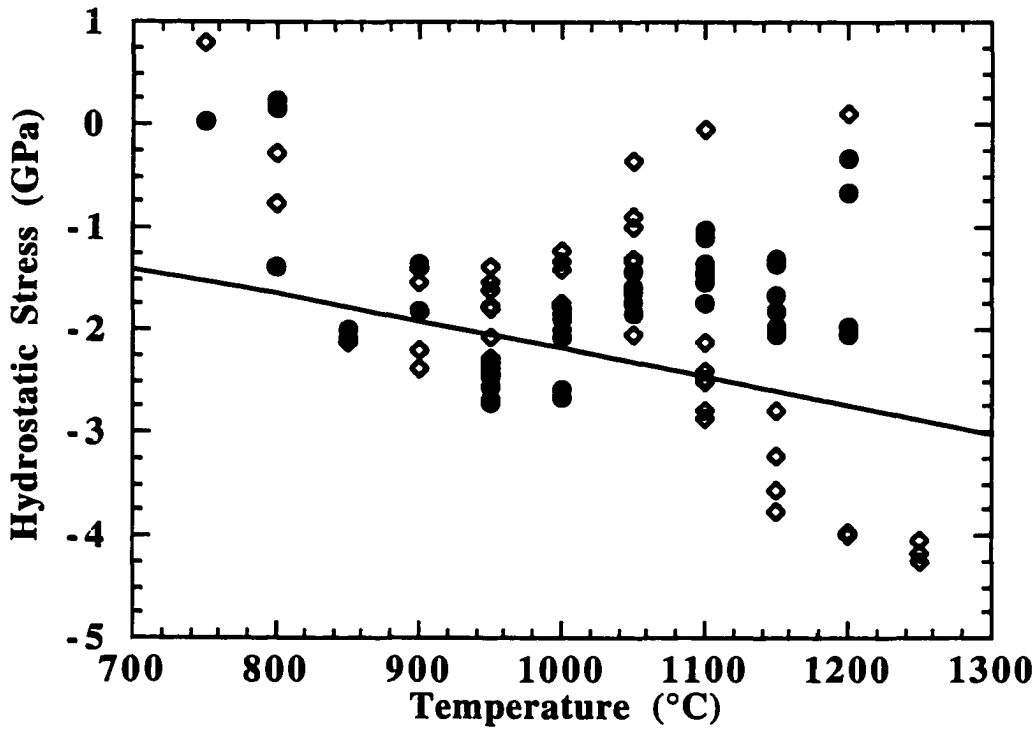

Figure 33. Hydrostatic Stress LBL and LBL-Hf. Solid circles and open diamonds correspond to LBL and LBL-Hf respectively.

The smaller stresses observed in the thermally grown scales on both of the LBL alloys (Figure 33) are due mostly to smaller coefficients of thermal expansion than those of FA71. The gradual stress relaxation of the reactive element free LBL alloy can be traced to the peculiar interface morphology that has been observed after oxidation in these alloys [64,78,79,100]. A cross section showing the scale-metal interface (presented later) reveals a nearly sinusoidal pattern with a wavelength of a few microns. The reactive element free LBL alloy is the only sample investigated that produces this convoluted surface morphology, all the remaining alloys maintain planar interfaces. In

a following section we will investigate the stresses in the vicinity of the convolutions by using the micro-florescence technique.

We know from Raman measurements that the mature scales that form on the Fe-Cr-Al alloys consist mostly of α-alumina. For the MCrAl and MCrAlY alloys (M= Ni and Co), the Raman spectra show the scales contain mostly chromia. In spite of this, we found, that enough α-alumina was present in the MCrAl(Y) scales to produce ruby spectra, thus allowing us to study the reactive element effect in this alloy (Figure 34).

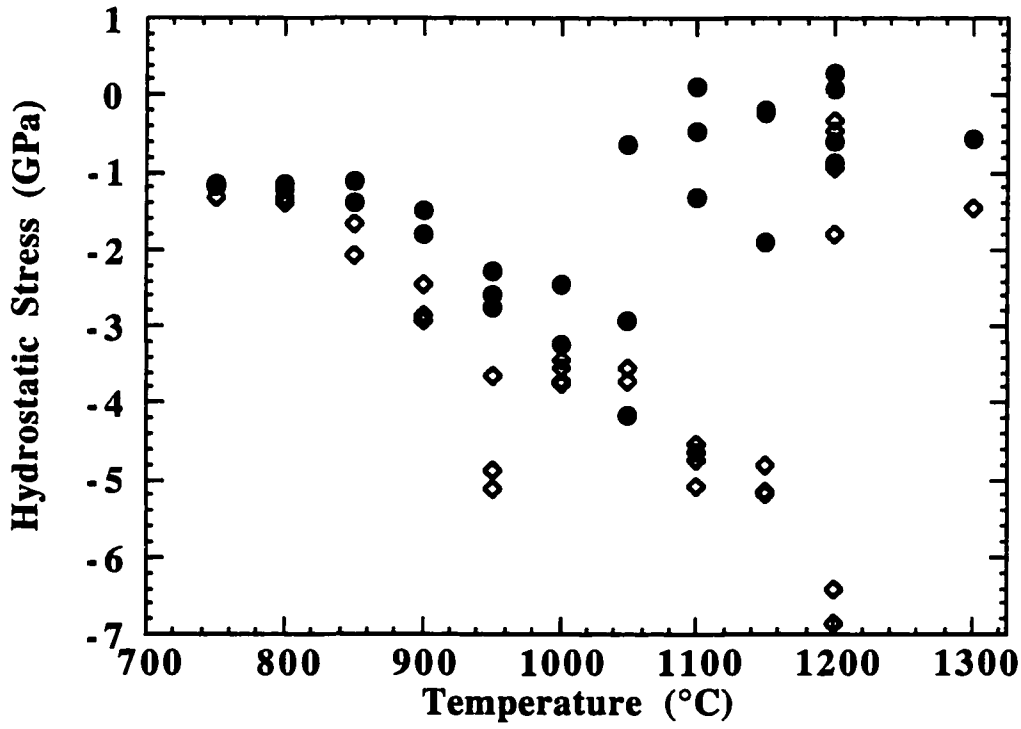

Figure 34. Hydrostatic Stress MCrAl and MCrAlY (M=Ni, Co). Solid circles and open diamonds correspond to MCrAL and MCrAlY respectively.

Ruby fluorescence was detected after heat treating at temperatures as low as 750°C. This indicates the presence of α-Al_2O_3 and permitted us to estimate the room temperature compressive stress in the scale, as shown in Figure 34. The scales on both alloys show an increasing compressive stress as the oxidation temperature is increased.

At T~1050°C MCrAl begins to show signs of stress relaxation indicating the onset of failure. At 1100°C and above, the scale exhibits near total stress relief, indicating catastrophic scale failure: large spalled flakes were also visible on the surface. Contrary to MCrAl, the accumulated scale on MCrAlY exhibits increasing stress to temperatures of about 1150°C, indicating that the scale is still bonded. At 1200°C we observe signs of stress relaxation and total stress relief at 1300°C. Figure 34 again provides a beautiful demonstration of the reactive element effect.

Scale strain measurements, using X-ray diffraction, have been reported for MCrAl(Y) alloys (M = Fe, Ni, Co) [101]. For considerably longer heat treatments (~80 hrs, T~1200°C) the scales that formed on the Ni-Co based MCrAlY, were found to be strain free. This is consistent with our observations that at 1200°C the scale on this alloy starts to stress relieve after roughly one hour.

Strain Determination by X-ray Scattering

In this section we describe an x-ray characterization of the strains in Fe-Cr-Al alloys. These experiments were undertaken for the purpose of confirming that the stress extracted using the ruby technique is reliable and provides a quantitatively correct measure of stress and strain. Our experiments were carried out at room temperature in the θ-2θ geometry using a rotating anode source and a multichannel detector. In spite of these technical enhancements, we were unable to detect signals from scales grown below ~1000°C. In the geometry we used, only lattice spacings normal to the sample surface were probed. Typically the spectra contain peaks from the substrate and from the oxides in the scale. The α-Al_2O_3 peaks can be identified and their positions determined as a function of oxidation temperature. A typical spectrum is presented in Figure 35 for a FA71 sample oxidized at 1150°C The prominent α-Al_2O_3 peaks are identified and labeled.

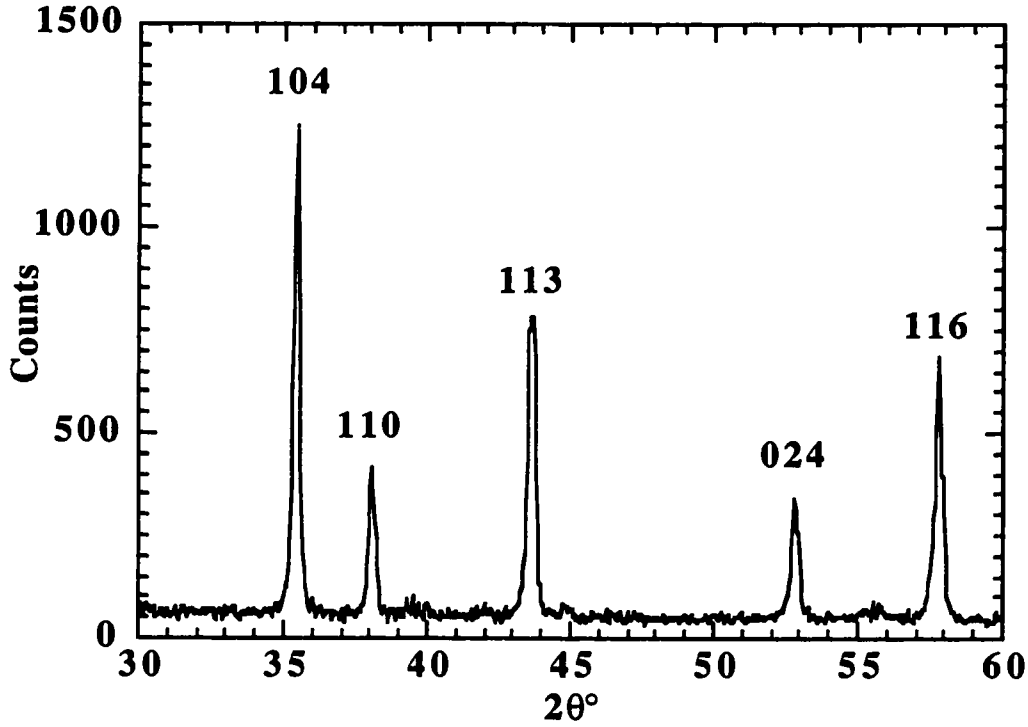

Figure 35. X-ray Diffraction Spectrum From the Scale That Formed on FA71. Sample oxidized in air, at 1150°C for 1 hr.

X-ray measurements of thermally grown alumina scales show expansions (relative to an α-Al_2O_3 standard) along the normal to the sample surface. The expansion can be determined by the shift in the 2θ angle of each Bragg reflection. Figure 36 shows the relative shift of the (113) peak from a strained scale with respect to a polycrystalline unstrained standard. The shift to smaller 2θ in the peak from the scale indicates expansion. Further, we report that, for a given oxidation temperature, the expansion is the same, within experimental error, for all of the α-Al_2O_3 peaks in the spectrum. This agreement in the strain measurements for the different peaks shows that the expansion perpendicular to the surface is independent of the orientation of individual grains. Qualitatively the expansion observed with x-rays is consistent with a biaxial compression caused by the thermal expansion mismatch.

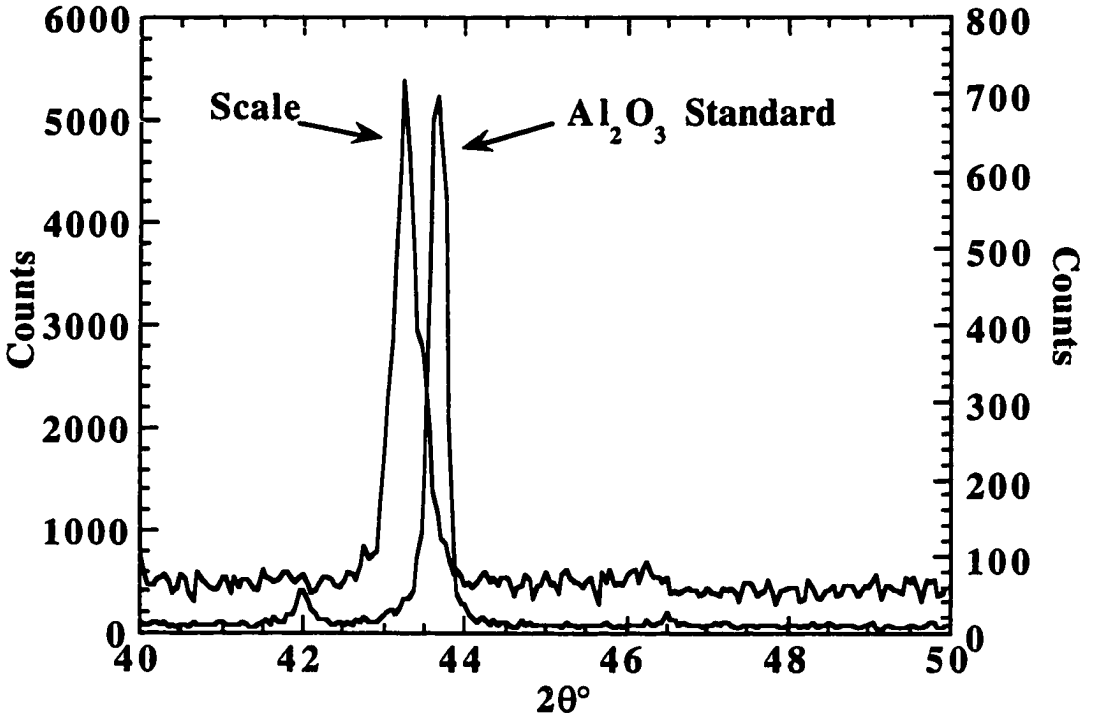

Figure 36. Comparison of (113) Bragg Peak From a Strained Scale and a Unstrained Polycrystalline Standard. The scale was formed on FAL after oxidation in air at 1150°C for 1 hr.

In order to quantitatively compare the x-ray strain measurements to the ruby stress measurements we need to take a closer look at how hydrostatic stress and perpendicular strain are related to the biaxial compressive strain. Eq. 2.17 relates the frequency shift to hydrostatic stress, which can be rewritten in component form, as:

$$\Delta\nu = 7.53 \, (\sigma_{11} + \sigma_{22} + \sigma_{33})/3 \qquad 5.2$$

Upon cooling to room temperature the thermal mismatch between scale and (isotropic) substrate produces a biaxial in-plane scale strain, $(\alpha_s - \alpha_a)\ \Delta T$. The resulting stress in the scale is also biaxial so that $\sigma_{11} = \sigma_{22} = \sigma_{in}$ and $\sigma_{33} = \sigma_{out} = 0$. Eq. 5.2 can be written.

$$\Delta\nu = 2/3 \, (7.53 \, \sigma_{in}) = 5.02 \, \sigma_{in} \qquad 5.3$$

For α-Al_2O_3, we use the known elastic constants to relate strain (ε_{ij}) to the σ_{in} stress component. By assuming the shear stresses and strains are negligible, Hook's law can be written as follows.

$$\sigma_{11} = C_{11}\varepsilon_{11} + C_{12}\varepsilon_{22} + C_{13}\varepsilon_{33} \qquad 5.4$$
$$\sigma_{22} = C_{12}\varepsilon_{11} + C_{22}\varepsilon_{22} + C_{13}\varepsilon_{33}$$
$$\sigma_{33} = C_{13}\varepsilon_{11} + C_{13}\varepsilon_{22} + C_{33}\varepsilon_{33}$$

The C_{ij} are elastic constants and for α-Al_2O_3, they are [102]: $C_{11} = 465$, $C_{33} = 563$, $C_{12} = 124$, $C_{13} = 117$. In principle Eq. 5.4 should be simultaneously solved for all grains in the scale. Since this is not possible it is reasonable to average only the three principal orientations.

The three orientations we consider consist of the c-axis of the Al_2O_3 crystal lying along each of the principal axis of the substrate frame, i.e. the c-axis lies along either of the two orthogonal directions in the plane of the substrate or along the substrate normal. Eqs. 5.4 can be solved for these orientations to give three relations between in plane strain and out of plane strain.

$$\varepsilon_{out} = -(2C_{13}/C_{33})\, \varepsilon_{in} \qquad 5.5$$
$$\varepsilon_{out} = -(C_{12}/C_{11} + C_{13}/C_{11})\, \varepsilon_{in}$$
$$\varepsilon_{out} = -(C_{12}/C_{11} + C_{13}/C_{11})\, \varepsilon_{in}$$

By using the accepted values for the elastic constants we obtain an average value relating the out of plane relaxation due to the in plane compression.

$$\varepsilon_{out} = (-0.484 \pm 0.068)\, \varepsilon_{in} \qquad 5.6$$

The uncertainty in Eq. 5.6 reflects the anisotropies of the elastic constants in Eq. 5.5.

The same approach we used to find Eq. 5.6 can be used to find a relation between in plane stress and in plane strain.

$$\sigma_{in} = (559 \pm 40) \varepsilon_{in} \qquad 5.7$$

Again the uncertainty in the above values is due to the anisotropic nature of the elastic constants.

Using Eqs. 5.3, 5.6 and 5.7, we obtain a relation between out of plane strain and the fluorescence frequency shift;

$$\Delta\nu = (5798 \pm 415) \varepsilon_{out} \qquad 5.8$$

where $\Delta\nu$ is expressed in cm^{-1}. This last equation allows us to make a quantitative comparison of the ruby and x-ray data.

In Figure 37 we show the perpendicular scale strain, from samples of FA71 and FAL, measured with x-rays (open symbols) and obtained from the ruby line shift measurements and using Eq. 5.8 (filled symbols). Error bars for the x-ray measurements correspond to the spread in strains obtained from the different diffraction peaks. Although the x-ray error bars are large, they do confirm that our analysis of the ruby data produces a very complete and consistent picture of the stress and strains in oxide scales. It should be noted that although it is possible to obtain strain information using x-rays, errors can be large. We could only use x-rays to measure strain in scales that formed at temperatures above 1000°C. We had to use large sample surfaces and the minimum data acquisition time was 26 min.

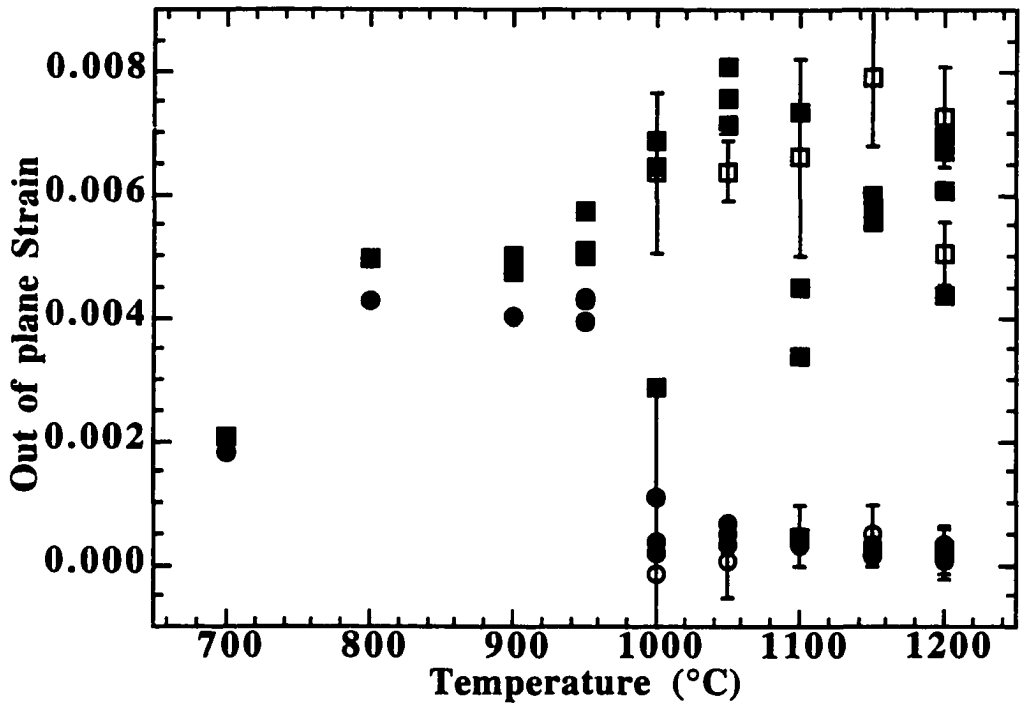

Figure 37. A Comparison of Out-Of-Plane Strain, as Determined by X-ray Diffraction and by Ruby Fluorescence. The FA71 and FAL samples were oxidized in air for 1 hr at each of the indicated temperatures. Full circles and full squares correspond to fluorescence measurements of FA71 and FAL respectively. Open circles and open squares correspond to x-ray measurements of FA71 and FAL respectively.

Alloy Thickness Dependence

Above we assumed the role that the scale and alloy thickness have on the thermal mismatch stress is small (Eq. 5.1). In this section we will investigate this assumption. To facilitate our inquiry we used four coupons of FA71 and four coupons of FAL, all having dimensions of approximately 0.5 cm square. The samples were carefully thinned to thickness ranging from 65 μm to 1150 μm. All six faces of each sample were polished with 1 micron diamond polishing grit. The FA71 samples were oxidized in air at 900°C for two hours, where they developed a 0.55 μm thick scale. The FAL samples were oxidized in air at 1000°C for four hours, where they developed

a 0.88 μm thick scale. None of the samples showed evidence of cracking or detachment. After the heat treatment fluorescence spectra were measured at room temperature. A coworker of the authors measured the scale thickness by using the interference patterns of reflected visible light resulting from the contributions from the air-oxide and metal-oxide surfaces [89].

In Figure 38 we have plotted our measured hydrostatic scale stresses from the FA71 (full circles) and FAL samples (open diamonds) versus the indicated alloy thickness. Each plotted value is the average of all points measured for a given thickness. The error bar is twice the standard deviation divided by the square root of the number of points. The figure also contains an analytical solution (full line) for the thickness dependent hydrostatic stress in a laterally infinite plate of joined dissimilar materials [93,94]. By assuming elastic behavior, uniform cooling, and constant mechanical and thermal properties, the uniaxial stress (σ_s) in the scale is expected to be given by:

$$\sigma_s = \{[E_s/(1-\nu_s)]\,(\alpha_s - \alpha_a)\,\Delta T\}/\{1 + [E_s/(1-\nu_s)]t_s / [E_a/(1-\nu_a)]t_a\} \qquad 5.9$$

Again E is Young's modulus, ν is Poisson's ratio, α is the temperature dependent coefficient of thermal expansion, ΔT is the temperature change on cooling, t is the thickness and s and a indicate scale and alloy respectively. Eq. 5.9 reduces to Eq. 5.1 for the limiting case of a scale that is much much thinner than the alloy. As described before the hydrostatic stress is $\sigma_H = 2\sigma_s/3$. For α-Al_2O_3, we used 380 GPa and 0.25 for E and ν respectively. For the alloy we used 141 GPa and 0.30 for Young's modulus, and Poisson's ratio respectively.

We see from the calculations that for the alloy and scale thicknesses investigated there is no clear effect on the expected scale stress. The overall agreement between the

experiment and calculations is quite good, considering that equation 5.9 considers only elastic thermal stress.

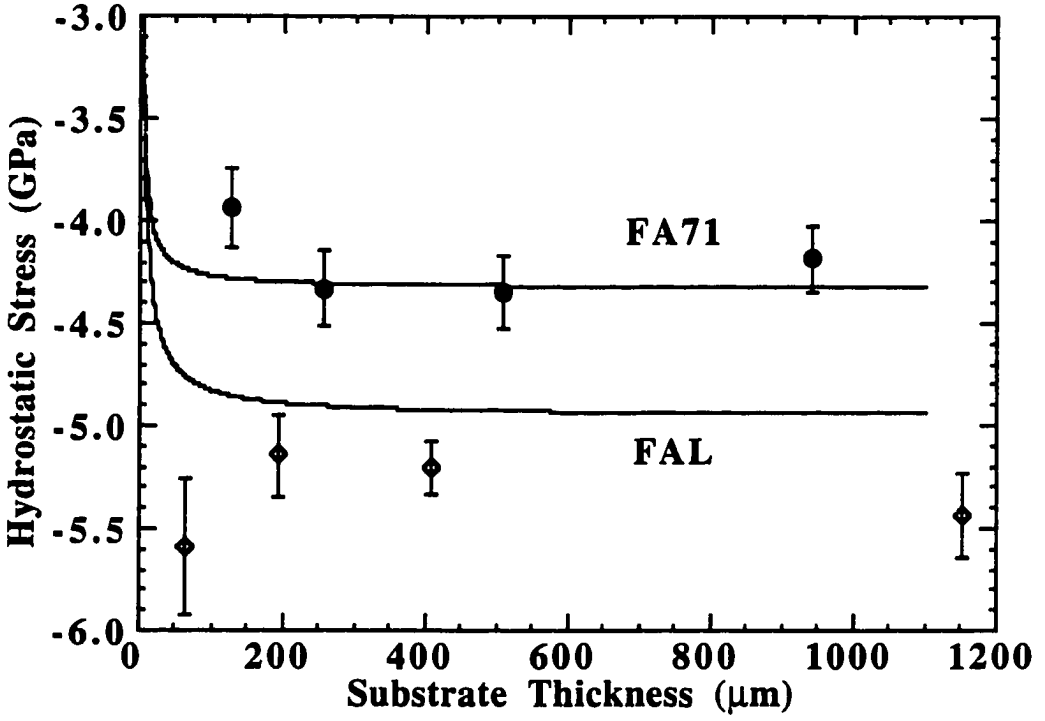

Figure 38. Average Measured and Calculated Stress vs. Substrate Thickness. FAL oxidized in air, at 1000°C for 4 hr (open diamonds) and FA71 oxidized in air, at 900°C for 2 hr (full circles).

Apriori there are a large number of other possible contributions to residual-stress accumulation and relaxation, such as, growth stresses, creep, scale phase composition, scale and alloy phase transformations, debonding, cracking, etc. A full treatment of this phenomenon is therefore extremely complex, especially when it is difficult to make initial assumptions regarding which effects are likely to contribute most strongly in a given instance. However it clear from Figure 38 that the thermal expansion mismatch is probably the most important origin of scale stress and for these systems the scale and alloy thickness play a lesser role.

Micro-Fluorescence

In the above section we acquired the ruby fluorescence data using the macro-fluorescence scattering geometry, which has a sample probe size of ~80 μm. In this section the fluorescence spectra were acquired in the backscattering geometry through a microscope which allowed the laser to be focused to about 1 μm. This increased spatial resolution allowed us to examine the scale stress behavior close to a sample edge and in the vicinity of a sample corner, where the stress field is no longer biaxial. The microprobe also provided us with the ability to examine a scale/alloy system that does not have a planar interface, again where the stress can not be assumed to behave biaxially.

Edge Effect

Stress distributions close to edges are of particular interest because spallation and debonding often seem to occur in their vicinity [103,104]; this is often interpreted as an indication that edges are regions of stress concentration. For the purpose of this work the study of these regions of the samples can help us develop a deeper understanding of the measured hydrostatic stress. Because we are now able to obtain experimental data with high spatial resolution, made possible by the micro-fluorescence technique, we have the ability to explore the sample edge in detail. The samples investigated in this section are the FA71 samples describe in the previous section; the alloy thicknesses ranged from 127 μm to 940 μm the scale thickness was 0.55 μm.

Figure 39 (top) is a micrograph of a corner of one of the oxidized samples. A schematic view of the sample corner (bottom), shows with black dots the approximeate positions on the surface where micro-fluorescence spectra were recorded.

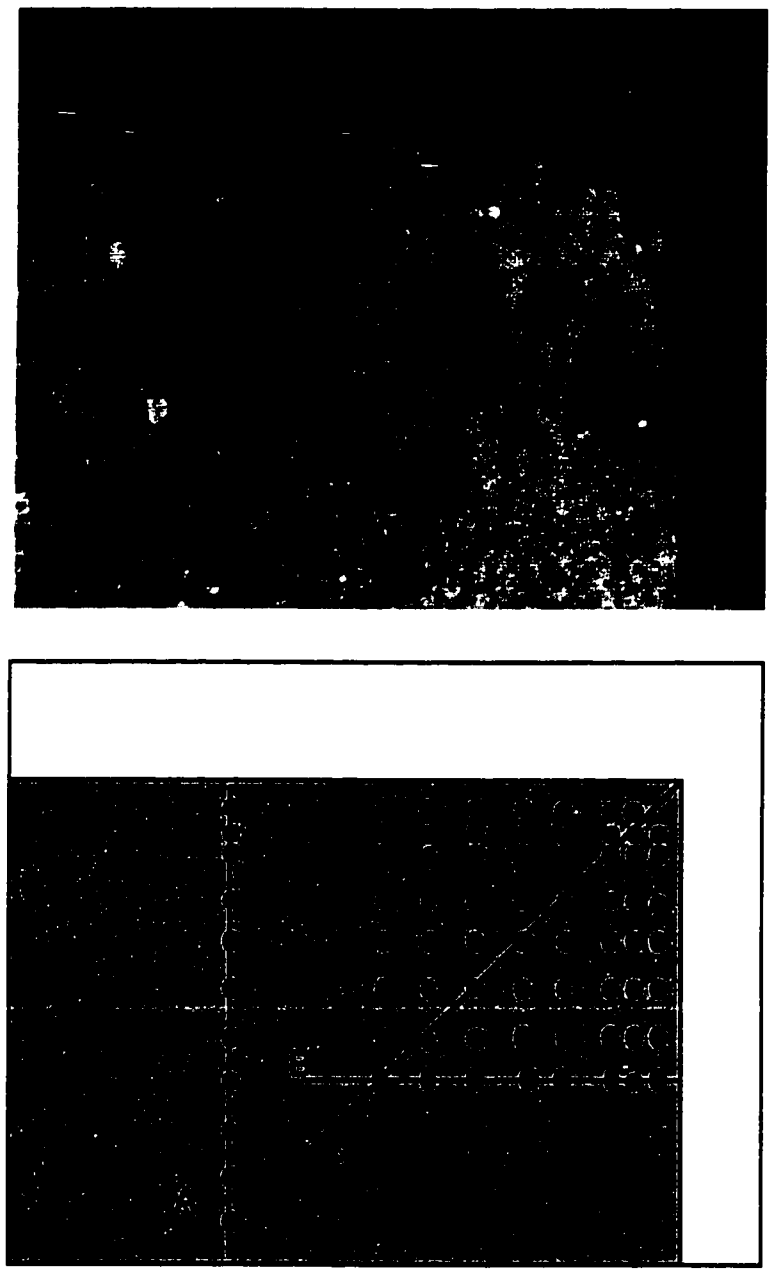

Figure 39. Micrograph (Top) of a Corner of Oxidized FA71 and Schematic View (Bottom) of the Corner. The black dots are the approximeate positions on the surface where micro-fluorescence spectra were recorded.

The stress behavior close to an edge and a corner is exhibited in Figures 40 and 41. In Figure 41 we show a three dimensional plot of the hydrostatic stress measured

on the matrix shown in Figure 39 (bottom). In Figure 40, we plot the hydrostatic stress as a function of distance from the corner along the corner diagonal (filled triangles) and as a function of distance from an edge (filled squares) corresponding to lines C and B respectively (Figure 39 bottom). It should be noted that the corner of the sample, top of Figure 39, shows a small amount of rounding; the radius of curvature is approximately 3 μm. Because the stress could not be measured at the exact corner, in Figure 41 the data point at (1.72 μm, 1.72 μm) is an average of the three adjacent points. Anticipating the comparison with calculations to be presented later, we emphasize that all our stress determinations were made on the flat surface of the sample; we did not attempt to probe the region where the sample is rounded. This rounded portion, where two faces meet, is comparable in size to our laser spot and hence we do not have the necessary resolution to probe it in detail.

Figures 40 and 41 show that, at the corner, the hydrostatic stress is approaching zero indicating that there is nearly complete relaxation of the hydrostatic stress. The figures also show the hydrostatic stress close to the sample edge is about one half the stress value far from the edge. We also observe a large stress decay length. Note in Figure 40 the stress relaxation extends to a distance of about 10 μm, which is about 20 the scales thickness. Some of the observed behavior can be qualitatively explained by considering the components of hydrostatic stress ($\sigma_H = (\sigma_{11}+\sigma_{22}+\sigma_{33})/3$). By using Eq. 5.1 we can calculate the expected stress due to the thermal mismatch between alloy and scale, σ_s = -6.48 GPa. Far from the sample edge the stress component normal to the sample surface is zero, and the two in-plane components are equal, so the hydrostatic stress is; $\sigma_H = 2/3\ \sigma_s$ or σ_H = -4.32 GPa. From Figure 40 we see the measured stress at a distance greater than about 25 micron is ~-4.1 GPa, which is consistent with the calculated value. At an edge we might expect that both of the components that are

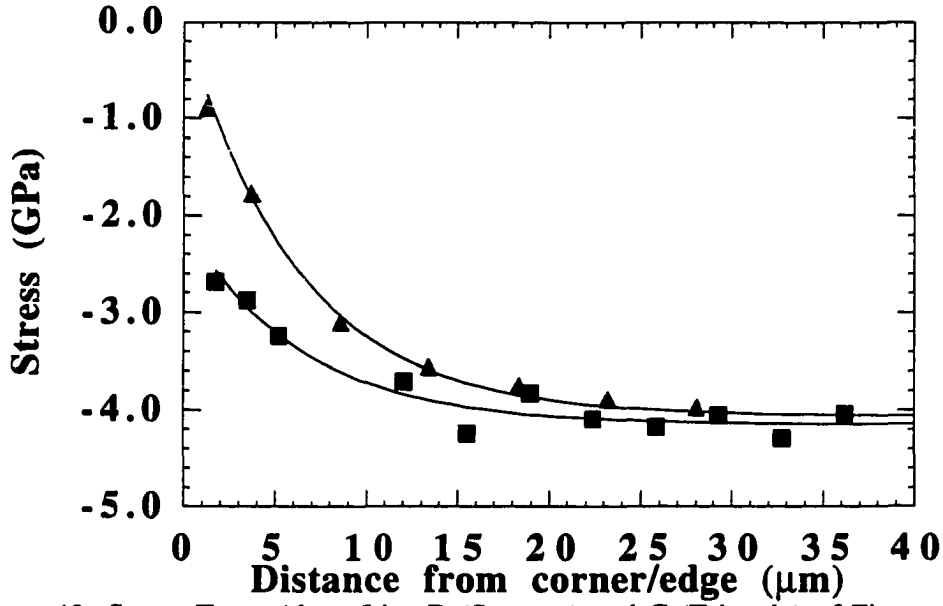

Figure 40. Stress Trace Along Line B (Squares) and C (Triangle) of Figure 39. The full line is to help guide the eye.

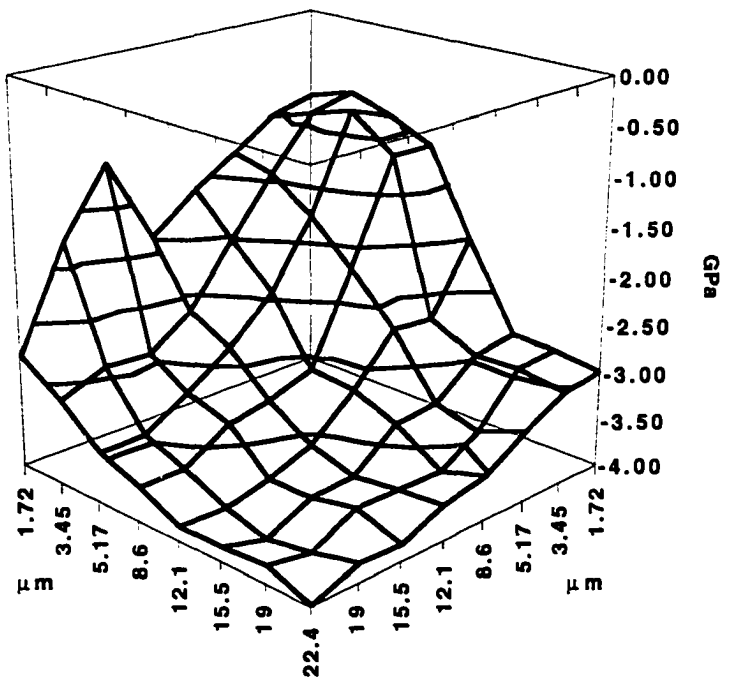

Figure 41. Three Dimensional Plot of the Stress in the Corner Region of the Sample.

perpendicular to the edge to become zero. Thus the hydrostatic stress is; $\sigma_H = 1/3\ \sigma_s$ or $\sigma_H = -2.16$ GPa. This is also consistent with the trend in Figure 40. Finally at the corner all three components of the stress ought to go to zero and consequently so should the hydrostatic stress, which is also consistent with the trend in the data in Figure 40.

Although the observed stress reduction close to the edge could be qualitatively understood as described above, all our attempts aimed at understanding the decay length failed. All our approaches at evaluating the elastic response of the scale/alloy produced decay lengths comparable to the scale thickness of ~1 μm as opposed to the measured ~10 μm.

Our surprising experimental result did however induce two theoreticians at the Idaho National Engineering and Environmental Laboratory (Richard Williamson and Julie Wright) to investigate the problem using finite element analysis (FEA). Although the author was not directly involved in the FEA calculations, they did lead to joint publications: the results are included here for the sake of completeness.

The FEA method deals with complex structures by dividing the 'structure' into smaller geometrically simple subsections (elements) for which the governing partial differential equations can be approximated by algebraic equations. A combination or assembly of the elements results in a system of algebraic equations that are readily solved on a computer. The solution typically involves an iterative procedure in which the displacements (and thus stress and strain) in each element are adjusted to satisfy the boundary conditions.

The assumptions made in modeling the residual stresses are as follows: The oxide and substrate are perfectly bonded throughout the calculation, and the specimen begins in a stress free condition at 900°C. Stresses or deformation resulting from growth of the oxide are not considered; growth stresses are thought to be small relative

to thermally generated stresses. All material properties are assumed to be homogeneous and isotropic, and were obtained from tabulations for bulk materials, as reported in reference [104]. Elastic properties are assumed to be independent of temperature [97,98], but monotonic temperature-dependent expansion coefficients [95,96] are used for both the scale and alloy. These latter assumptions are equivalent to precluding phase transformations in both the substrate and oxide. Plasticity effects were precluded for the scale; the alloy was assumed to be governed by a von Mises yield condition and isotropic hardening with temperature-dependent plastic flow curves, based on tensile curves of an Fe-28Al-2Cr alloy [105]. Cooling is assumed to be spatially uniform and relatively rapid, so time-dependent deformation (creep) is not considered. A two-dimensional computational mesh [104] was used to model the samples in generalized plane strain. The mesh has a nominal edge length of 100 μm and a uniform 0.5 μm thick oxide scale on the entire exterior. Rather than a sharp edge where two surfaces meet, a corner radius of 2 μm was used.

When the specimen is cooled from an oxidation temperature to ambient, a biaxial stress state exists in regions distant from the edges, with stress and strain values essentially equivalent to infinite plate solutions. The film is in compression and the substrate in tension because of the difference in thermal contraction of the two materials. At an edge, however, a type of bending phenomenon is observed in the film. The substrate plasticity enables it to significantly deform to accommodate stresses, and the film near the corner behaves similarly to an elastic beam in bending, with tensile stresses present along the outside of the beam and compressive stresses on the inside of the beam. The resultant stress state is the sum of this stress gradient from bending and the compression throughout the film from thermal contraction.

The average hydrostatic stress across the scale, determined as a function of distance from the edge, is compared with measured stresses in Figure 42. The symbols

correspond to averages of experimental measurements acquired along multiple traces perpendicular to the sample edge (such as line A in Figure 39). The full and dashed lines are the results of the model FEA calculations and were first volume averaged through each column of elements in the scale, consistent with the fact that the oxides are relatively transparent and the entire scale thickness is probed experimentally. The dashed line in Figure 42 stems from a calculation where only elastic deformation was allowed; since it does not reproduce the experimentally observed decay length, we conclude that it is necessary to include plastic deformation in the substrate. The full line in Figure 42 represents calculations including plastic deformation. Agreement with experiment, both the shape of the curves and the stress magnitudes, is excellent.

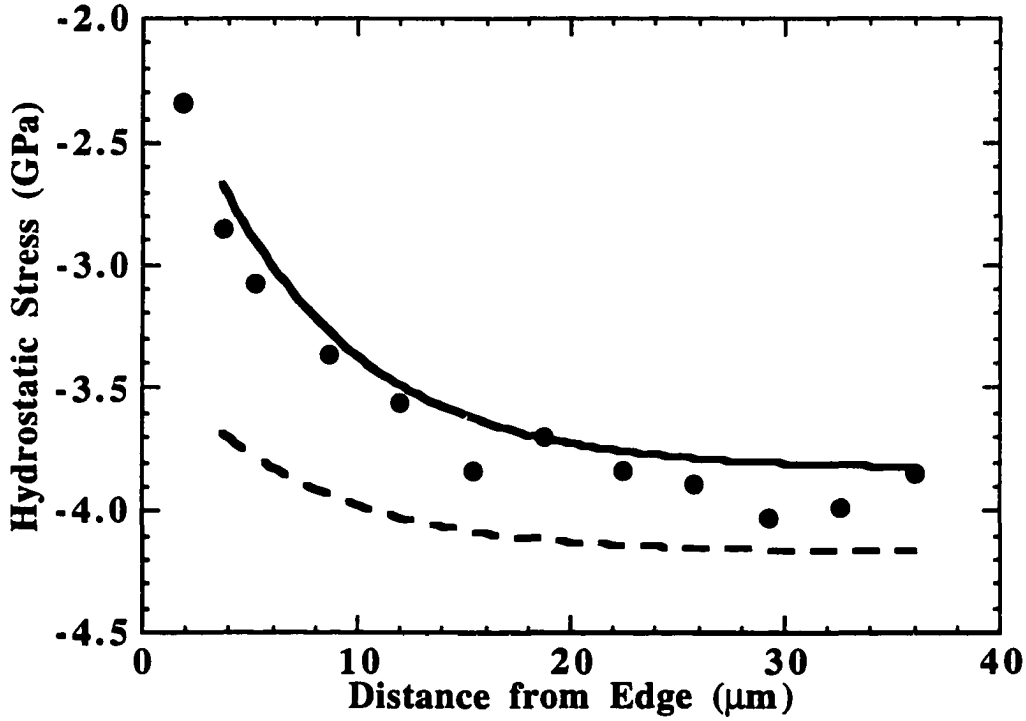

Figure 42. Stress as a Function of Distance From the Sample Edge. Circles are the experimental data collected from the sample. Lines are calculated for elastic (dashed) and including plastic (full) substrates.

The process of depth averaging and retaining only the hydrostatic stress component of the calculated results shown in Figure 42, necessary in order to compare

with experiment, does involve some loss of information. Although not discussed here, far from an edge the calculated stress gradients are relatively small and hence the averaging has little effect. Close to the edge, however, rich stress patterns, apparent in the calculations [89,104], are lost during the averaging. Local tensile stress components are calculated at the edge, so although the measured hydrostatic stress appears to be approaching zero near the edge, this cannot be taken as an indication that damage is unlikely.

The ruby fluorescence and FEA methods work well in concert. The measurements provide verification of and confidence in the model, and the model provides the detailed information necessary for improved understanding, failure prediction, and design improvements. We will proceed by comparing measured stress to FEA model predictions for a scale with a convoluted interface.

Convolutions

In a previous section, where we reported on the reactive element effect in the LBL alloys, we pointed out the reactive element free alloy exhibited a gradual stress relaxation at high temperatures as opposed to the abrupt stress relaxation seen on FA71 and MCrAl. The gradual stress relaxation of the LBL sample can be attributed to the peculiar interface morphology that has been observed after oxidation in these alloys [64,78,79,100]. A cross section showing the scale-metal interface reveals a nearly sinusoidal pattern with a wavelengths of a few microns (Figure 43 top). The reactive element free LBL alloy is the only sample investigated that demonstrates this convoluted surface morphology. In this section we will investigate the stresses in the vicinity of these convolutions using the micro-fluorescence technique.

The scales that grow during oxidation are often rough. This roughness is most often due to scale buckling, as in the case of many Cr_2O_3-forming alloys [106]. Where

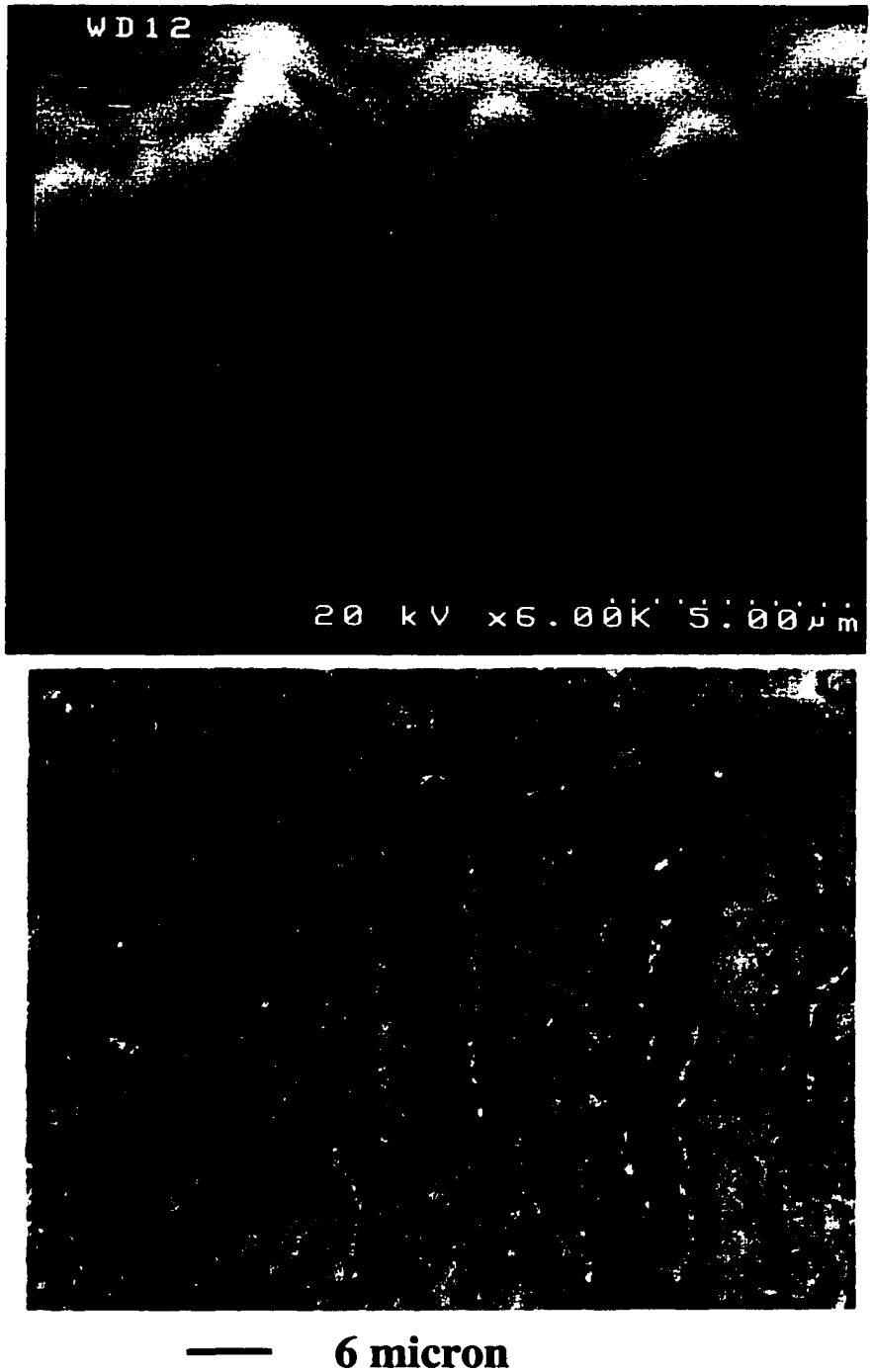

Figure 43. SEM Crossection (Top) and Optical Micrograph (Bottom) of LBL.

the scale detaches from the substrate and wrinkles under the influence of the in-plane compressive stress. In the particular samples studied here the roughening occurs without any separation from the substrate, so that the scale and the scale/alloy interface corrugate together, giving rise to a wavy interface with a fairly regular amplitude and wavelength distributions [64,78,79,100]. Our focus here was to study the stress distribution in scales with the latter morphology, i.e. the cooperative convolution of the scale and the substrate. Figure 43 is an example of such convolution. The top panel is a SEM crossection, obtained by a coworker, of an LBL alloy after a 3 hr heat treatment at 1150°C, in air, where the scale and alloy are cooperatively convoluted. The bottom panel is an optical micrograph, in reflection, of a surface of LBL after a 3 hour oxidation at 1000°C in 1 atm O_2.

A battery of experiments including ruby stress measurements were performed on the samples shown in the bottom portion of Figure 43. Peggy Hou, a collaborator from the Lawrence Berkeley Laboratory, measured an average scale thickness of 1.03±0.35 μm with an oxide grain size of less than 0.5 μm. At Berkeley the sample's topography was also characterized by means of atomic force microscopy (AFM) [64,100]. The sample was found to have large and small convolutions with average heights of 0.76±0.21 and 0.23±0.08μm, and with average base widths of 2.75 and 1.99 μm, respectively.

The fluorescence spectra were acquired using the same microscope optics that were use to measure the edge effect of the previous section. Initially spectra from several valley areas and from the tops of ridges were acquired. The measured hydrostatic stress values, are shown in Table 3. The quoted errors are twice the standard deviation divided by the square root of the number of points The values, therefore, clearly show a lower compressive σ_H along the ridges.

The hydrostatic stress computed (Eq. 5.9) for a bonded infinite plate geometry of the two materials, i.e. the theoretical hydrostatic stress of a flat scale of the same thickness is -2.19 GPa. Spectra were also recorded along a line trace across the width of three separate ridges, as shown in Figure 44. Again a reduction in stress is observed towards the top of the ridges indicating this reduction is a general and reproducible feature.

Table 3

Hydrostatic Stresses Valleys and Ridges

	σ_H (GPa)	error
valleys	-1.83	±0.04
ridges	-1.42	±0.06

A theoretical understanding of these results again relied on our Idaho National Engineering and Environmental Laboratory collaboration. Although the author was not directly involved in these calculation they are included to produce a more complete picture. The residual stresses and strains were computed during simulated cooling from a stress free condition at 1000°C to ambient temperature in specimens where the oxide and substrate were assumed to be perfectly bonded. The convolutions were assumed to have developed at the oxidation temperature (1000°C) and as a result are built into the model; the origin of the convoluted morphology was not considered, although the convolutions were free to evolve during cooling. Stresses or deformations resulting from the growth of the oxide were not considered; i.e. growth stresses were thought to be small relative to thermally generated stress. Cooling was assumed to be spatially uniform and relatively rapid, so time dependent deformation (creep) was not considered, although the substrate was permitted to deform plastically. To simplify the

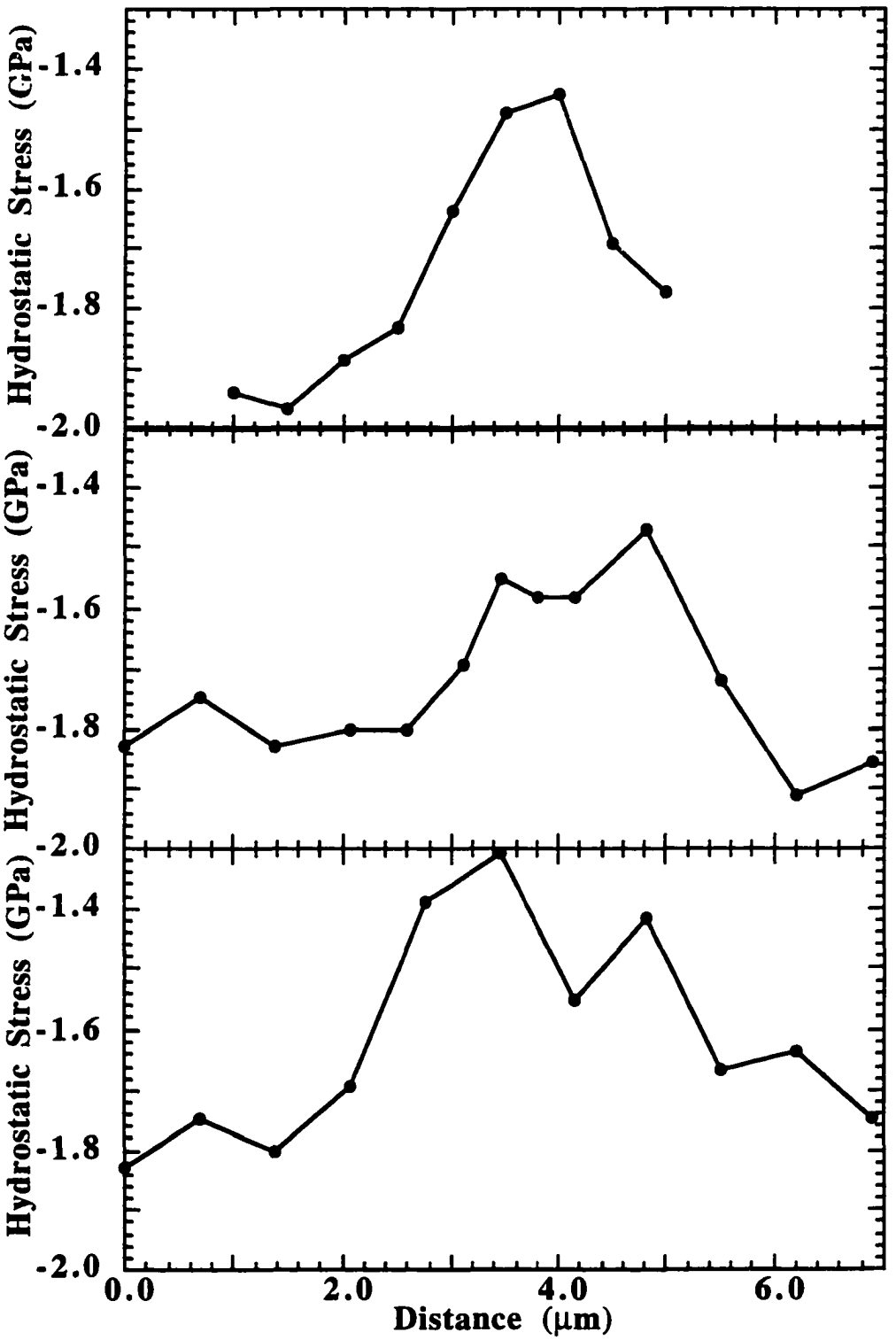

Figure 44. Stress Values Obtained From Measurement Across Various Ridges on the Sample.

complex specimen topography (Figure 43) for the purpose of modeling, the convolutions were assumed to be sinusoidal in shape. Based on the observed AFM measurements, large convolutions alternating with small convolutions were mimicked in the calculations. The same material properties were assumed here as were assumed in the previous section.

The FEA calculations generate a wealth of information (most of which is not presented here) about each of the components of scale and substrate stress [86,87]. However, the scale interface convolutions cause a type of localized bending. As the scale is placed in compression during cooling, the convolutions steepen, and the scale at each peak behaves similarly to an elastic beam in bending, with tensile stresses present along the outside of the beam and compressive stress on the inside. As a result, the residual stresses are no longer biaxial but contain significant gradients. The FEA model shows the scale stress to be analogous to that observed in a simple corrugated beam placed in compression, but is not symmetrical because of the constraint provided by the substrate.

The computed hydrostatic scale stress for the modeled geometry is compared with the measured stress in Figure 45, as a function of specimen position. The comparison was made by averaging σ_H across the volume of several columns of elements to achieve an approximate excited volume of 1 μm^3 at the peak, midpoint and valley. This volume was based on a 1 μm diameter spot though out the 1 μm scale thickness, since the oxides are relatively transparent and the entire scale thickness is probed experimentally. The agreement between the measured and volume-averaged results is very good; both the shapes of the curves and the stress magnitude are similar. Any offset between the model curve and the experiment data may be due to growth stresses that are not included in the model. Furthermore, the model geometry was

based on an average wavelength and amplitude of convolutions from which a given convolution could easily vary by 20%.

Once again the ruby fluorescence measurements provide verification of and confidence in the FEA modeling. This section, as well as the previous one, demonstrate that the ruby fluorescence stress measurements technique is readily applicable to micro-structural investigation.

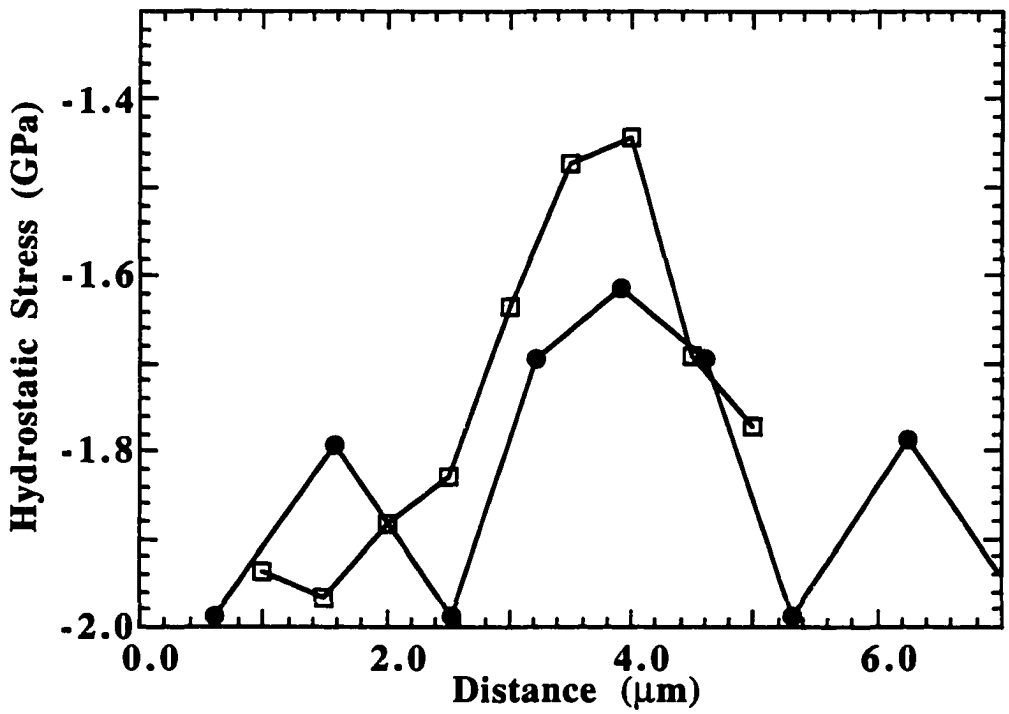

Figure 45. Comparison of Measured (Open Squares) and Modeled Stress (Full Circles).

Summary and Conclusions

This initial survey of the applicability of ruby piezospectroscopy to thermally grown oxide scales has demonstrated that the technique is a very powerful tool. Because of the short acquisition times, the lack of any sample preparation and the non-destructive nature of the technique, it is clear that, if the technique were applied to a

newly invented high temperature alumina forming alloy it would clearly provide a large amount of information about the principal cause of scale failure: viz scale stress. By using both modes of operation, namely macro and micro fluorescence, we have provided insight into the thermal-mechanical behavior of alumina containing scales.

The ruby spectrum is useful as a fingerprint for determining the presence of α-Al_2O_3. By carefully monitoring the fluorescence signal strength we have demonstrated that the addition of a reactive element to an alloy slows the formation of α-alumina.

We observed that, if an alumina forming alloy contains a reactive element (e.g. Hf, Zr or Y), the scales can support significantly larger compressive stress. Ruby strain measurements were verified by comparison to x-ray strain measurements .

It was demonstrated that the ruby fluorescence stress measurement technique is readily applicable to micro structural investigation. By using microscope optics, the stress behavior in the vicinity of sample edges, corners and scale/alloy cooperative convolutions were investigated.

The ruby fluorescence and FEA methods work well in concert. The measurements provide verification of, and confidence in, the model. The model provides the detailed information necessary for improved understanding, failure prediction, and design improvements.

CHAPTER VI

CONCLUDING REMARKS

Summary

For the purpose of evaluating Raman scattering and ruby fluorescence as tools for investigating metallic corrosion, it was decided to perform our investigations on alloys which had been extensively investigated by other techniques. This approach has enabled us not only to ascertain the validity of our findings but has also allowed us to compare the difficulties, drawbacks, limitations of the techniques which often provide the similar information on the oxidation process.

The work reported in Chapter IV of this thesis has shown that Raman scattering is indeed a useful tool for oxide scale characterization. Because each oxide possesses a well defined vibrational spectrum related to the interatomic bonding and masses of the constituent atoms, it has been possible using Raman spectroscopy, to follow the evolution of the chemical composition of the scale as a function of oxidation treatment. In this respect, while the detection of Cr_2O_3 in mature scales on FeCrNi alloys came as no surprise, the transient evolution of Fe oxide contains information which had not clearly been previously observed. In a similar vein the role of the reactive element was predicted to accelerate the formation of the mature scale phases (i.e. Cr_2O_3 and α-Al_2O_3) [13]. It was surprising to find that for the FeCrNi alloys the reactive element had little effect on the transient scale evolution (Chapter IV) and that for the FeCrAl alloys it slows the formation of α-Al_2O_3 (result supported by Chapter V and Appendix B).

Raman scattering has therefore turned out to be quite a powerful tool for investigating oxidation. There is almost no sample preparation necessary, the acquisition times are relatively short (~8 min.), and the technique is also non-destructive. We anticipate that the technique will be particularly useful for the investigation of new alloys where the oxides in the scale are difficult to predict.

The use of ruby fluorescence as a built-in stress gauge in the alumina scales has provided us with information not previously available. Although the importance of stresses had long since been identified as a crucial ingredient in scale failure, no convenient technique was available to provide it experimentally. Although conceptually x-rays were capable of yielding this information the necessity for large flat surfaces and thick scales make this technique applicable in only a few instances. The ruby fluorescence is much more sensitive and can be used on small samples.

The fluorescence stress gauge identified the reactive element effect as not due to a reduction in stress, contrary to what was predicted [13]. Consequently, new theories about the effect that the reactive element has on scale stress will have to include the results of this thesis. The stress information obtained by the micro-fluorescence can not be obtained by any other technique. The results reported in Chapter V on the edge effect and convoluted interfaces have provided confidence in the scale stress models produced by finite element analysis. The relaxation of the scale stress which extends more than twenty times the scale thickness, as the edge is approached, was not predicted prior to this work. It was predicted that scales with convoluted interface would have higher compressive stress in the valleys than on the ridges [100] which is now confirmed. The ruby piezospectroscopic techniques is clearly a powerful tool for the study of corrosion, and the results it provides has improved on our understanding of scale stress.

Directions

In principle, because Raman peak positions are sensitive to stress, they can also conceptually be used as a stress gauge. However because the position of the Raman lines are also sensitive to stoichiometric effects, the interpretation of the line shifts can be very complicated. A careful evaluation of the stoichiometric and compressional dependence will have to be undertaken before Raman spectroscopy can be used as a reliable tool for the measurement of scale stress.

There are fluorescences other then ruby that may be useful as stress gauges. Cr doped κ-Al_2O_3 fluoresces and we are currently developing it into a tool for the measurement of scale stress. Similarly the fluorescence produced by MgO doped with Cr is under development as well.

Most characterization techniques suffer from the drawback that the samples are not investigated at the oxidation temperature, but experience cooling to room temperature prior to measurement. The cooling of the sample can produce a strain in the scale that can in turn produce a pressure driven phase change. Based on the work in this thesis, which has shown Raman scattering to be a powerful technique for scale characterization, a new project has been started at Argonne National Laboratory to build a UV laser spectroscopy system. By using UV radiation it is possible to eliminate the large black body radiation background which is observed at higher temperature when using visible light [107]. This will prove to be one of the few techniques that is capable of in-situ high temperature characterization of scales.

The alloys investigated in this thesis have been polycrystalline. A new graduate student at our laboratory has started to use Raman fingerprinting and ruby piezospectroscopy to investigate the corrosion of single crystal alloys. This study

should improve our understanding of the effects that either alloy grain boundaries or alloy orientation have on the scale phases and scale stresses.

The Energy Technology Division of Argonne National Laboratory is currently investigating alloy ceramic composite systems used for turbine engine components. The particular system are structural alloys coated with a corrosion resistant alloy (MCrAlY Chapters IV and V). These in turn are coated with a thermal resistance ceramic (ZrO_2). These three layer systems are prone to failure due to corrosive attack. Raman spectroscopy and ruby piezospectroscopy, after a slow start, are becoming major techniques used in the investigation of these systems [108].

REFERENCES

[1] D. A. Jones, *Principles and Preventions of Corrosion,* (Prentice Hall, New Jersey) p 3 (1992)

[2] Mary L. Duchi, *Economic Effects Of Metallic Corrosion in the United States,* Battelle Report to Specialty Steel Industry of North America (April 1995)

[3] Leo Kay in the Press Office, Press Release, *United States Environmental Protection Agency,* Release# 98-3-20, (March 23, 1998)

[4] Louis Sass, Press Release, *United States Environmental Protection Agency,* Release# 98-OPA197, (July 6, 1998)

[5] D. A. Jones, *Principles and Preventions of Corrosion,* (Prentice Hall, New Jersey) p 4 (1992)

[6] G. W. Meetham, *The Development of the Gas Turbine Materials,* (Halsted Press Division John Wiley & Sons, New York) p V, (1981)

[7] G. W. Meetham, *The Development of the Gas Turbine Materials,* (Halsted Press Division John Wiley & Sons, New York) p 20, (1981)

[8] K. R. Trethwey, J. Chamberlain, *Corrosion for Students of Science and Engineering,* (Langman Scientific & Technical with John Wiley & Sons, New York) p 337 (1988)

[9] P. Kofsted, *High-Temperature Oxidation of metals,* (John Wiley & Sons, New York) p 1 (1966)

[10] H. Hindam, D. P. Whittle, *Oxidation of Metals,* **18**, p 245 (1982)

[11] D. A. Jones, *Principles and Preventions of Corrosion,* (Prentice Hall, New Jersey) p 419 (1992)

[12] K. Natesan, C. Richier, B. W. Veal, M. Grimsditch, D. Renusch and A. P. Paulikas, *Argonne National Laboratory Report,* ANL/FE-95/02 (1995)

[13] J. Jedlinski, *Solid State Phenomena,* **21&22**, p 335 (1992)

[14] N. W. Ashcroft, N. D. Mermin, *Solid State Physics,* (Horcourt Brace College Publishers, Fort Worth) p 102 (1976)

[15] J. B. Bindell in *Encyclopedia of Materials Characterization,* ed. C. R. Brundle, C. A. Evans, S. Wilson, L. E. Fitzpatrick (Butterworth - Heinemann, Boston) p 71 (1992)

[16] K. E. Sickafus in *Encyclopedia of Materials Characterization*, ed. C. R. Brundle, C. A. Evans, S. Wilson, L. E. Fitzpatrick (Butterworth - Heinemann, Boston) p 99 (1992)

[17] K. E. Sickafus in *Encyclopedia of Materials Characterization*, ed. C. R. Brundle, C. A. Evans, S. Wilson, L. E. Fitzpatrick (Butterworth - Heinemann, Boston) p 100 (1992)

[18] J. C. Yang, M. Yeadon, B. Kolasa, J. M. Gibson, 193th ECS spring meeting, San Diego, CA., (1998) Vol 98-9 *High Temperature Corrosion and Materials Chemistry*, ed by P. Y. Hou, M. J. McNallan, R. Oltra, E. J. Opila, and D. A. Shores, Electrochem. Soc., Pennington, NJ (1998), p 126

[19] K. E. Sickafus in *Encyclopedia of Materials Characterization*, ed.by C. R. Brundle, C. A. Evans, S. Wilson, L. E. Fitzpatrick (Butterworth - Heinemann, Boston) p 113 (1992)

[20] R. L. Farrow, A. S. Nagelberg, *Applied Physics Letters* **36**, p 945, (1980)

[21] R. L. Farrow,P. L. Mattern, A. S. Nagelberg, *Applied Physics Letters*, **36**, p 212, (1980)

[22] N. Boucherit, A. Hugot-Le Goff, S. Joiret, *Thin Solid Films*, **174**, p 111, (1989)

[23] D. J. Gardiner, C. J. Littleton, K. M. Thomas, K. N. Strafford, *Oxidation of Metals*, **27**,p 57, (1987)

[24] J. Birnie, C. Craggs, D. J. Gardiner and P. R. Graves, *Corrosion Science*,**33**, p 1, (1992).

[25] H. E. Evans, A. M. Huntz, *Materials at High Temperatures*, **12**, p 111 (1994)

[26] D. J. Gardiner in *Microscopy of Oxidation-2* eds. S. B. Newcomb and M. G. Bennet. (The Institute of Materials, London) p 36 (1993)

[27] M. J. Bennett, *Surface and Interface Analysis*, **22**, p 421, (1994)

[28] W. A. England, M. J. Bennett, D. A. Greenhalgh, S. N. Jenny, C. F. Knights, *Corrosion Science*, **26**, No 7, p 537 (1986)

[29] M. J. Bennett, P. R. Graves, R. W. M. Hawes, in *High Temperature Alloys, Their Exploitable Potential*, J. B. Marriott, M. Merz, J. Nihoul, J. Ward, (Elsevier Applied Science, London and New York, 1987) p 205 (1987)

[30] M. J. Graham, R. J. Hussey, *Oxidation of Metals*, **44**, p 339 (1995)

[31] R. L. Farrow, R. E. Benner, A. S. Nagelberg, P. L. Mattern, *Thin Solid Films*, **73**, p 33 (1980)

[32] K. Natesan, B. W. Veal, M. Grimsditch, D. Renusch and A. P. Paulikas, Proc. *Ninth Annual Conference on Fossil Energy Materials*, Oak Ridge, TN, CONF-9505204, ORNL/FMP-95/1, p 225 (1995)

[33] D. Renusch, M. Grimsditch, I. Koshelev, B. W. Veal, *Oxidation of Metals*, **46**, p 365 (1996)

[34] D. Renusch, B. W. Veal, K. Natesan, I. Koshelev, M. Grimsditch, 190th ECS fall meeting, San Antonio, TX., (1996) Vol 96-26 Fundamentals of High Temperature Corrosion, ed by D. A. Shores, R. Rapp and P. Y. Hou, Electrochem. Soc., Pennington, NJ, p 62 (1997)

[35] D. Renusch, M. Grimsditch, I. Koshelev, B. W. Veal, *Oxidation of Metals*, **48**, p.471 (1997)

[36] D. Renusch, M. Grimsditch, A. P. Paulikas, B. W. Veal, 193th ECS spring meeting, San Diego, CA., (1998) Vol 98-9 *High Temperature Corrosion and Materials Chemistry*, ed by P. Y. Hou, M. J. McNallan, R. Oltra, E. J. Opila, and D. A. Shores, Electrochem. Soc., Pennington, NJ, p 76 (1998)

[37] B. W. Veal, D. Renusch, I. Koshelev, A. P. Paulikas, S. Uran, M. Grimsditch, P. Y Hou, 193th ECS spring meeting, San Diego, CA., (1998) Vol 98-9 *High Temperature Corrosion and Materials Chemistry*, ed by P. Y. Hou, M. J. McNallan, R. Oltra, E. J. Opila, and D. A. Shores, Electrochem. Soc., Pennington, NJ, p 65 (1998)

[38] N. W. Ashcroft, N. D. Mermin, *Solid State Physics*, (Horcourt Brace College Publishers, Fort Worth) p 437 (1976)

[39] N. B. Colthup, S. E. Wiberley, L. H. Daly. *Introduction to Infrared and Raman Spectroscopy*, 2 ed. (Academic Press, New York) p59 (1975)

[40] J. R. Ferraro, K. Nakamoto, *Introduction to Raman Spectroscopy*, (Academic Press, Boston) p 13 (1994)

[41] J. B. Marion, M. A. Heald, *Classical Electromagnetic Radiation*, 2ed. (Harcourt Brace Jovanovich, Publishers, San Diego) p 231 (1980)

[42] N. W. Ashcroft, N. D. Mermin, *Solid State Physics*, (Horcourt Brace College Publishers, Fort Worth) p 481 - 486 (1976)

[43] N. B. Colthup, S. E. Wiberley, L. H. Daly. *Introduction to Infrared and Raman Spectroscopy*, 2 ed. (Academic Press, New York) p62 (1975)

[44] B. D. Bartolo, *Optical Interactions in Solids*, (John Wiley, New York) p 193 - 219 (1968)

[45] G. F. Imbusch in *Luminescence of Inorganic Solids*, ed.by B. D. Bartolo (Plenum Press, New York), p 115 - 130 (1977)

[46] Q. Ma, D. R. Clarke, *Journal American Ceramin Society*, **76**, p 1433 (1993)

[47] J. He, D. R. Clarke, *Journal American Ceramin Society*,**78**, p 1347 (1995)

[48] A. Jayaraman, *Review of Modern Physics*, **55**, p 65 (1983)

[49] Instruments SA, Inc. *T64000 The Ultimate Raman Spectrograpk.* (Instruments SA, Inc, New Jersey) p 6 (1995)

[50] R. W. G. Wyckoff, *Crystal Structures*, (Interscience Publishers, New York) 2ed. Ed., Vol. **2**, p 6 (1964)

[51] R. W. G. Wyckoff, *Crystal Structures*, (Interscience Publishers, New York) 2ed. Ed., Vol. **3**, p 79 (1965)

[52] R. J. Thibeau, C. W. Brown and R. H. Heidersbach, *Applied Spectroscopy*, **32**, p 32 (1978)

[53] R. W. G. Wyckoff, *Crystal Structures*, (Interscience Publishers, New York) 2ed. Ed., Vol. **1**, p 85 (1963)

[54] M. J. Massey, N. H. Chen, J. W. Allen, R. Merlin, *Physical Review B*, **41**, p 8776 (1990).

[55] *CRC Handbook of Chemistry and Physics*, edit by R. C. Weast, M. J. Astle, (CRC Press, Inc., Boca Raton Florida), 61st Edition, p B-5 (1980)

[56] O. Kubaschewski, *Iron-Binary Phase Diagrams*, (Springer-Verlag, New York) p 79 (1992)

[57] F. F. Bentley, L. D. Smithson, A. L. Rozek, *Infrared Spectra and Characteristic Frequencies ~700-300 cm-1*, (Interscience Publishers, New York) p 1540 (1968)

[58] R. E. Dientz, G. I. Parisot, A. E. Meixner, *Physical Review B*, **4**, p 2302 (1971).

[59] J. S. Arlow, D. F. Mitchell, M. J. Graham, *Journal. of Vacuum Science and Technolgy*, **5**, No. 4, p 572 (1987)

[60] K. F. McCarty, D. R. Boehme, *Journal of Solid State Chemistry* , **79**, p 19 (1989)

[61] M. I. Baraton, G. Busca, M. C. Prieto, G. Ricchirdi, V. S. Escribano, *Journal of Solid State Chemistry*, **112**, p 9 (1994)

[62] R. Prescott and M. J. Graham, *Oxidation of Metals*, **38**, p 233, (1992)

[63] D. M. Lipkin, H. Schaffer, F. Adar, D. R. Clarke, *Applied Physics Letters*, **70**, No. 19, 2550 (1997)

[64] P. Y. Hou, R. M. Cannon, H. Zhang, R. L. Williamson, 190th ECS fall meeting, San Antonio, TX, Vol 96-26 *Fundamentals of High Temperature*

Corrosion, ed by D. A. Shores, R. Rapp and P. Y. Hou, Electrochem. Soc., Pennington, NJ, p 28 (1997)

[65] G. C. Bye, G. T. Simpkin, *Journal American Ceramin Society*,.**57**, p 367 (1974).

[66] C. J. P. Steiner, D. P. H. Hasselman, R. M. Spriggs, *Journal American Ceramin Society*, **54**, p 412 (1971).

[67] M. Ozawa, M. Kimura, A. Isogai, *Journal Materials Science Letters*, **9**, p 709 (1990)

[68] J. R. Wynnyckyj, C. G. Morris, *Metallurgical Transactions B*, Vol. **16B**, p 345 (1985)

[69] C. Loung, J. W. Richardson, M. Ozawa, *Journal Alloys and Componds*, **250**, p 356 (1997) Proc. 21th Rare Earth Conference, Duluth, MN

[70] P. R. Graves, C. Johnston, J, J, Campaniello, *Materials Research Bulletin*, **23**, p 1651 (1988)

[71] K. Natesan, K. L. Klug, D. Renusch, M. Grimsditch and B. W. Veal, Tenth Annual Conference on Fossil Energy Materials, Knoxville TN, May 14-16, (1996)

[72] D. Renusch, B. W. Veal, I. Koshelev, K. Natesan, M. Grimsditch and P. Y. Hou, *Fundamental Aspects of High Temperature Corrosion*, ed by D. A. Shores, R. Rapp and P. Y. Hou, (Electrochem. Soc., Pennington) Vol **96-26** p 62 (1997)

[73] D. M. Lipkin, D. R. Clarke, M. Hollatz, M. Bobeth, W. Pompe, *Corrosion Science*, **39**, p 231, (1997)

[74] V. K. Tolpygo, J. R. Dryden, D. R. Clarke, *Acta Materialia*, **46**, p 927 (1998)

[75] C. Mennicke, E. Schumann, C. Ulrich and M. Ruhle, (presented at the 4th Int. Symp. on *High Temp. Corrosion and Protection of Mat.*, Les Embiez, France, May 20-24, 1996) *Materials Science Forum* , **251-254**, p 251 (1997)

[76] D. M. Lipkin and D. R. Clarke, *Oxidation of Metals* , **45**, p 267 (1996)

[77] R. J. Christennsen, D. M. Lipkin, D. R. Clarke, *Acta Materialia*, **44**, p 3813 (1996)

[78] V. K. Tolpygo, D. R. Clarke, *Acta Metall. Materialia*, **46**, p 14 (1998)

[79] Xiao-Yan Gong, D. R. Clarke, *Oxidation of Metals*, **50**, p 355 (1998)

[80] Q. Wen, D. R. Clarke, N. Yu and M,. Nastasi, *Applied Physics Letters*, **66**, p 293 (1995)

[81] Qing Ma and D. R. Clarke, *Journal American Ceramin Society*, **77**,p 298 (1994)

[82] Qing Ma, and D. R. Clarke, *Acta Metall. Materialia*, **41**, No. 6, 1811 (1993)

[83] Qing Ma, W. Pompe, J. D. French, D. R. Clarke, *Acta Metall. Materialia*, **42**, No. 5, 1673 (1994)

[84] S. E. Molis and D. R. Clarke, *Journal American Ceramin Society*, **73**,p 3189 (1990)

[85] Qing Ma and D. R. Clarke, *The American Society of Mechanical Eneineers*, AMD-Vol **181**, Book No. H00888 - 1993

[86] J. K. Wright, R. L. Williamson, P. Y. Hou, R. M. Cannon, D. Renusch, M. Grimsditch, B. W. Veal 193th ECS spring meeting, San Diego, CA., (1998) Vol 98-9 *High Temperature Corrosion and Materials Chemistry*, ed by P. Y. Hou, M. J. McNallan, R. Oltra, E. J. Opila, D. A. Shores, (Electrochem. Soc.,Pennington) p. 53 (1998)

[87] J. K. Wright, R. L. Williamson, D. Renusch, M. Grimsditch, B. W. Veal, P. Y. Hou, R. M. Cannon, *Materials Science and Enginerring*, **A262**, p 246 (1998)

[88] M. Grimsditch, D. Renusch, B. W. Veal, J. K. Wright, R. L. Williamson, 193th ECS spring meeting, San Diego, CA., (1998) Vol 98-9 *High Temperature Corrosion and Materials Chemistry*, ed by P. Y. Hou, M. J. McNallan, R. Oltra, E. J. Opila, and D. A. Shores, (Electrochem. Soc., Pennington) p 32 (1998)

[89] D. Renusch, Murali, S. Uran, M. Grimsditch, B. W. Veal, J. K. Wright, R. L. Williamson -- (accepted by *Oxidation of Metals*-1999)

[90] A. A. Kaplyanskii, A. K. Przhevuskii and R. B. Rozenbaum, *Soviet Physics, Solid State* **10**, p 1864 (1969).

[91] I. Koshelev, A. P. Paulikas, B. W. Veal, *Oxidation of Metals*, **51**,p 23, (1999)

[92] B. W. Veal, D. Renusch, I. Koshelev, A. P. Paulikas, S. Uran, M. Grimsditch, P. Y Hou, 193th ECS spring meeting, San Diego, CA., (1998) *High Temperature Corrosion and Materials Chemistry*, ed by P. Y. Hou, M. J. McNallan, R. Oltra, E. J. Opila, and D. A. Shores, (Electrochem. Soc., Pennington) Vol **98-9** p 65 (1998)

[93] T. Yada and H. Koguchi, *JSME Int. J.*, **34** (2) p 163 (1991)

[94] J. J. Barns, J. G. Goedjen, D. A. Shores, *Oxidation of Metals*, **32**,p 449 (1989)

[95] W. D. Porter, P. J. Maziasz, *Scripta Metallurgica* , **29**, p 1043 (1993)

[96] Y. S. Touloukian, P. K. Kirby, R. E. Taylor, T. Y. Lee, *Thermophysical Properities of Matter: Thermal Expansion in Nonmetallic Solids*, (Plenum, New York), Vol. **13** (1977)

[97] W. J. Lackey, D. P. Stinton, G. A. Carney, L. L. Fehrenbacher, A. C. Schaffhauser, Oake Ridge National Laboratory Report, ORNL/TM-8949

[98] P. Morgand, P. Mouturat, G. Sainfort, *Acta Metallurgica*, **16**, 867, (1968)

[99] A. Goldsmith, T. E. Watermand, H. J. Hirschborn, *Handbook of Thermalophyisical Properties of Solids Materials*, (Pargamon Press, New York), Vol **2** , Alloys (1962)

[100] P.Y. Hou and J. Stringer, *Journal de Physique IV*, Colloque C9, supplement to *Journal de Physique III*, **3**, p. 231 (1993)

[101] K. L. Luthra, C. L. Briant, *Oxidation of Metals* , **26**, 397 (1986)

[102] Landolt and Bornstein, *Numerical Data and Functional Relationships in Science and Technology*, (Springer, New York), New Series, Group III, Vol. **11**, p. 50 (1979)

[103] R. L. Williamson, J. K. Wright and R. M. Cannon, 190th ECS fall meeting, Oct. 6-11, 1996, San Antonio, TX. *Fundamentals of High Temperature Corrosion VI*, ed by D. A. Shores and P. Y. Hou, (Electrochem. Soc., Pennington) Vol **96-26** p 62 (1997)

[104] J. K. Wright, R. L. Williamson and R. M. Cannon, Materials Science and Enginerring **A238** 411 (1997)

[105] J. R. Knibloe, R. N. Wright, V. K. Sikka, R. H. Baldwin, C. R. Howell, Materials Science and Engineering **A153** p. 282 (1992)

[106] P. Kofstad, *High Temperature Corrosion*, (Elsevier Applied Science, New York, 1998)

[107] E. Zouboulis, D. Renusch, M. Grimsditch, *Journal of Applied Physics Litters*, **72** (1) p 1 (1998)

[108] J. P. Singh, B. Nair, D. Renusch, M. Sutaria, and M. Grimsditch, 23rd Annual Cocoa Beach Conference on *Engineering Ceramics and Structures*, American Ceramic Society, Cocoa Beach, FL, Jan. 25, (1999)

Appendix A

Catalog of Oxide Spectra

In chapter four we describe a technique for identifying oxide scale phases by using Raman spectroscopy (fingerprinting). The technique involves the comparison of Raman spectra acquired from oxide scale to Raman spectra acquired from pure oxides (fingerprints). In chapter IV a few spectra acquired from standard samples were presented for illustrative purposes. Here we present several additional spectra of oxides that may be found in scales. Most of the spectra we acquired from as received pure oxides perched from chemical supply companies.

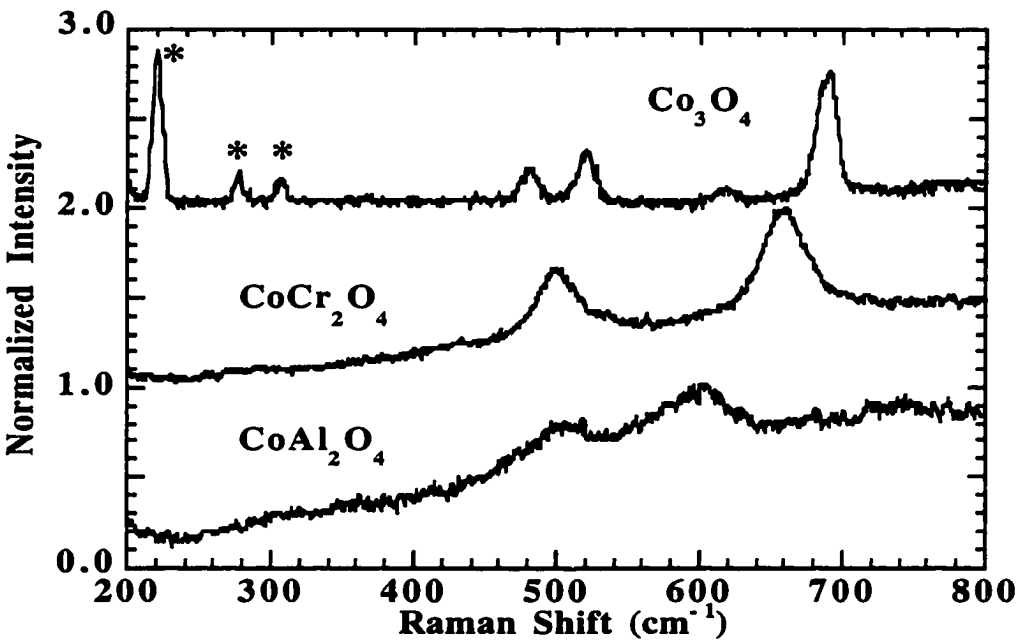

Figure 46. Raman spectra from Pure, Co_3O_4, $CoCr_2O_4$ and $CoAl_2O_4$. The * indicates plasma lines from the Kr laser.

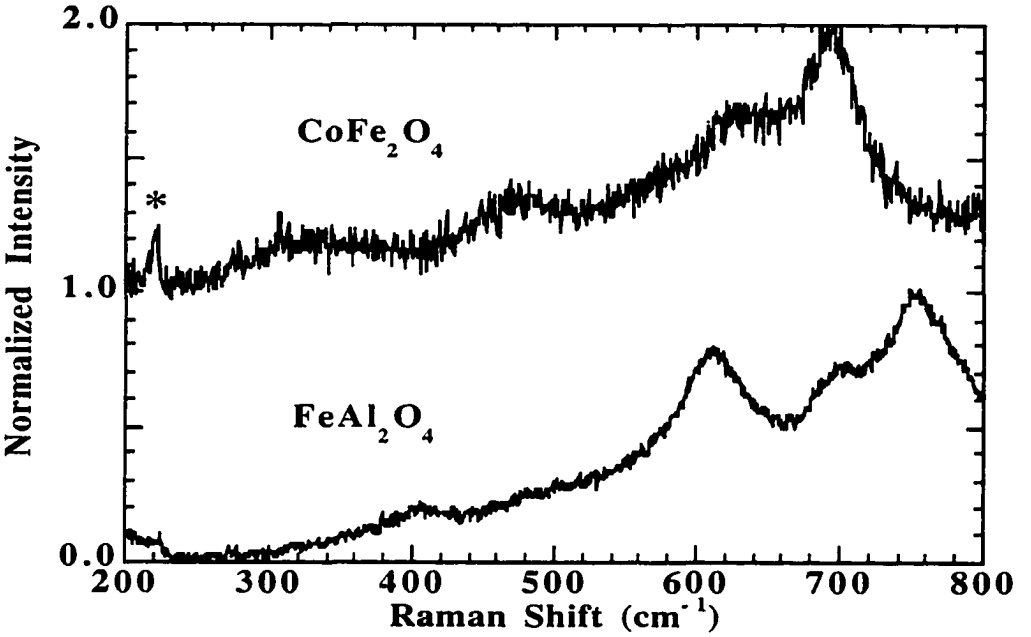

Figure 47. Raman Spectra From Pure CoFe2O4 And FeAl2O4. The * indicates plasma lines from the Kr laser.

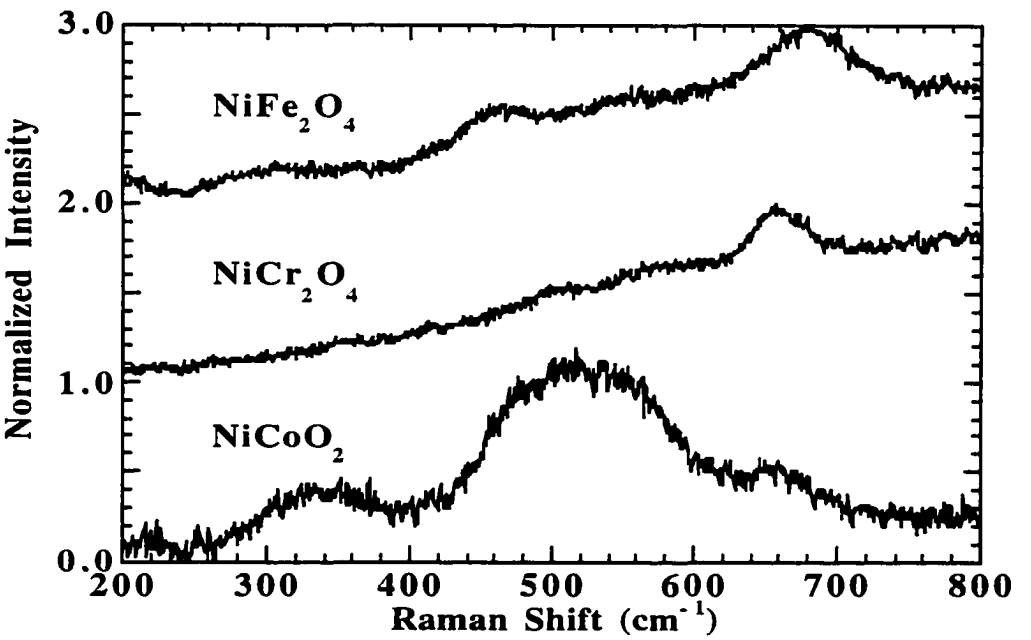

Figure 48. Raman spectra from Pure, NiFe2O4, NiCr2O4 and NiCo2O4.

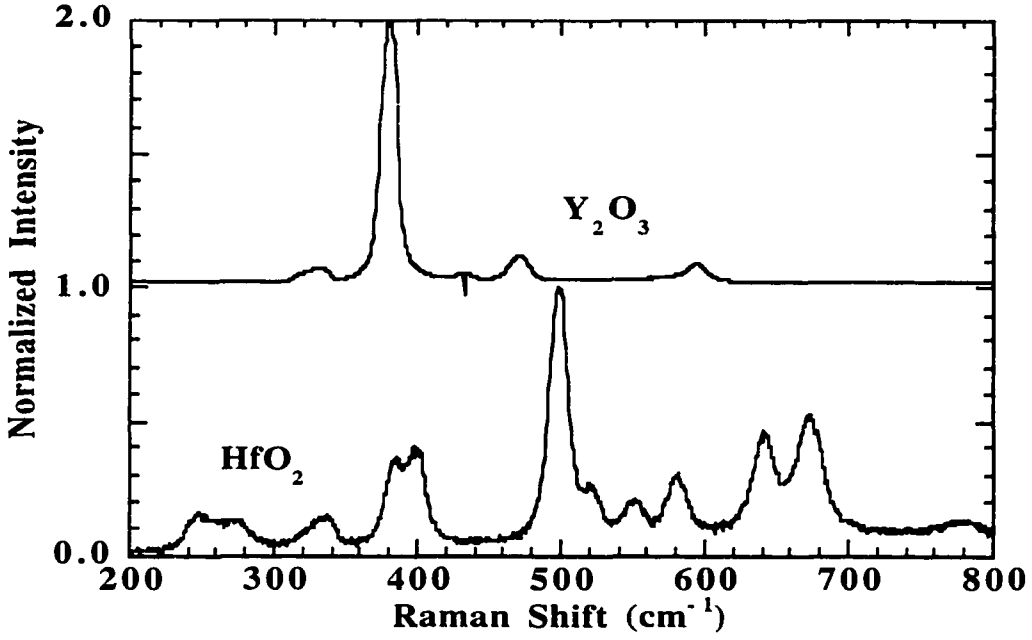

Figure 49. Raman Spectra From Pure, Y_2O_3 and HfO_2.

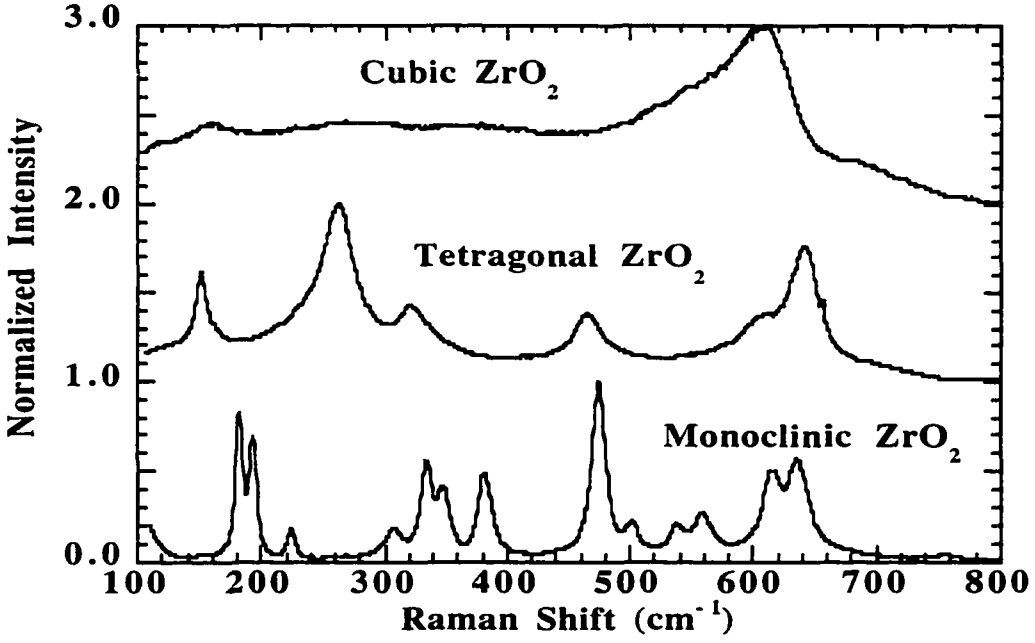

Figure 50. Raman Spectra From Cubic, Tetragonal and Monoclinic ZrO_2.

Appendix B

Phase Transformation of ZrO_2 Modified Alumina

In an effort to understand how the α-phase of Al_2O_3 is generated in scales, we have investigated the temperature induced γ to α transition in alumina. This transition is reported to occur via an intermediate phase (κ or θ [65-69]). It has also been reported that the metastable intermediate phase can be partially stabilized by doping the alumina with rare earth elements [65-69]. Because such elements are used as reactive elements in high temperature alloys, we suspect a partial stabilization effect may occur in scales. As presented in chapters four and five, the Raman and fluorescence data acquired from the thermally grown scales that form on rare earth free samples have stronger α-alumina signals, which is indicative of a larger volume fraction of α-Al_2O_3.

Starting with reagent grade γ-Al_2O_3, a sample of the as received powder, as well as a sample mixed with 1 wt% ZrO_2, was pressed at ~5000 psi, into a pellet ~1 cm diameter and ~0.5 cm tall. The pellet was sequentially heat treated from 600 °C to 1200 °C in steps of either 50 °C or 100 °C, for one hour at each temperature. Raman scattering, ruby fluorescence and X-ray powder diffraction (XRD) measurements were performed at room temperature between each treatment. The Raman spectra for the undoped and doped pellets are presented in figures 51 and 52, respectively.

At temperatures below 800 °C the X-ray data confirm that the sample is γ-Al_2O_3, however the Raman spectra are almost featureless, save a broad fluorescence background and a weak peak at ~520 cm^{-1}. For temperatures between 900 °C and 1150 °C, for the undoped sample (900°C to 1200°C doped sample), the Raman spectra contain peaks that are clearly not attributable to either γ- or α-Al_2O_3, so they must originate from an intermediate transient phase. The positions of the non-α peaks are ~255 cm^{-1}, ~335 cm^{-1}, ~620 cm^{-1}, ~710 cm^{-1}, ~780 cm^{-1}. The Raman spectra for the doped alumina, in figure 51, also contain peaks attributed to ZrO_2. This transient phase, as shown below, is identified as κ-Al_2O_3 by XRD. Figures 53 and 54 contain

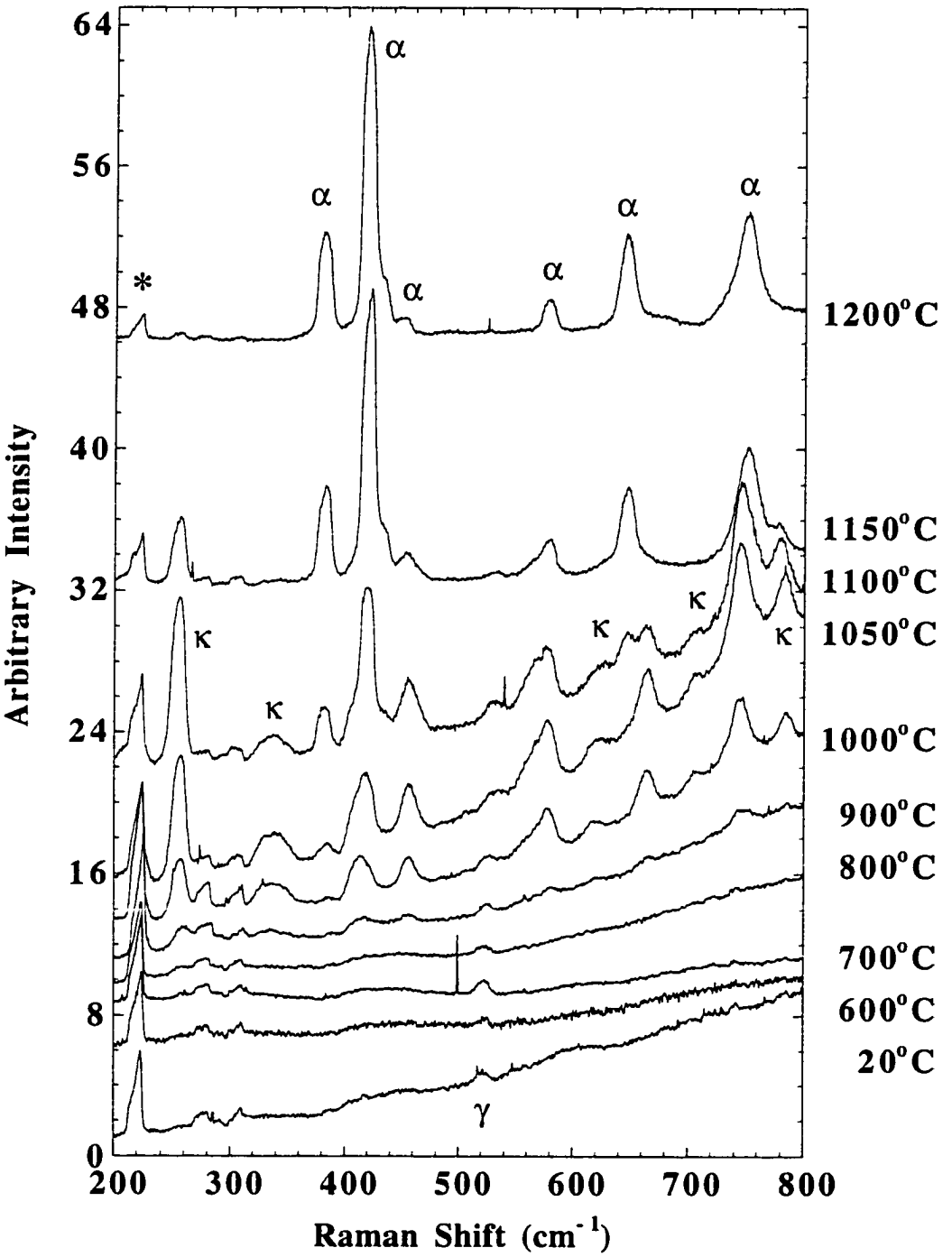

Figure 51. Raman Spectra From Undoped Al_2O_3. Powder heat treated at indicated temperatures for 1 hr.

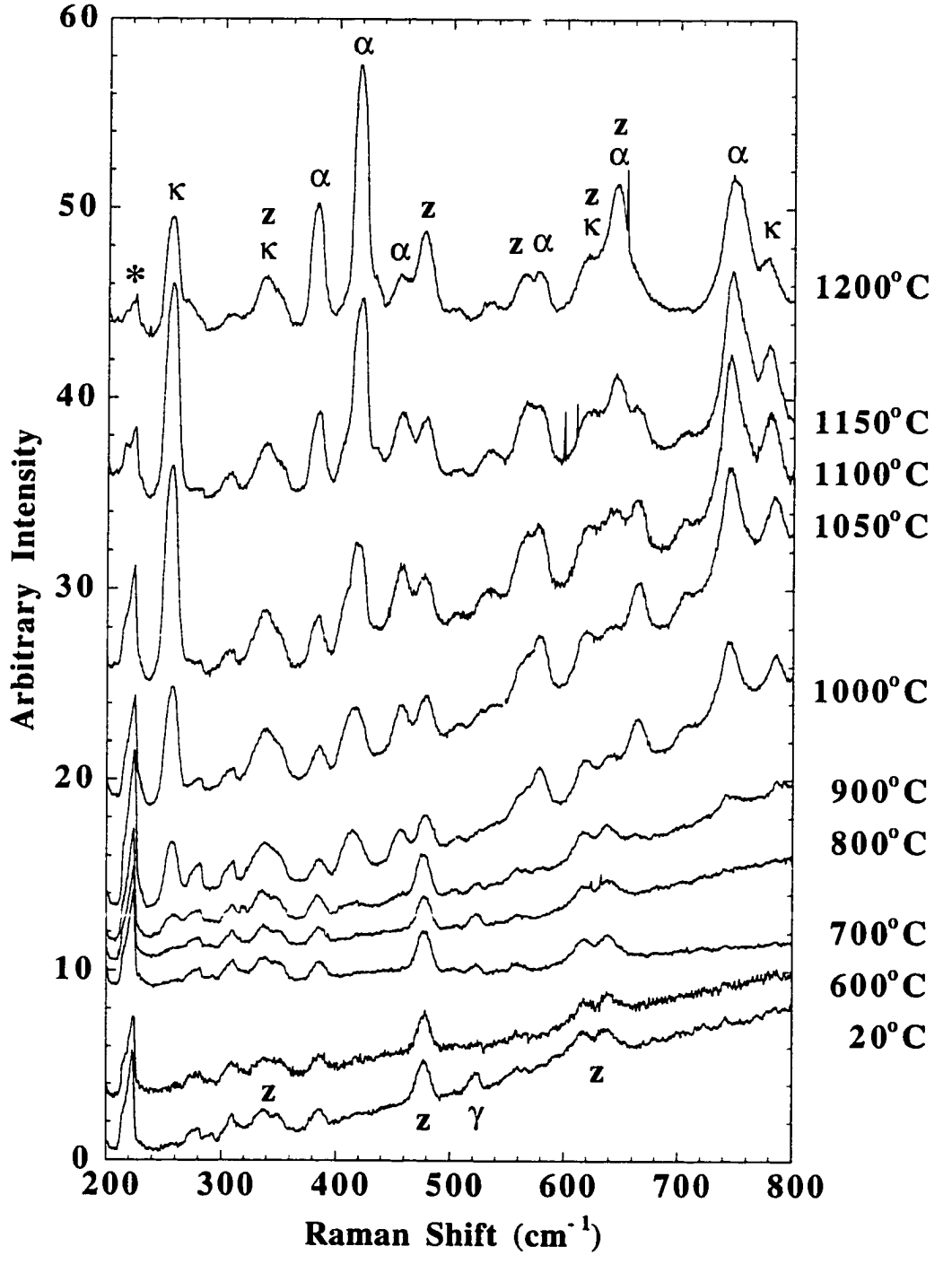

Figure 52. Raman Spectra From Al_2O_3 Doped With 2% ZrO_2. Powder heat treated at indicated temperatures for 1 hr.

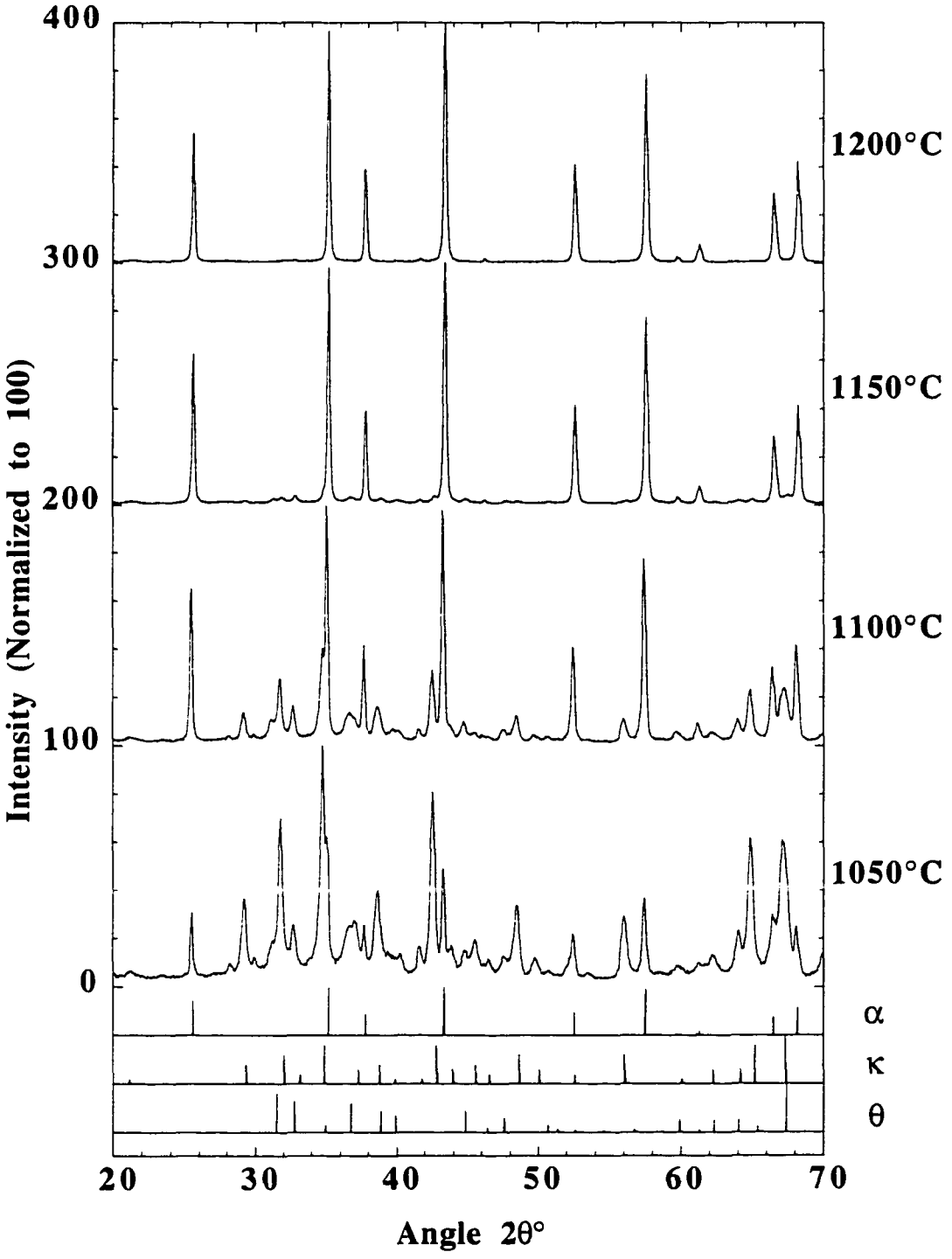

Figure 53. X-Ray Spectra From Undoped Al_2O_3. Powders heat treated at indicated temperatures for 1 hr.

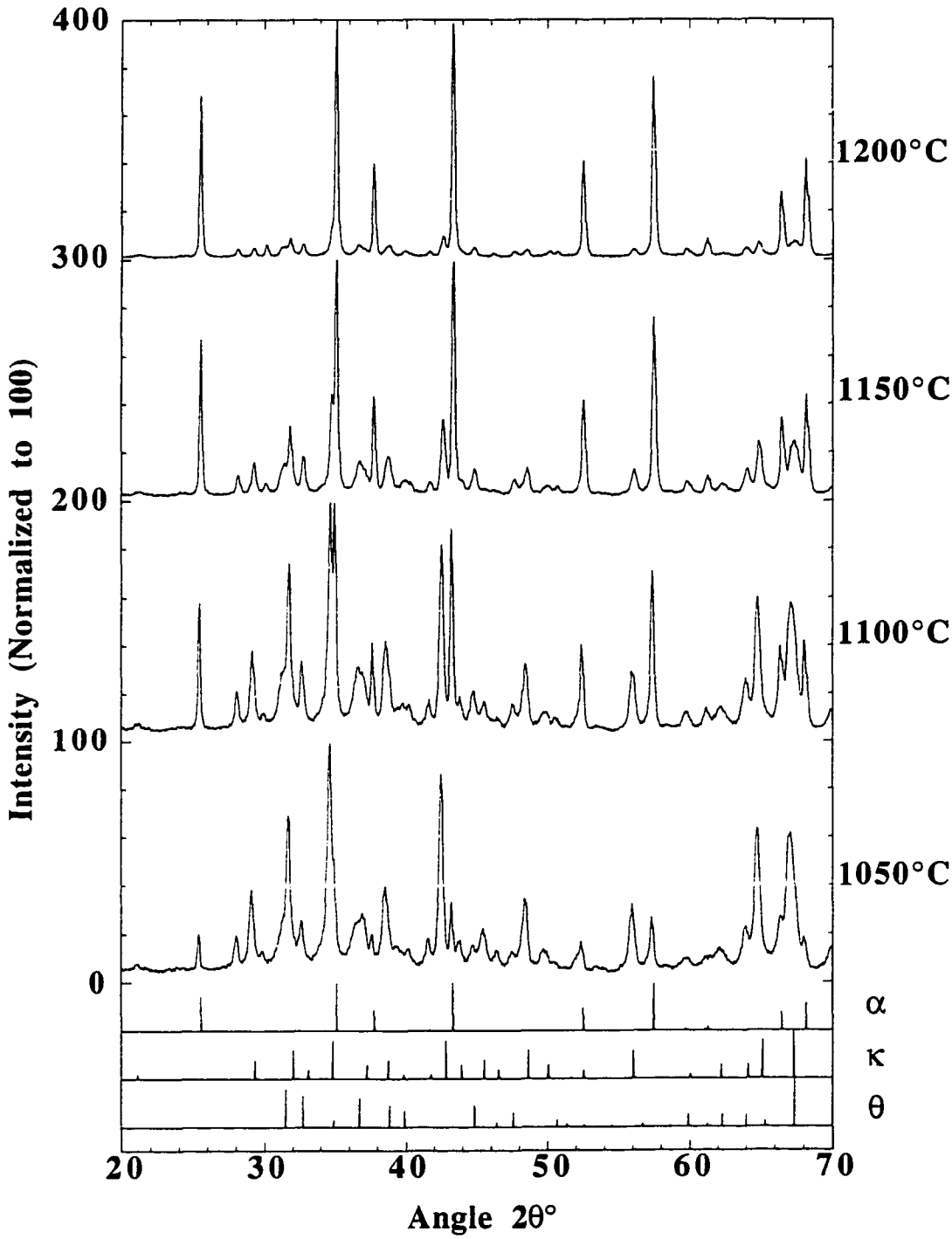

Figure 54. X-Ray Spectra From Al_2O_3 Doped With 2% ZrO_2. Powders heat treated at indicated temperatures for 1 hr.

the powder diffraction patterns acquired from the undoped and doped pellets respectively.

On the bottom of figures 53 and 54 there are graphical representations of the reported values of the 2θ positions and the relative intensities of the Bragg reflections for θ-, κ- and α- alumina. By comparing the reported 2θ positions and relative intensities for each alumina phase to those in the XRD spectra it can be seen that only κ- and α-alumina are produced on heating. Larger volume fractions of κ are observed at the lower heat treatment temperatures.

The evidence for the partial stabilization of the transient κ-A_2O_3 is apparent by observing the Raman and XRD spectra that are acquired after the 1200°C heat treatment. For the undoped sample all of the Raman and XRD peak can be attributed to α-alumina (figures 51 and 53), however the doped sample still produces peak attributable to κ-alumina (figures 52 and 54).

Figure 55 is a plot of the ruby fluorescence intensities for both samples. As in the scales, we found a similar logarithmic temperature dependence, and a large discrepancy in the signal intensity acquired from the doped and undoped samples. The discrepancy is close to a factor of 12, which we attribute to the ZrO_2 containing sample having a smaller volume fraction of α-Al_2O_3.

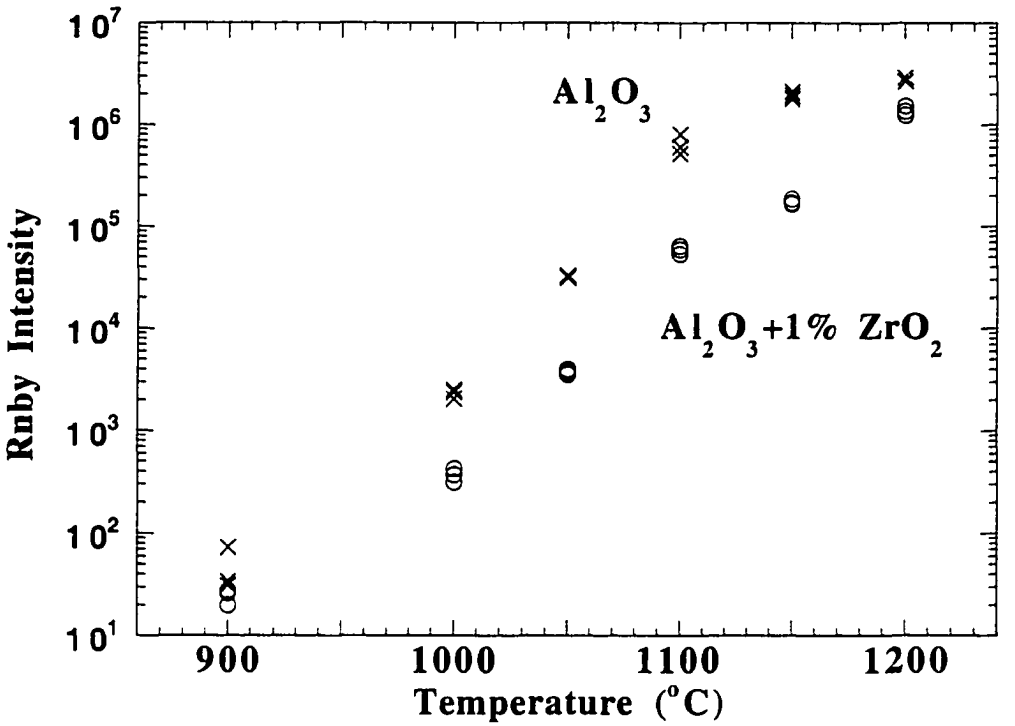

Figure 55. Ruby Fluorescence Intensities of Both Samples.

BIBLIOGRAPHY

J. S. Arlow, D. F. Mitchell, M. J. Graham, *Journal. of Vacuum Science and Technolgy,* **5**, No. 4, p 572 (1987)

N. W. Ashcroft, N. D. Mermin, *Solid State Physics,* (Horcourt Brace College Publishers, Fort Worth) (1976)

M. I. Baraton, G. Busca, M. C. Prieto, G. Ricchirdi, V. S. Escribano, *Journal of Solid State Chemistry*, **112**, p 9 (1994)

J. J. Barns, J. G. Goedjen, D. A. Shores, *Oxidation of Metals*, **32**,p 449 (1989)

B. D. Bartolo, *Optical Interactions in Solids,* (John Wiley, New York) (1968)

M. J. Bennett, *Surface and Interface Analysis*, **22**, p 421, (1994)

M. J. Bennett, P. R. Graves, R. W. M. Hawes, in *High Temperature Alloys, Their Exploitable Potential,* J. B. Marriott, M. Merz, J. Nihoul, J. Ward, (Elsevier Applied Science, London and New York, 1987) p 205 (1987)

F. F. Bentley, L. D. Smithson, A. L. Rozek, *Infrared Spectra and Characteristic Frequencies ~700-300 cm-1*, (Interscience Publishers, New York) (1968)

J. B. Bindell, in *Encyclopedia of Materials Characterization,* ed. C. R. Brundle, C. A. Evans, S. Wilson, L. E. Fitzpatrick (Butterworth - Heinemann, Boston) p 71 (1992)

J. Birnie, C. Craggs, D. J. Gardiner and P. R. Graves, *Corrosion Science*,**33**, p 1, (1992).

N. Boucherit, A. Hugot-Le Goff, S. Joiret, *Thin Solid Films*, **174,** p 111, (1989)

G. C. Bye, G. T. Simpkin, *Journal American Ceramin Society*, **57**, p 367 (1974).

R. J. Christennsen, D. M. Lipkin, D. R. Clarke, *Acta Materialia*, **44**, p 3813 (1996)

N. B. Colthup, S. E. Wiberley, L. H. Daly. *Introduction to Infrared and Raman Spectroscopy,* 2 ed. (Academic Press, New York) (1975)

CRC Handbook of Chemistry and Physics, edit by R. C. Weast, M. J. Astle, (CRC Press, Inc., Boca Raton Florida), 61st Edition, (1980)

R. E. Dientz, G. I. Parisot, A. E. Meixner, *Physical Review B*, **4**, p 2302 (1971).

Mary L. Duchi, *Economic Effects Of Metallic Corrosion in the United States*, Battelle Report to Specialty Steel Industry of North America (April 1995)

W. A. England, M. J. Bennett, D. A. Greenhalgh, S. N. Jenny, C. F. Knights, *Corrosion Science*, **26**, No 7, p 537 (1986)

H. E. Evans, A. M. Huntz, *Materials at High Temperatures*, **12**, p 111 (1994)

R. L. Farrow, R. E. Benner, A. S. Nagelberg, P. L. Mattern, *Thin Solid Films*, **73**, p 33 (1980)

R. L. Farrow, P. L. Mattern, A. S. Nagelberg, *Applied Physics Letters*, **36**, p 212, (1980)

R. L. Farrow, A. S. Nagelberg, *Applied Physics Letters* **36**, p 945, (1980)

J. R. Ferraro, K. Nakamoto, *Introduction to Raman Spectroscopy*, (Academic Press, Boston) (1994)

D. J. Gardiner in *Microscopy of Oxidation-2* eds. S. B. Newcomb and M. G. Bennet. (The Institute of Materials, London) (1993)

D. J. Gardiner, C. J. Littleton, K. M. Thomas, K. N. Strafford, *Oxidation of Metals*, **27**,p 57, (1987)

A. Goldsmith, T. E. Watermand, H. J. Hirschborn, *Handbook of Thermalophyisical Properties of Solids Materials*, (Pargamon Press, New York), Vol **2** , Alloys (1962)

Xiao-Yan Gong, D. R. Clarke, *Oxidation of Metals*, **50**, p 355 (1998)

M. J. Graham, R. J. Hussey, *Oxidation of Metals*, **44**, p 339 (1995)

P. R. Graves, C. Johnston, J, J, Campaniello, *Materials Research Bulletin*, **23**, p 1651 (1988)

M. Grimsditch, D. Renusch, B. W. Veal, J. K. Wright, R. L. Williamson, 193th ECS spring meeting, San Diego, CA., (1998) Vol 98-9 *High Temperature Corrosion and Materials Chemistry*, ed by P. Y. Hou, M. J. McNallan, R. Oltra, E. J. Opila, and D. A. Shores, (Electrochem. Soc., Pennington) p 32 (1998)

J. He, D. R. Clarke, *Journal American Ceramin Society*,**78**, p 1347 (1995)

H. Hindam, D. P. Whittle, *Oxidation of Metals*, **18**, p 245 (1982)

P. Y. Hou, R. M. Cannon, H. Zhang, R. L. Williamson, 190th ECS fall meeting, San Antonio, TX, Vol 96-26 *Fundamentals of High Temperature Corrosion*, ed by D. A. Shores, R. Rapp and P. Y. Hou, Electrochem. Soc., Pennington, NJ, p 28 (1997)

P.Y. Hou and J. Stringer, *Journal de Physique IV*, Colloque C9, supplement to *Journal de Physique III*, **3**, p. 231 (1993)

G. F. Imbusch in *Luminescence of Inorganic Solids*, ed.by B. D. Bartolo (Plenum Press, New York), p 115 - 130 (1977)

Instruments SA, Inc. *T64000 The Ultimate Raman Spectrograph.* (Instruments SA, Inc, New Jersey) (1995)

A. Jayaraman, *Review of Modern Physics*, **55**, p 65 (1983)

J. Jedlinski, *Solid State Phenomena*, **21&22**, p 335 (1992)

D. A. Jones, *Principles and Preventions of Corrosion*, (Prentice Hall, New Jersey) (1992)

A. A. Kaplyanskii, A. K. Przhevuskii and R. B. Rozenbaum, *Soviet Physics, Solid State* **10**, p 1864 (1969).

Leo Kay in the Press Office, Press Release, *United States Environmental Protection Agency*, Release# 98-3-20, (March 23, 1998)

J. R. Knibloe, R. N. Wright, V. K. Sikka, R. H. Baldwin, C. R. Howell, Materials Science and Engineering **A153** p. 282 (1992)

P. Kofstad, *High Temperature Corrosion*, (Elsevier Applied Science, New York, 1998)

P. Kofsted, *High-Temperature Oxidation of metals*, (John Wiley & Sons, New York) (1966)

I. Koshelev, A. P. Paulikas, B. W. Veal, *Oxidation of Metals*, **51**,p 23, (1999)

O. Kubaschewski, *Iron-Binary Phase Diagrams*, (Springer-Verlag, New York) (1992)

W. J. Lackey, D. P. Stinton, G. A. Carney, L. L. Fehrenbacher, A. C. Schaffhauser, Oake Ridge National Laboratory Report, ORNL/TM-8949

Landolt and Bornstein, *Numerical Data and Functional Relationships in Science and Technology*, (Springer, New York), New Series, Group III, Vol. **11**, p. 50 (1979)

D. M. Lipkin and D. R. Clarke, *Oxidation of Metals* , **45**, p 267 (1996)

D. M. Lipkin, D. R. Clarke, M. Hollatz, M. Bobeth, W. Pompe, *Corrosion Science*, **39**, p 231, (1997)

D. M. Lipkin, H. Schaffer, F. Adar, D. R. Clarke, *Applied Physics Letters*, **70**, No. 19, 2550 (1997)

C. Loung, J. W. Richardson, M. Ozawa, *Journal Alloys and Componds*, **250**, p 356 (1997) Proc. 21th Rare Earth Conference, Duluth, MN

K. L. Luthra, C. L. Briant, *Oxidation of Metals* , **26**, 397 (1986)

Qing Ma and D. R. Clarke, *Acta Metall. Materialia*, **41**, No. 6, 1811 (1993)

Qing Ma and D. R. Clarke, *Journal American Ceramin Society*, **77**,p 298 (1994)

Qing Ma and D. R. Clarke, *The American Society of Mechanical Eneineers*, AMD-Vol **181**, Book No. H00888 - 1993

Q. Ma, D. R. Clarke, *Journal American Ceramin Society*, **76**, p 1433 (1993)

Qing Ma, W. Pompe, J. D. French, D. R. Clarke, *Acta Metall. Materialia*, **42**, No. 5, 1673 (1994)

J. B. Marion, M. A. Heald, *Classical Electromagnetic Radiation*, 2ed. (Harcourt Brace Jovanovich, Publishers, San Diego) (1980)

M. J. Massey, N. H. Chen, J. W. Allen, R. Merlin, *Physical Review B*, **41**, p 8776 (1990).

K. F. McCarty, D. R. Boehme, *Journal of Solid State Chemistry* , **79**, p 19 (1989)

G. W. Meetham, *The Development of the Gas Turbine Materials*, (Halsted Press Division John Wiley & Sons, New York) (1981)

C. Mennicke, E. Schumann, C. Ulrich and M. Ruhle, (presented at the 4th Int. Symp. on *High Temp. Corrosion and Protection of Mat.*, Les Embiez, France, May 20-24, 1996) *Materials Science Forum* , **251-254**, p 251 (1997)

S. E. Molis and D. R. Clarke, *Journal American Ceramin Society*, **73**,p 3189 (1990)

P. Morgand, P. Mouturat, G. Sainfort, *Acta Metallurgica*, **16**, 867, (1968)

K. Natesan, K. L. Klug, D. Renusch, M. Grimsditch and B. W. Veal, Tenth Annual Conference on Fossil Energy Materials, Knoxville TN, May 14-16, (1996)

K. Natesan, C. Richier, B. W. Veal, M. Grimsditch, D. Renusch and A. P. Paulikas, *Argonne National Laboratory Report*, ANL/FE-95/02 (1995)

K. Natesan, B. W. Veal, M. Grimsditch, D. Renusch and A. P. Paulikas, Proc. *Ninth Annual Conference on Fossil Energy Materials*, Oak Ridge, TN, CONF-9505204, ORNL/FMP-95/1, p 225 (1995)

M. Ozawa, M. Kimura, A. Isogai, *Journal Materials Science Letters*, **9**, p 709 (1990)

W. D. Porter, P. J. Maziasz, *Scripta Metallurgica* , **29**, p 1043 (1993)

R. Prescott and M. J. Graham, *Oxidation of Metals*, **38**, p 233, (1992)

D. Renusch, M. Grimsditch, I. Koshelev, B. W. Veal, *Oxidation of Metals*, **46**, p 365 (1996)

D. Renusch, M. Grimsditch, I. Koshelev, B. W. Veal, *Oxidation of Metals*, **48**, p.471 (1997)

D. Renusch, M. Grimsditch, A. P. Paulikas, B. W. Veal, 193th ECS spring meeting, San Diego, CA., (1998) Vol 98-9 *High Temperature Corrosion and Materials Chemistry*, ed by P. Y. Hou, M. J. McNallan, R. Oltra, E. J. Opila, and D. A. Shores, Electrochem. Soc., Pennington, NJ, p 76 (1998)

D. Renusch, B. W. Veal, I. Koshelev, K. Natesan, M. Grimsditch and P. Y. Hou, *Fundamental Aspects of High Temperature Corrosion*, ed by D. A. Shores, R. Rapp and P. Y. Hou, (Electrochem. Soc., Pennington) Vol **96-26** p 62 (1997)

D. Renusch, B. W. Veal, K. Natesan, I. Koshelev, M. Grimsditch, 190th ECS fall meeting, San Antonio, TX., (1996) Vol **96-26** *Fundamentals of High Temperature Corrosion*, ed by D. A. Shores, R. Rapp and P. Y. Hou, Electrochem. Soc., Pennington, NJ, p 62 (1997)

D. Renusch, Murali, S. Uran, M. Grimsditch, B. W. Veal, J. K. Wright, R. L. Williamson -- (accepted by *Oxidation of Metals*-1999)

Louis Sass, Press Release, *United States Environmental Protection Agency*, Release# 98-OPA197, (July 6, 1998)

K. E. Sickafusin, *Encyclopedia of Materials Characterization*, ed. C. R. Brundle, C. A. Evans, S. Wilson, L. E. Fitzpatrick (Butterworth - Heinemann, Boston) (1992)

J. P. Singh, B. Nair, D. Renusch, M. Sutaria, and M. Grimsditch, 23rd Annual Cocoa Beach Conference on *Engineering Ceramics and Structures*, American Ceramic Society, Cocoa Beach, FL, Jan. 25, (1999)

C. J. P. Steiner, D. P. H. Hasselman, R. M. Spriggs, *Journal American Ceramin Society*, **54**, p 412 (1971).

R. J. Thibeau, C. W. Brown and R. H. Heidersbach, *Applied Spectroscopy*, **32**, p 32 (1978)

V. K. Tolpygo, D. R. Clarke, *Acta Metall. Materialia*, **46**, p 14 (1998)

V. K. Tolpygo, J. R. Dryden, D. R. Clarke, *Acta Materialia*, **46**, p 927 (1998)

Y. S. Touloukian, P. K. Kirby, R. E. Taylor, T. Y. Lee, *Thermophysical Properities of Matter: Thermal Expansion in Nonmetallic Solids*, (Plenum, New York), Vol. **13** (1977)

K. R. Trethwey, J. Chamberlain, *Corrosion for Students of Science and Engineering*, (Langman Scientific & Technical with John Wiley & Sons, New York) (1988)

B. W. Veal, D. Renusch, I. Koshelev, A. P. Paulikas, S. Uran, M. Grimsditch, P. Y Hou, 193th ECS spring meeting, San Diego, CA., (1998) *High Temperature Corrosion and Materials Chemistry*, ed by P. Y. Hou, M. J. McNallan, R. Oltra,

E. J. Opila, and D. A. Shores, (Electrochem. Soc., Pennington) Vol **98-9** p 65 (1998)

Q. Wen, D. R. Clarke, N. Yu and M,. Nastasi, *Applied Physics Letters,* **66,** p 293 (1995)

R. L. Williamson, J. K. Wright and R. M. Cannon, 190th ECS fall meeting, Oct. 6-11, 1996, San Antonio, TX. *Fundamentals of High Temperature Corrosion VI*, ed by D. A. Shores and P. Y. Hou, (Electrochem. Soc., Pennington) Vol **96-26** p 62 (1997)

J. K. Wright, R. L. Williamson and R. M. Cannon, Materials Science and Enginerring **A238** 411 (1997)

J. K. Wright, R. L. Williamson, P. Y. Hou, R. M. Cannon, D. Renusch, M. Grimsditch, B. W. Veal 193th ECS spring meeting, San Diego, CA., (1998) Vol 98-9 *High Temperature Corrosion and Materials Chemistry*, ed by P. Y. Hou, M. J. McNallan, R. Oltra, E. J. Opila, D. A. Shores, (Electrochem. Soc.,Pennington) p. 53 (1998)

J. K. Wright, R. L. Williamson, D. Renusch, M. Grimsditch, B. W. Veal, P. Y. Hou, R. M. Cannon, *Materials Science and Enginerring,* **A262**, p 246 (1998)

R. W. G. Wyckoff, *Crystal Structures*, (Interscience Publishers, New York) 2ed. Ed., Vol. **1**, p 85 (1963)

R. W. G. Wyckoff, *Crystal Structures*, (Interscience Publishers, New York) 2ed. Ed., Vol. **2**, p 6 (1964)

R. W. G. Wyckoff, *Crystal Structures*, (Interscience Publishers, New York) 2ed. Ed., Vol. **3**, p 79 (1965)

J. R. Wynnyckyj, C. G. Morris, *Metallurgical Transactions B*, Vol. **16B**, p 345 (1985)

T. Yada and H. Koguchi, *JSME Int. J.*, **34** (2) p 163 (1991)

J. C. Yang, M. Yeadon, B. Kolasa, J. M. Gibson, 193th ECS spring meeting, San Diego, CA., (1998) Vol 98-9 *High Temperature Corrosion and Materials Chemistry*, ed by P. Y. Hou, M. J. McNallan, R. Oltra, E. J. Opila, and D. A. Shores, Electrochem. Soc., Pennington, NJ (1998), p 126

E. Zouboulis, D. Renusch, M. Grimsditch, *Journal of Applied Physics Litters*, **72** (1) p 1 (1998)